UNIVERSITÀ
DEGLI STUDI
DI TRIESTE

DIPARTIMENTO DI FISICA

XXXVI CICLO DEL DOTTORATO DI RICERCA IN FISICA

ULTRAFAST NON-EQUILIBRIUM STUDIES OF COMPLEX MATERIALS THROUGH PUMP-PROBE AND STOCHASTIC SPECTROSCOPIES

Settore scientifico-disciplinare: **FIS/03**

DOTTORANDO
Enrico Maria Rigoni

COORDINATORE
Prof. Francesco Longo

SUPERVISORE DI TESI
Prof. Daniele Fausti

ANNO ACCADEMICO 2022/2023

"*-Do you see the light?-*
-What light?-"

Reverend Cleophus James & Elwood Blues, *The Blues Brothers*

Abstract

Ultrafast spectroscopies established as the primary investigation tool for complex materials, i.e. systems in which the coupling between electronic, vibrational and magnetic degrees of freedom generates a multitude of competing phases. Indeed, the characterization of dynamic processes triggered by ultrashort light pulses allows for the disentanglement of the different microscopic contributions and provides unique information about the leading interactions in matter.

In the first part of the thesis, we rely on the ultrafast technique of *pump-probe spectroscopy* to investigate the non-equilibrium response of two prototypical complex materials. At first, we present a dynamic study of the low-temperature ferrimagnet $RbNiF_3$ where we unveil novel information hidden to the static response, like the presence of dd-phonon coupling or the discovery of a photo-induced metastable state. Secondly, we characterize the electronic excitations of the $Bi_2Sr_2CaCu_2O_{8-\delta}$ cuprate superconductor. Notably, the non trivial polarization dependence of the superconducting birefringence signal suggests a scenario where time-reversal symmetry is broken.

The second part of the thesis approaches the problems of non-equilibrium physics from a different perspective which focuses on the development of new investigation tools. In particular, we present *Femtosecond Covariance Spectroscopy* (FCS), a novel spectroscopic technique which relies on multimode photonic correlations to unveil non-linear signals.

We discuss two different applications of FCS: i) we test the capabilities of the technique in measuring magnetic excitations. ii) we perform a time-resolved measurement of electronic Raman scattering from Cooper pairs in cuprates. The finding of magnonic signatures in $RbNiF_3$ and especially the discovery of a superconducting correlation signal above T_c in $Bi_2Sr_2CaCu_2O_{8-\delta}$ propose FCS as an ideal technique for the investigation of complex materials. In conclusion, we illustrate possible technological developments to overcome the major limitations of FCS (i.e. long acquisition times) and make it competitive with other spectroscopic techniques.

Contents

Chapter 1
Introduction

Light is essential for human life not only for the biological processes that it triggers, but also because it is a primary investigation tool that we use to perceive the world around us. Indeed, we continuously analyze through our eyes the light that is scattered by objects to 'study' the surrounding environment.
More than 100 years after the pioneering studies of Newton on the *composition of light* [1], W. H. Wollaston noted that the solar spectrum presented a series of *dark lines*, that were later discovered to coincide with the emission lines of heated chemical elements [2, 3]. This work paved the way for the investigation of material properties through light-matter interaction, being the first experiment of optical spectroscopy.

For a long time, the experimental approach of optical spectroscopies was to exploit electromagnetic fields to probe the material properties at *equilibrium*. However, new perspectives emerged with the advent of ultrafast laser sources. The possibility of employing ultrashort coherent light pulses not only to monitor the response of the system, but also to trigger dynamical processes, led to the development of *non-equilibrium* techniques grouped in the category of *ultrafast optical spectroscopy* [4].

Ultrafast spectroscopies

Ultrafast spectroscopy experiments measure the non-linear response of materials with a sequence of ultrashort pulses. The most used configuration, *pump-probe spectroscopy*, employs a pair of pulses first to promote the system into an excited state (*pump*) and then to follow the subsequent relaxation dynamics (*probe*).
Importantly, by resolving the temporal evolution of the system, complementary and, in several cases, additional information can be gained with respect to the equilibrium response.

That is the case of *complex materials*, a class of materials where the interplay of vibrational, electronic and magnetic degrees of freedom gives rise to multiple phase transitions and to exotic macroscopic states [5]. Indeed, ultrafast spectroscopies exploit the different thermalization timescales to disentangle the electrons, lattice and spin contributions and unveil the leading interactions of the various phases.

Remarkably, ultrafast light-matter interaction can also lead to the onset of metastable states via non-adiabatic phase transitions. When ultrashort light pulses inject a large number of excitations in the material within a time window that is shorter than the characteristic relaxation timescales, an anomalous energy redistribution between the microscopic degrees of freedom occurs, causing a change in the material properties.

Photo-induced changes in macroscopic properties like superconductivity [6–8], ferroelectricity [9] and optical transparency [10] constitute the first steps towards the optical control of matter states.

In this thesis, we adopt the aforementioned non-equilibrium approach to investigate the dynamic response of two prototypical complex materials: a magnetic compound which exhibits ferrimagnetic spin-order at low temperatures ($RbNiF_3$) and a high temperature cuprate superconductor ($Bi_2Sr_2CaCu_2O_{8+\delta}$).
We present a detailed study of the two materials with conventional pump-probe spectroscopy in the first part of the dissertation.

A different approach...

The multitude of open questions in ultrafast science, combined with the advancement of technological achievements, stimulates a continuous growth of novel experimental approaches towards the study of complex systems [11–13]. In particular, the hunt for new observables that potentially carry information hidden from conventional spectroscopies is always ongoing [14].
In the second part of the thesis, we explore the field of novel non-equilibrium techniques by developing a *stochastic* and *covariance-based* approach to study complex materials. Differently from the majority of spectroscopic techniques, *Femtosecond Covariance Spectroscopy* (FCS) exploits statistical momenta beyond the average (i.e. covariance) to reveal non-linear material responses. Specifically, FCS accounts on noisy pulses to evaluate multimode photonic correlations and measure low-energy modes.
Notably, FCS considers each repetition of the experiment as a measurement under different conditions. As a consequence, the technique is ideally suited for the investigation of materials in which fluctuations play a major role, like unconventional superconductors [15].

Detailed summary

The thesis is structured in the following way:

- In **Chapter 2** we discuss the basic principles of pump-probe spectroscopy. After a short theoretical introduction, we present the experimental setup with high temporal and frequency resolution that we developed for non-equilibrium experiments. By exploiting non-linear optical processes, we obtain laser beams with a wide range of tunability that goes from the visible to the mid-IR energy range. In this way, we can probe the frequency-resolved dynamic response related to the resonant excitation of specific electronic degrees of freedom (e.g. *dd-transitions*, *superconducting gap*, ...).

- **Chapter 3** is dedicated to a non-equilibrium study of the magnetic compound $RbNiF_3$. By applying pump-probe spectroscopy to the investigation of this low-temperature ferrimagnet, we report evidence of multiple coupling mechanisms between spins, phonons and electrons. First, we unveil the presence of optical transitions which are hidden in the linear response and involve both excitonic, vibrational and magnonic contributions. Secondly, we measure a long-living dynamic signal that we associate to a resonant transient magneto-optical Faraday effect possibly determined by the onset of a metastable phase. Finally, the spectral response of coherent excitations reveals non trivial coupling between low-energy phonons and *dd* excited states.

- In **Chapter 4** we face a different kind of complex material that is $Bi_2Sr_2CaCu_2O_{8+\delta}$, a ceramic compound that exhibits high temperature superconductivity. Among the wide range of unconventional features that characterize high temperature superconductors, we focus on the anisotropy of the superconducting gap and on its link with the B_{1g}/B_{2g} electronic excitations. In particular, starting from the equilibrium model for Raman scattering in Cuprates, we develop a non-equilibrium description of the process. Then, we test the selection rules of the two models by investigating the dynamic birefringence signal in the superconducting state. Two different scenarios emerge for the two excitations. The B_{2g} mode obeys the equilibrium model, since its selection rules do not depend on the pump polarization. The symmetry of the B_{1g} mode is not described by neither the static nor the dynamic model. We rationalize these results with a symmetry-breaking scenario that possibly reconnects to the predictions of time-reversal symmetry broken states in Cuprates.

- We present *Femtosecond Covariance Spectroscopy* (FCS) in **Chapter 5**. In a FCS experiment, the optical observable is not anymore the average of the spectral intensities, but is the multimode covariance computed across the probe spectrum. The key idea of this technique is that Raman interaction imprints photonic correlations onto a previously uncorrelated broadband pulse. For this reason, a crucial ingredient for FCS is the generation of stochastic (i.e. uncorrelated) pulses. We first describe the experimental implementation of Femtosecond Covariance Spectroscopy, focusing on the generation of stochastic pulses achieved through an SLM-based pulse shaper. Secondly, we validate the technique by presenting the results of FCS experiments on α-quartz.
  The second part of the Chapter is focused on the application of FCS to the study of complex materials. Starting from $RbNiF_3$, we investigate whether the technique is sensitive to magnetic excitations, finding good indications that this is the case. Finally, we setup a pump-probe FCS experiment on optimally-doped $Bi_2Sr_2CaCu_2O_{8+\delta}$ to measure the sub-ps response of electronic excitations. Notably, we unveil the presence of a correlation signal both in the superconducting and in the pseudogap phase of the sample, possibly suggesting the presence of local pairing above T_c

- In **Chapter 6**, we discuss possible technological developments to make Femtosecond Covariance Spectroscopy competitive with other spectroscopic techniques and propose a different method for the generation of stochastic pulses. Indeed, the main limitation of the technique resides in the acquisition time, limited by the SLM technology to $\sim 60\,\mathrm{Hz}$. For this reason, in collaboration with the Fastlite R&D department, we developed a *customized dazzler*, i.e. a pulse shaper based on an acousto-optic crystal. Differently from SLM-based systems, this kind of pulse shapers can potentially work up to $30\,\mathrm{kHz}$, hence improving by orders of magnitude the experimental acquisition times. We perform a set of preliminary tests to understand if stochastic pulses generated with this alternative method are truly uncorrelated and hence fit for FCS experiments. Our measurements unveil two major criticalities which are the presence of correlation fringes and the impossibility of selectively add stochastic fluctuations to limited regions of the pulse spectrum. Nonetheless, preliminary dynamic measurements show that intrinsic correlations wash out in the transient response. This evidence opens the possibility of employing dazzler-based FCS for time-resolved studies and potentially makes FCS competitive with other spectroscopic techniques.

References

[1] Isaac Newton. "A new theory about light and colors". In: *American journal of physics* 61.2 (1993), pp. 108–112.

[2] William Hyde Wollaston. "XII. A method of examining refractive and dispersive powers, by prismatic reflection". In: *Philosophical Transactions of the Royal Society of London* 92 (1802), pp. 365–380.

[3] Gustav Kirchhoff. "Ueber die Fraunhofer'schen Linien". In: *Annalen der Physik* 185.1 (1860), pp. 148–150.

[4] Margherita Maiuri, Marco Garavelli, and Giulio Cerullo. "Ultrafast spectroscopy: State of the art and open challenges". In: *Journal of the American Chemical Society* 142.1 (2019), pp. 3–15.

[5] Claudio Giannetti et al. "Ultrafast optical spectroscopy of strongly correlated materials and high-temperature superconductors: a non-equilibrium approach". In: *Advances in Physics* 65.2 (2016), pp. 58–238.

[6] Daniele Fausti et al. "Light-induced superconductivity in a stripe-ordered cuprate". In: *science* 331.6014 (2011), pp. 189–191.

[7] Wanzheng Hu et al. "Optically enhanced coherent transport in YBa 2 Cu 3 O 6.5 by ultrafast redistribution of interlayer coupling". In: *Nature materials* 13.7 (2014), pp. 705–711.

[8] Matteo Mitrano et al. "Possible light-induced superconductivity in K3C60 at high temperature". In: *Nature* 530.7591 (2016), pp. 461–464.

[9] TF Nova et al. "Metastable ferroelectricity in optically strained SrTiO3". In: *Science* 364.6445 (2019), pp. 1075–1079.

[10] Alexandre Marciniak et al. "Vibrational coherent control of localized d–d electronic excitation". In: *Nature Physics* 17.3 (2021), pp. 368–373.

[11] Alfred Zong et al. "Emerging ultrafast techniques for studying quantum materials". In: *Nature Reviews Materials* 8.4 (2023), pp. 224–240.

[12] Frank Y Gao et al. "Ultrafast single-shot optical and THz spectroscopy: a window into nonlinear dynamics of condensed matter systems". In: *Ultrafast Phenomena and Nanophotonics XXVII*. Vol. 12419. SPIE. 2023, pp. 14–20.

[13] Jack Zwettler et al. "An extreme ultraviolet 2e-ARPES setup based on dual time-of-flight analyzers". In: *Journal of Electron Spectroscopy and Related Phenomena* 270 (2024), p. 147417.

[14] Filippo Glerean et al. "Time-resolved multimode heterodyne detection for dissecting coherent states of matter". In: *Optics Letters* 45.13 (2020), pp. 3498–3501.

[15] VJ Emery and SA Kivelson. "Importance of phase fluctuations in superconductors with small superfluid density". In: *Nature* 374.6521 (1995), pp. 434–437.

Part I

Pump-Probe spectroscopy & Complex Materials

Chapter 2
Non-equilibrium spectroscopies

2.1 Pump-probe spectroscopy

Complex materials are characterized by the interplay between magnetic, vibrational and electronic degrees of freedom. To understand the intricate coupling mechanisms that rule the physical properties in these systems, the study of the linear response alone doesn't suffice [1]. In this framework, non-linear spectroscopy, and in particular *pump-probe spectroscopy*, established as a unique tool to disentangle competing interactions and to control transient states of matter [2–5].

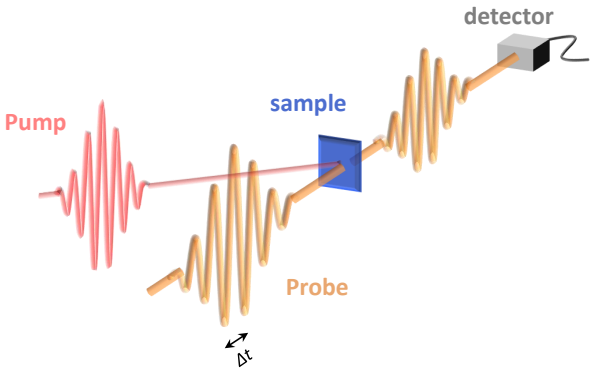

FIGURE 2.1: sketch of a *pump-probe* experiment. An intense ultrashort pulse, the *pump*, impinges on a system triggering excitations. After a well-defined time delay Δt, a second pulse, the *probe*, interacts with the excited system and is subsequently measured.

In a pump-probe experiment, two ultrashort light pulses are used to study out-of-equilibrium systems. First, one intense pulse, the *pump*, impinges on the material and brings it into an excited state. Then, after a controlled time delay, a second pulse (i.e. the *probe*) interacts with the excited system and is subsequently measured (Figure 2.1). By reconstructing the temporal profile of the reflected/transmitted probe light as a function of the delay between the two pulses, it is possible to follow the relaxation dynamics of the material.

In Figure 2.2 we report a typical single-color pump-probe trace. In particular, we follow

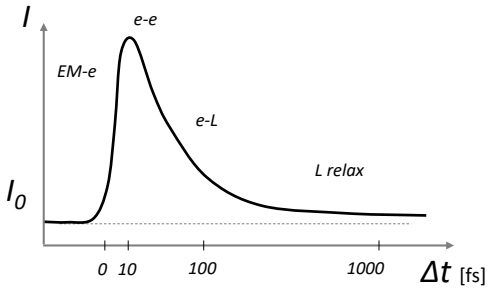

FIGURE 2.2: typical example of a pump-probe trace. Adapted from [6].

the relaxation dynamics by probing the changes in the probe intensity[1] as a function of the delay time. Notably, the temporal dynamics are representative of the different interaction timescale, e.g. the electromagnetic field with the electrons (EM-e), the electron-electron interactions (e-e), the electron-lattice (e-L), and the lattice thermalization (L) [10].

2.1.1 Theoretical description

When an electric field $E(t)$ interacts with the electrons of a material, we can model the light-matter interaction with a field- induced displacement of the electrons from the equilibrium position $r(t)$. This displacement will result in an electric dipole moment $\mu(t) = -e \cdot r(t)$, where e represents the electron charge. By adding up all the N electric dipoles in the unit volume, we obtain the macroscopic polarization of the material :

$$P(t) = N \cdot \mu(t) \tag{2.1}$$

that we can express in terms of the electric field as

$$P(t) = \epsilon_o \int \chi(t - t')E(t')dt' \tag{2.2}$$

where ϵ_0 is the dielectric permittivity of vacuum and χ, the susceptibility of the material, encloses the sample contribution to the optical response. Notably, the expression can be conveniently rewritten in the frequency domain as:

$$P(\omega) = \epsilon_o \chi(\omega)E(\omega) \tag{2.3}$$

If the incident electric field is weak with respect to the electron-nuclei binding force, the force exerted on the electrons can be approximated by a harmonic perturbation and the dependence of the polarization from the electric field is linear (equation 2.3). However, when the fields become stronger, anharmonic effects emerge and corrections with higher orders of the electric field must be included [11]. In other words, we expand P in powers of E:

$$P \equiv P_L + P_{NL} = \epsilon_0 \Big[\chi^{(1)}E + \chi^{(2)}E^2 + \chi^{(3)}E^3 + ...\Big] \tag{2.4}$$

that we rewrite as

$$P(k, \omega) = \epsilon_0 \sum_j \chi^{(j)}E^j(k, \omega) \tag{2.5}$$

[1] We underline that even if it is the most studied, intensity isn't the only meaningful observable in a pump probe experiment [7–9].

From a theoretical point of view, a pump-probe experiment can be pictured as a *third order process*, where three incoming fields $E_i(k,\omega)$ (two coming from the pump pulse and one taken from the probe) interact via the third order susceptibility tensor of the material $\chi^{(3)}$ to generate a fourth signal field:

$$E_s(k_s,\omega_s) \propto \chi^{(3)} \prod_{i=1}^{3} E_i(k_i,\omega_i) \tag{2.6}$$

Notably, the generated signal field propagates along the same direction of the incoming probe beam

$$k_s = k_{probe} \tag{2.7}$$

In the four-wave mixing framework, this evidence reconciles with the momentum-conservation law

$$k_s = \sum_i k_i \tag{2.8}$$

by imposing that the two pump photons hold opposite momentum ($k_1 = -k_2$). On the contrary, there is no way of respecting both equation 2.7 and 2.8 in a *second order* formalism.

Finally, we point out that the signal field E_s is typically orders of magnitude weaker than the incoming beams. Nonetheless, it is still detectable because it is conveniently amplified by the co-propagating scattered probe through the so-called *heterodyne process*[2] [13].

2.2 Experimental implementation

In the following Section, we introduce the main elements that constitute the experimental setup that we use for performing pump-probe experiments. A detailed description of the specific arrangements used for the different experiments is postponed to the correspondent Chapters.

There are two key ingredients that must be taken into account in the design of a pump-probe experiment: the temporal duration and the energy range of the ultrashort light pulses.
First, the temporal duration of pump/probe pulses is linked to the time resolution of the experiment. In particular, dynamic changes that occur on timescales shorter than the convolution of the pulses temporal profiles can't be resolved[3]. Therefore, the pulsed-laser source must be chosen in accordance to the timescales of the phenomena under study [4].

A second important parameter is the energy of the light pulses. Indeed, the possibility of tuning the energy of the pulses in/off resonance with specific degrees of freedom (e.g. magnetic excitation, electronic transition, ...) allows to study peculiar effects that occur in complex materials [3–5, 17, 18].

[2] In the *Heterodyne process* a weak field interacts in an interferometer with a stronger classical field, commonly named *Local Oscillator*, to generate a phase-referenced and amplified version of the signal field [12]. Since in a pump-probe experiment the Local Oscillator coincides with the driving field, the signal is said to be *self-heterodyned*.

[3] In some cases (*chirped pulses*) the temporal resolution of PP experiments can be pushed below the temporal duration of the pump/probe pulses [14].

[4] Notably, the efforts for developing laser sources which provide shorter light pulses represent a proper branch of physics [15, 16].

Our setup accounts for both of these aspect and provides ultrashort laser pulses with a wide range of energy tunability (Figure 2.3). We use a Ti-Sapphire laser source (Pharos, *Light Conversion*) to generate coherent light pulses ($400\,\mu J$, $50\,kHz$) at $1030\,nm$. Then, we split the radiation into three different portions that we use to generate three different beams:

- a broadband white light beam
- a beam in the visible/near-IR range
- a beam in the MIR range

Visible-NIR light beam

We use $40\,\mu J$ of the $1030\,nm$ radiation to pump Non-Collinear Optical Parametric Amplifier (Orpheus-N,*Light Conversion*) and generate ultrashort laser pulses ($< 25\,fs$) with tunable energy in the range 650-$900\,nm$ (1.37-$1.90\,eV$).
In pump-probe experiments, this beam can be used both as a probe (see Chapters 4 and 5) or as a pump (Chapter 3). Moreover, the visible/near IR energy range is suited for optical manipulation of the light pulses, i.e. *pulse shaping* (further details are provided in Chapter 5).

MIR light beam

The second pulse is obtained by pumping with $350\,\mu J$ of the fundamental beam a Twin Optical Parametric Amplifier system (Orpheus-TWIN, *Light Conversion*). The two output beams are mixed in a *GaSe* crystal where the non-linear phenomenon of *Difference Frequency Generation (DFG)* takes place. After filtering out the short wavelength components ($<4\,\mu m$), we obtain low energy pulses that we can tune in the range 4.5-$20\,\mu m$ (0.06-$0.27\,eV$). The temporal duration of MIR pulses is $>100\,fs$. We use MIR pulses just as pump pulses.

White light beam

The remaining $10\,\mu J$ of the $1030\,nm$ radiation are filtered and focused on a $6\,mm$ thick sapphire crystal (Al_2O_3) to generate broadband white-light pulses (bandwidth $= 1.4$-$2.2\,eV$) by *self phase modulation*. Importantly, the supercontinuum pulses are *chirped*, i.e. low frequency components travel in the leading edge of the pulse while high frequency ones travel in the tail, determining an elongated temporal profile ($<1\,ps$). This results in a distortion of the pump-probe signal that we can correct in post processing (Figure 2.4). We exploit the broad spectral content of white-light pulses to probe the spectral response of materials.

The setup is provided with two translation stages that control the relative time delay between the three beams.
All beams have linear polarization. In particular, we can tune the orientation of the white light and of the visible/NIR beam with a combination of half-wave plates and polarizers. The polarization of the MIR beam is vertical and is fixed.
All beams are focused on the sample and, according to the experiment, focal lenses are chosen in order to obtain the desired spot size.

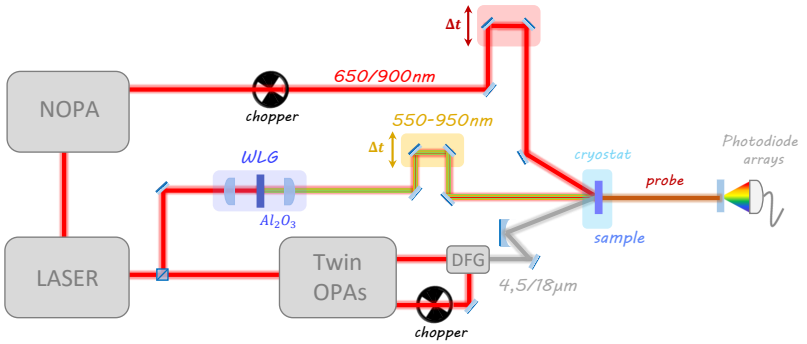

FIGURE 2.3: sketch of the general setup. According to the experiment, the role of *pump* and *probe* can be played by different beams.

We point out that the setup is suited for performing 3 pulses experiments, where pump pulses with different energies are exploited to target different excitations [19]. Some examples can be found in [20].

2.2.1 Sample

The sample is mounted in a closed cycle liquid helium cryostat (DE 204 by *Advanced Research Systems*) that can reach temperatures down to $8\,\mathrm{K}$. Samples are glued with conductive silver paint on a copper sample holder that is in thermal contact with the cold finger of the cryostat[5] .
The cryostat is arranged on a customized mechanical structure that ensures movements along the x, y and z axis. In addition, if the experiment requires a specific orientation of the sample, a piezoelectric rotator (*Attocube*, ANR240) can be inserted in between the sample and the sample holder[6].
We monitor the temperature of the sample with a thermocouple mounted close to the sample position. When the sample is directly glued on the sample holder, the minimum temperature reachable is $\sim 10\,\mathrm{K}$, while it increases to $\sim 40\,\mathrm{K}$ when the rotator is inserted.

According to the specific sample under study, the experiments can be performed in *reflection* or in *transmission* geometry.

2.2.2 Detection

As sketched in Figure 2.3, we collect the probe beam after its interaction with the sample[7] and we disperse the different spectral components with a transmission grating. Then, the spectral dispersed probe is focused on an NMOS detector, constituted by an array of 128 silicon photodiodes (*Hamamatsu*, S8380-128Q).
NMOS detector are synchronized with the laser source and can provide single-shot acquisition up to $5\,\mathrm{kHz}$. If the experiment is performed at higher repetition rates, single-shot acquisition is not available anymore and the detected signal is integrated over subsequent pulses.

[5] To improve the thermal contact we insert Indium foils inside the copper-copper junctions.

[6] We underline that in principle the sample can stay fixed and the polarization of the light beams can be rotated. However, there are cases where we can't manipulate the beam polarization (MIR pulses) and so the rotator is needed.

[7] either the reflection or the transmission beam

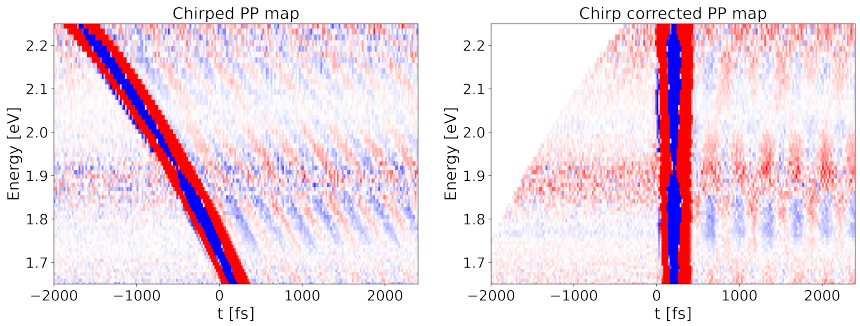

FIGURE 2.4: PP maps with temporal chirp (left) and with a correction of the chirp (right) performed in post-processing.

We frequency calibrate the detector by using a commercial bandpass filter (FGB67, *Thorlabs*) with a previously characterized transmission spectrum.

2.2.3 Differential Acquisition

In pump-probe experiments, we're interested in measuring the differential signal associated to the pump-induced excitation. For this reason, we insert a mechanical blade (*chopper*) along the pump optical path that periodically blocks the pump/let it pass. We sort the two datasets, *pumped* and *unpumped*, by referencing the presence/absence of the pump with a photodiode.
In *transmission geometry*[8], the differential signal, that is a function of the pump-probe delay t and of the probe frequency ω, is defined as:

$$\frac{\Delta T(\omega,t)}{T} = \frac{T_{pumped}(\omega,t) - T_{unpumped}(\omega,t)}{T_{unpumped}(\omega,t)} \tag{2.9}$$

where T_{pumped} is the probe transmitted light when the pump excites the sample and $T_{unpumped}$ is the spectrum measured when the pump is blocked.

We point out that broadband pulses commonly present *temporal chirp*, i.e. different spectral components are located at different times of the pulse temporal profile. This can be due to the interaction of the light pulse with dispersive elements or can be intrinsic in the generation process of the pulse, as in the case of supercontinuum light (*self-phase modulation*).
In pump-probe experiments, the presence of temporal chirp appears as a frequency-dependent time delay between the two pulses.

In Figure 2.4 (left), we observe the effect of temporal chirp in a pump probe map, where the differential transmissivity is plotted as a function of the pump-probe delay (x-axis) and of the probe frequency energy (y-axis). Importantly, temporal chirp can be corrected or by inserting optical elements with negative temporal dispersion or directly in post-processing (Figure 2.4 right).

Notably, in both the *chirped* and in the *corrected* PP maps, we observe quick oscillations at positive times with a period of $\sim 330\,\mathrm{fs}$, that is a much smaller time with respect to the temporal chirp of the pulses ($\sim 2\,\mathrm{ps}$). This is possible because the actual experimental resolution depends on the pulse-sample interaction and in particular on the

[8] *Reflection geometry* can be treated analogously.

duration of the interaction between the perturbed sample and the specific probe spectral component that is later resolved on the detector pixel [14].

References

[1] Yao Wang et al. "Theoretical understanding of photon spectroscopies in correlated materials in and out of equilibrium". In: *Nature Reviews Materials* 3.9 (2018), pp. 312–323.

[2] Claudio Giannetti et al. "Ultrafast optical spectroscopy of strongly correlated materials and high-temperature superconductors: a non-equilibrium approach". In: *Advances in Physics* 65.2 (2016), pp. 58–238.

[3] Daniele Fausti et al. "Light-induced superconductivity in a stripe-ordered cuprate". In: *science* 331.6014 (2011), pp. 189–191.

[4] TF Nova et al. "Metastable ferroelectricity in optically strained SrTiO3". In: *Science* 364.6445 (2019), pp. 1075–1079.

[5] Alexandre Marciniak et al. "Vibrational coherent control of localized d–d electronic excitation". In: *Nature Physics* 17.3 (2021), pp. 368–373.

[6] Fabio Novelli. "In search of selective excitations for studying out-of-equilibrium properties in strongly correlated electron systems and high temperature superconductors". PhD thesis. University of Trieste, 2012.

[7] Filippo Glerean et al. "Time-resolved multimode heterodyne detection for dissecting coherent states of matter". In: *Optics Letters* 45.13 (2020), pp. 3498–3501.

[8] Giorgia Sparapassi et al. "Transient measurement of phononic states with covariance-based stochastic spectroscopy". In: *Light: Science & Applications* 11.1 (2022), p. 44.

[9] Dario De Angelis et al. "Free electron laser stochastic spectroscopy revealing silicon bond softening dynamics". In: *Physical Review B* 107.21 (2023), p. 214305.

[10] Eric Beaurepaire et al. "Ultrafast spin dynamics in ferromagnetic nickel". In: *Physical review letters* 76.22 (1996), p. 4250.

[11] Eric Olaf Potma and Shaul Mukamel. "Theory of coherent Raman scattering". In: *Coherent Raman Scattering Microscopy* (2012), pp. 3–42.

[12] Filippo Glerean. "Multimode heterodyne detection for ultrafast investigation of quantum materials". PhD thesis. University of Trieste, 2020.

[13] Giorgia Sparapassi. "Femtosecond Covariance Spectroscopy". PhD thesis. University of Trieste, 2019.

[14] Dario Polli et al. "Effective temporal resolution in pump-probe spectroscopy with strongly chirped pulses". In: *Physical Review A* 82.5 (2010), p. 053809.

[15] G Steinmeyer et al. "Frontiers in ultrashort pulse generation: pushing the limits in linear and nonlinear optics". In: *Science* 286.5444 (1999), pp. 1507–1512.

[16] Gerard Mourou and Toshiki Tajima. "More intense, shorter pulses". In: *Science* 331.6013 (2011), pp. 41–42.

[17] F Giusti et al. "Signatures of enhanced superconducting phase coherence in optimally doped Bi 2 Sr 2 Y 0.08 Ca 0.92 Cu 2 O 8+ δ driven by midinfrared pulse excitations". In: *Physical review letters* 122.6 (2019), p. 067002.

[18] Davide Bossini et al. "Controlling coherent and incoherent spin dynamics by steering the photoinduced energy flow". In: *Physical Review B* 89.6 (2014), p. 060405.

[19] Angela Montanaro et al. "Visible pump–mid infrared pump–broadband probe: Development and characterization of a three-pulse setup for single-shot ultrafast spectroscopy at 50 kHz". In: *Review of Scientific Instruments* 91.7 (2020).

[20] Angela Montanaro. "Non-equilibrium response of quantum materials to resonant low-energy electronic photo-excitations". PhD thesis. University of Trieste, 2022.

Chapter 3

Transient Faraday effect and dd-phonon coupling in $RbNiF_3$

3.1 Abstract

Differently from the majority of ABF_3 fluorides, $RbNiF_3$ is a low-temperature ferrimagnet with hexagonal structure [1]. Below the Curie temperature $T_c = 139\,\mathrm{K}$, Ni spins align generating two inequivalent sub-lattices with opposite orientation that determine the ferrimagnetic character of $RbNiF_3$ [2].
In the late 60's, after the determination of the aforementioned magnetic behavior, studies on $RbNiF_3$ focused on the optical properties of the absorption spectrum [2–4]. In particular, curiosity was stimulated by the $3A_2 \rightarrow {}^1E^a$ *dd* transition, that unveiled magnonic and phononic sidebands [3, 4].

The presence of multiple *dd-transitions* in the visible range combined with the evidence of *exciton-phonon* and *exciton*-magnon coupling propose $RbNiF_3$ as an ideal platform to test the interplay between electronic, magnetic and vibrational degrees of freedom. Towards this direction, the application of ultrafast spectroscopy - the established primary investigation tool for complex systems [5] - to the study of $RbNiF_3$ is the direct next step. However, up to now, no pump-probe study on $RbNiF_3$ has been reported and the only dynamic studies present in literature are limited to the parent compound $KNiF_3$ [6–9].

In this Chapter, we extend the non-equilibrium approach to $RbNiF_3$ with the aim of adding new evidences to the intricate picture of spin-lattice-electronic coupling [6, 10–12]. After a short introduction on the sample properties, we present a set of equilibrium measurements where we reproduce the literature results. Then, we present the non-equilibrium experiment, drawing a direct link between the dynamic and the static response. Subsequently, we discuss the magneto-optical origin of the dynamic signal, supporting our discussion with polarization resolved measurements. In addition, we propose a theoretical model to explain the resonant nature of the transient response. Finally, in the last section of the Chapter, we isolate the coherent response of the system, unveiling evidences of *dd-phonon* coupling.

3.2 Introduction

$RbNiF_3$ is a magnetic compound that at atmospheric pressure crystallizes in a hexagonal structure[1] with space group D_{6h} and a $BaTiO_3$-like configuration [1]. Below the Curie temperature T_c=139 K, $RbNiF_3$ exhibits ferrimagnetic ordering while at higher temperatures the sample is a paramagnet [14].

In Figure 3.1 (a) we display the atomic structure of the $RbNiF_3$ unit cell. Each Ni ion is at the center of an octahedron formed by six F ions. Notably, not all the octahedra are equivalent. In particular, we can distinguish between A-sites and B-sites Ni atoms, depending if the relative octahedra share a corner or a face with the neighbours.

This distinction is particularly relevant for the magnetic properties of the system. Indeed, neighbouring Ni atoms interact via *superexchange* interaction mediated by the interstitial F atom and, according to the Ni-F-Ni angle, the interaction can either be ferromagnetic (if Ni-F-Ni angle is $90°$) or antiferromagnetic (if it is $180°$) [15, 16].
Since the angle between two adjacent B-sites Ni atoms is $\sim 90°$ while the Ni-F-Ni angle between A-B sites is $180°$ (see Figure 3.1, b), two different sub-lattices with opposite spin orientation are created: A-sites Ni orient with spin down (blue arrows in Figure 3.1) while B-sites Ni align with spin up (red arrows).

We underline that, since the number of B-sites Ni is twice the A-sites one, the two spin sub-lattices are inequivalent. Consequently, a ferrimagnetic ground state is established.
This evidence was confirmed by experimental measurements of the magnetic moment, where the net contribution to the saturation magnetization was found to be one third of the expected value for ferromagnetic ordering [2]. Importantly, Figure 3.1 displays a spin alignment parallel to the $\hat{c}$ axis of the sample but $RbNiF_3$ actually exhibits easy-plane anisotropy, with the lowest-energy spin orientation being in the basal plane ($\perp \hat{c}$) [2].

The ferrimagnetic-to-paramagnetic phase transition is well evidenced in the spectrum of low-energy excitations of $RbNiF_3$. Figure 3.2 displays the Raman spectrum of the material in the ferrimagnetic state (15 K), in the paramagnetic one (200 K) and at the phase transition (140 K) [14]. We address two different kinds of excitations. First, there are Raman peaks which do not change across the phase transition that are associated to phononic excitations.
Secondly, there is an intense peak in the ferrimagnetic state centered at $\sim$14 THz (470 cm^{-1}) that broadens and shifts to lower energies when the temperature is increased. At high temperatures, the peak almost vanishes.
This Raman peak is related to a *2-magnon* excitation, i.e. a pair of magnon excitations associated to the two different spin sub-lattices[2]. Hence, it's strictly linked to the magnetic ordering of the system.

3.2.1 Optical properties

Apart for the magnetic behavior, $RbNiF_3$ was much investigated for its peculiar optical properties. Like similar fluorides compounds, the optical absorption spectrum of $RbNiF_3$

[1] At high pressures, $RbNiF_3$ enters in a new phase characterized by a cubic perovskite structure similar to the one of $KNiF_3$ [13].

[2] Fleury et al. [17] tested the Raman response in the presence of an external magnetic field. No appreciable change of the 2-magnon peak was observed, confirming that the excitation carries a net spin = 0.

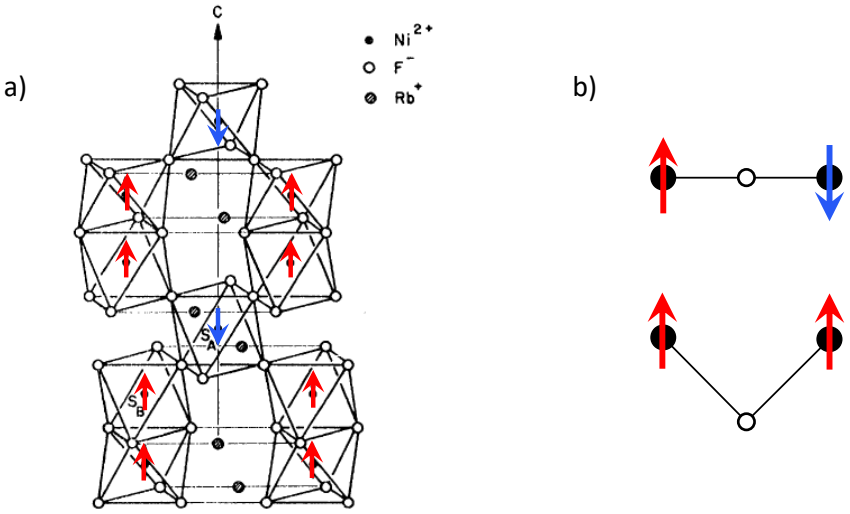

FIGURE 3.1: unit cell of $RbNiF_3$ (a). Ni ions interact via superexchange interaction: depending on the Ni-F-Ni angle, the spins have a parallel or antiparallel orientation (b), determining the macroscopic ferrimagnetic state below T_c=139 K. Adapted from [14].

is dominated by *dd-transitions* [18]. In particular, experimental efforts were focused on the characterization of the multi-peak $3A_2 \rightarrow {}^1E^a$ transition in an attempt to understand the origin of its unusual lineshape [3, 4].

Zanmarchi and Bongers studied the dependence of the $3A_2 \rightarrow {}^1E^a$ lineshape on the polarization of the incoming light [3]. The resulting absorption spectra collected in the ferrimagnetic phase of the sample are plotted in Figure 3.3 (a).
Remarkably, they revealed the presence of 3 or 4 sidebands, depending if the incident light was polarized orthogonal or parallel to the $\hat{c}$-axis, in the ferrimagnetic state of $RbNiF_3$. Moreover, they reported the disappearing of the sidebands in the paramagnetic state.

Later, Pisarev et al. performed a systematic investigation of the same transition on a set of fluorides compounds ($RbNiF_3$ included) with multiple techniques [4]. The Magnetic Linear Dichroism, Magnetic Circular Dichroism and Absorption spectra[3] of $RbNiF_3$ are showed in Figure 3.3 (b).
Moreover, the authors proposed a possible interpretation of the various peaks. In particular, they addressed the low-energy peak (centered at $\sim$15.000 cm^{-1} in Figure 3.3 (b), low) to an *exciton* transition, the middle one ($\sim$15.400 cm^{-1}) to an *exciton+phonon* transition and the high energy peak ($\sim$15.800 cm^{-1}) to an *exciton+phonon+magnon* transition.

[3] The absorption spectrum is obtained with $E_{incident} \perp \hat{c}$.

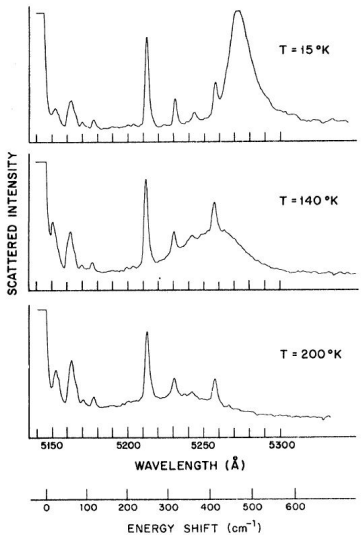

FIGURE 3.2: Raman spectrum of $RbNiF_3$ acquired in the ferrimagnetic ($10\,\mathrm{K}$), paramagnetic state ($200\,\mathrm{K}$) and at the phase transition ($140\,\mathrm{K}$). From [14].

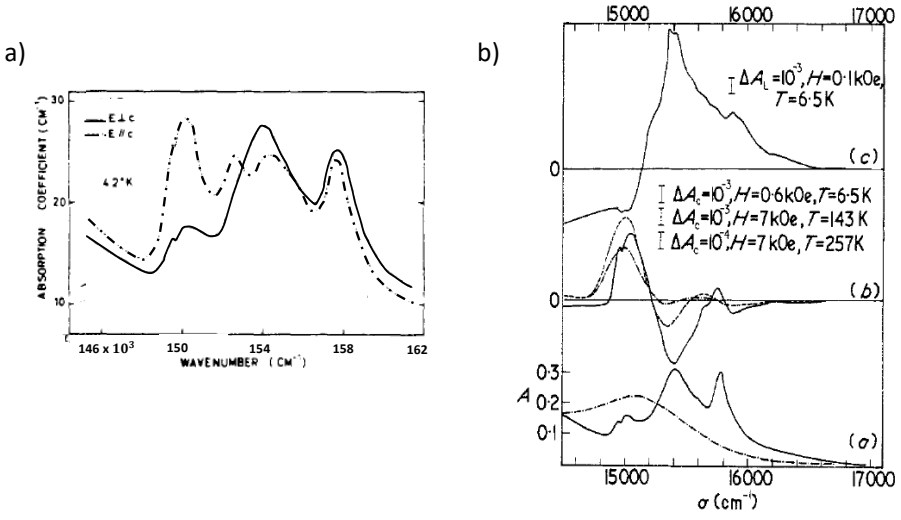

FIGURE 3.3: $3A_2 \rightarrow {}^1E^a$ transition. (a) Polarization dependence of the $RbNiF_3$ absorption spectrum [3]. (b) Magnetic Linear Dichroism (top), Magnetic Circular Dichroism (mid) and optical absorption spectrum (bottom) of $RbNiF_3$ [4].

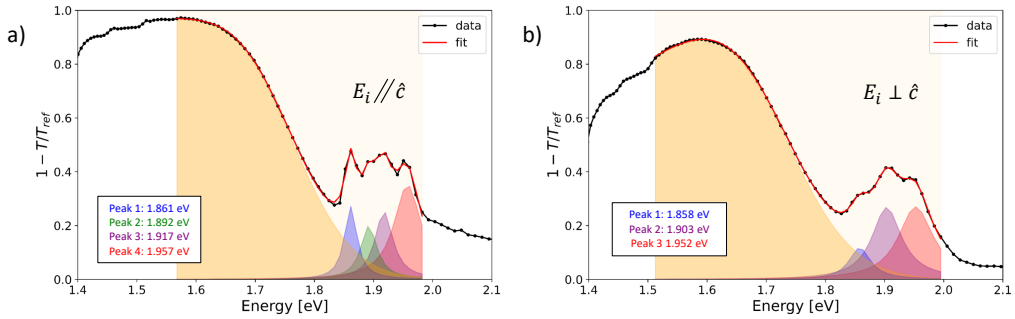

FIGURE 3.4: static response of $RbNiF_3$ at low temperature (T=10 K) obtained by using a broadband white-light pulse with polarization parallel (a) or orthogonal (b) to the $\hat{c}$ axis .

3.3 Static response

We start our investigation by characterizing the equilibrium response of $RbNiF_3$, looking for agreements with the results reported in literature.
We study a $350\,\mu m$ thick crystal of $RbNiF_3$ with in-plane $\hat{c}$-axis. To probe the static response, we measure the static transmissivity of the sample with broadband white-light pulses (1.4-$2.2\,eV$).

First, we test the polarization dependence of the static response to check if we can observe the changes in the lineshape of the $3A_2 \rightarrow {}^1E^a$ transition reported in [3] (Figure 3.3, a).
To highlight the absorption features of $RbNiF_3$, Figure 3.4 displays the fraction of light which is not transmitted by the sample as $1 - T/T_{ref}$, where T and T_{ref} represent the transmitted spectrum with/without the sample, respectively, and their ratio returns the transmittance of the sample[4]. Measurements are performed in the ferrimagnetic state of $RbNiF_3$ (T=10 K) with probe polarization[5] parallel (a) and orthogonal (b) to the $\hat{c}$ axis .

We isolate two distinct absorption features. In the 1.8-$2\,eV$ energy range, we observe a structured multi-peak that corresponds to the $3A_2 \rightarrow {}^1E^a$ *dd-transition* while at lower energies (1.4-$1.8\,eV$) there is a saturated absorption peak that, in analogy with the absorption spectrum of $KNiF_3$, we attribute to the $3A_2 \rightarrow {}^3T^1$ *dd-transition* [18, 19].
According to [3], the lineshape of the multi-peak transition changes by varying the orientation of the incoming polarization: four peaks are observed when $E_{incident} \parallel \hat{c}$, while three appear when $E_{incident} \perp \hat{c}$.

We fit the lineshape of the two transitions in the energy range 1.57-$2.0\,eV$ (shaded area in Figure 3.4) with a combination of multiple lorentzian functions (multi-peak) + skewed Gaussian (saturated absorption) curve. The fit function can be written as:

$$f(\omega) = \sum_{i=1}^{N} A_i \frac{\Gamma_i}{\Gamma_i^2 + (\omega - \omega_i)^2} + A_S\, e^{-\frac{(\omega-\omega_S)^2}{2\sigma_S^2}} \left\{1 + erf\left[\alpha(\omega - \omega_S)\right]\right\} \tag{3.1}$$

where *erf(x)* is the *error function* that accounts for the asymmetric shape of the saturated absorption peak (yellow area in Figure 3.4) and the number of peaks *N* depends on the

[4] Notably, the spectra reported in Figure 3.4 carry a contribution from both the absorbance and the reflectance of the sample.
[5] The polarization of the incoming pulse is controlled by a polarizer.

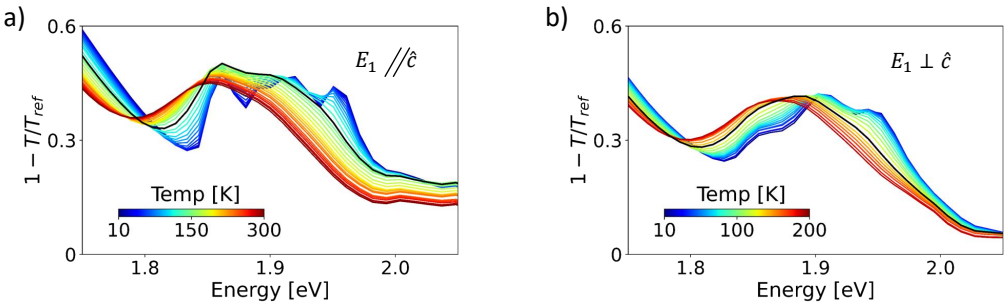

FIGURE 3.5: temperature dependence of the static response with $E_{incident} \parallel \hat{c}$ (a) and $E_{incident} \perp \hat{c}$ (b). Black line marks the Curie Temperature T_c=139 K.

orientation of the probe light with respect to the $\hat{c}$-axis (according to the results of [3], *N*=3 for $E_{incident} \perp \hat{c}$ and *N*=4 for $E_{incident} \parallel \hat{c}$ configuration).
The resulting central frequencies ω_i of the lorentzian peaks show a good agreement with the ones reported in [3] (Table 3.1).

$E_{incident} \parallel \hat{c}$		
ω_i	exp [eV]	Z&B [eV]
ω_1	1.861 ± 0.001	1.861
ω_2	1.892 ± 0.002	1.892
ω_3	1.917 ± 0.002	1.914
ω_4	1.957 ± 0.001	1.953

$E_{incident} \perp \hat{c}$		
ω_i	exp [eV]	Z&B [eV]
ω_1	1.858 ± 0.001	1.861
ω_2	1.903 ± 0.001	1.909
ω_3	1.952 ± 0.001	1.954

TABLE 3.1: comparison between the central frequencies of the lorentzian peaks obtained with the static fits and the values reported by Zanmarchi and Bongers in [3].

Temperature dependence

By increasing the sample's temperature, we follow the change of the absorption spectrum across the transition from ferrimagnetic-to-paramagnetic state. We do this for both configurations of probe polarization ($E_{incident} \parallel \hat{c}$ and $E_{incident} \perp \hat{c}$).

Figure 3.5 presents the static response measured at different temperatures when $E_{incident} \parallel \hat{c}$ (Figure 3.5 (a)) and with $E_{incident} \perp \hat{c}$ (Figure 3.5 (b)).
When temperature is increased, both *dd-transitions* experience a redshift, whether the incoming light is polarized parallel or orthogonal to the $\hat{c}$ axis. In addition, in both configurations there is a broadening of the multi-peak $3A_2 \rightarrow {}^1E^a$ transition that is consistent with previous observations [4].

To properly address the nature of the different sidebands, it is necessary to unveil their temperature dependence. In principle, this information can be extracted by our dataset by performing a static fit at each sample's temperature. However, the limited amount of sampling points in combination with the overlap of the different sidebands prevents us from resolving the different contributions.

In [3], Zanmarchi and Bongers isolated the temperature dependence of the different sidebands. When $E_{incident} \parallel \hat{c}$ and the temperature is increased, the intensity of the

$1.89\,\mathrm{eV}$ and $1.95\,\mathrm{eV}$ peaks (green and red peaks in Figure 3.4 (a)) decreases until both peaks disappear at T_c. When $E_{incident} \perp \hat{c}$, a similar behavior is experienced by the high energy sideband at $1.95\,\mathrm{eV}$ (red peak in Figure 3.4 (b)).

This evidence suggests a magnetic origin for the disappearing peaks. For both configurations, this observation matches the picture reported in [4] that associates the $1.95\,\mathrm{eV}$ peak (red peak in Figure 3.4) to the *exciton-phonon-magnon* transition, while $1.86\,\mathrm{eV}$ and $1.91\,\mathrm{eV}$ peaks are linked to *exciton* and *exciton-phonon* transitions, respectively.
Concerning the peak at $1.89\,\mathrm{eV}$ (green curve) that emerges when $E_{incident} \parallel \hat{c}$, Zanmarchi and Bongers address its origin to an *exciton+magnon* transition [3].

3.4 Dynamic measurements

Having characterized the equilibrium response of the sample, we add a second ultrashort pulse to perform pump-probe measurements. The versatility of our setup (Figure 3.6) gives us the opportunity to adopt different experimental configurations. In particular, we can employ pump pulses in the visible-NIR range to match the energies of $RbNiF_3$ optical transitions (*Pump 1* in Figure 3.6) or use low-energy MIR pulses (*Pump 2*) to have non-resonant pumping.
Moreover, we can select the polarization of the scattered probe by means of a polarizer placed after the sample.
We monitor the white-light stability by splitting the probe beam before the sample and by measuring the non-interacting portion on a second detector (*Channel 0* in Figure 3.6).

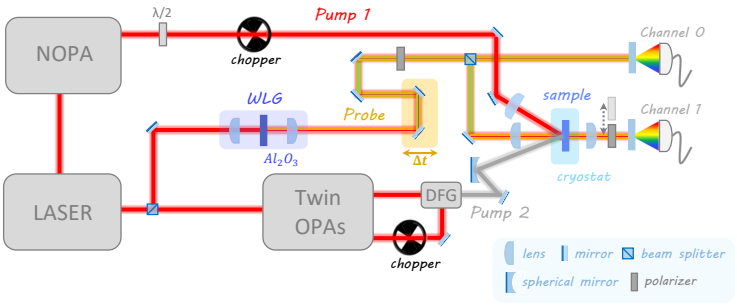

FIGURE 3.6: detailed scheme of the experimental setup. The last polarizer can either be inserted or removed, according to the experiment, to select the polarization of the scattered probe light.

3.4.1 PP measurements with no polarization selection

We start our investigation by employing a pump pulse resonant to the low-energy $^3A_2 \rightarrow {}^3T^1$ *dd*-transition ($\phi_{pump}^{incident} \sim 1\,\mathrm{mJ\,cm^{-2}}$) and by measuring the whole transmitted light, with no polarization selection. In this way we can directly connect the spectral response of the PP measurement to the optical transitions previously characterized (Figure 3.4).

We probe the transient transmissivity, derived as $\Delta T/T = (T_p - T_u)/T_u$ (see Chapter 2), with the broadband WL pulse used for the static measurements (T_p and T_u indicate the transmitted spectra acquired when the pump is present or blocked). In Figure 3.7, we show the resulting PP map obtained at T=$10\,\mathrm{K}$ when the probe polarization is set parallel to $\hat{c}$.
All the dynamic measurements presented in this Chapter have been carried out with the polarization of the pump $\hat{e}_{pump}$ set parallel to the probe polarization $\hat{e}_{probe}$.

The pump excitation generates a long-living signal that persists at negative times. Notably, besides some weak oscillations at positive times, we do not track any temporal evolution of the signal (see Figure 3.7, c). Since the experiment is performed with a laser repetition rate of $10\,\mathrm{kHz}$ and a chopping frequency of the pump of $45\,\mathrm{Hz}$, we estimate the lifetime of the transient signal to be $100\,\mu\mathrm{s} < \tau < 20\,\mathrm{ms}$.
To understand if such signal is compatible with a thermal signal, we estimate the time necessary to dissipate the accumulated heat by calculating the thermal diffusivity of the material. For $RbNiF_3$ the values of the thermal conductivity and of the specific heat

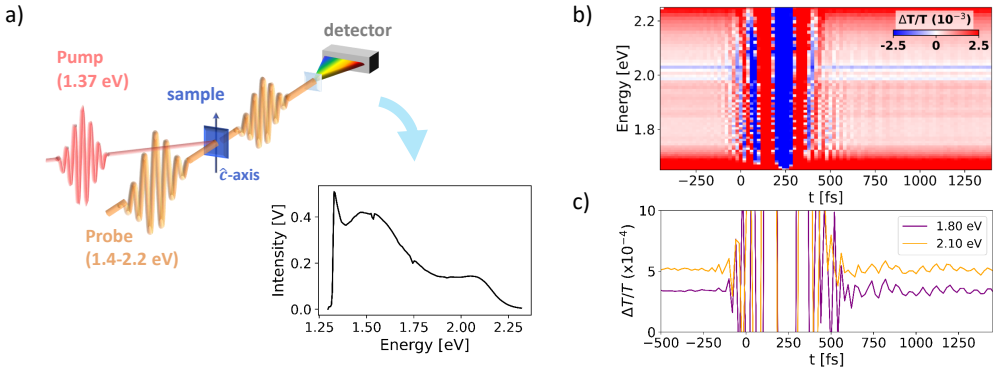

FIGURE 3.7: (a) experimental arrangement of the PP setup without the selection of the scattered probe polarization. Inset shows the spectrum of the white-light probe before the interaction with the sample. (b) pump-probe map with pump and probe polarization parallel to $\hat{c}$. We measure a long living signal that persists at negative times. Considering the repetition rate of the laser ($10\,\mathrm{kHz}$) and the chopping frequency of the pump ($45\,\mathrm{Hz}$) we set two boundaries to the lifetime of the transient signal: $100\,\mu\mathrm{s} < \tau < 20\,\mathrm{ms}$. At positive times, weak oscillations are visible. (c) horizontal cuts of the PP map.

capacity aren't available: hence, we performed the calculation for the parent compound $KNiF_3$ [20, 21], obtaining $\alpha \sim 39.9\,\mathrm{m^2\,s^{-1}}$ and, on a distance of $300\,\mu\mathrm{m}$, a diffusion time $t_d \sim 2\,\mathrm{ns}$.
The great discrepancy that we observe between the diffusion time t_d[6] and the lifetime of the transient signal τ suggests a non-thermal contribution to the long-living transient signal. We test this hypothesis in the next Section.

In Figure 3.8 (a) and (b) we present the vertical cuts ($\Delta t = -250\,\mathrm{fs}$) of the PP maps obtained with $E_{incident} \parallel \hat{c}$ and $E_{incident} \perp \hat{c}$, respectively. We observe a non trivial spectral dependence of the signal characterized by multiple peaks.
Starting from the static fit function which describes $f = 1 - T/T_{ref}$, we develop a *dynamic model* to fit the transient signal and link it to the equilibrium response. In particular, we can write:

$$\frac{\Delta T}{T} = \frac{T_p - T_u}{T_u} = \frac{\frac{T_p}{T_{ref}} - \frac{T_u}{T_{ref}}}{\frac{T_u}{T_{ref}}} = \frac{(1 - f_p) - (1 - f_u)}{(1 - f_u)} \tag{3.2}$$

where $f_u = f(\omega, p_u)$ is the static fit function of equation 3.1 with the parameters p_u that describe the static response and $f_p = f(\omega, p_p)$ is the same fit function with the parameters p_p which have to be determined by the dynamic fit.

The result of the dynamic fit is plotted in Figure 3.8 ((a) and (b), orange trace). The dynamic model well reproduces the observed signal up to $1.96\,\mathrm{eV}$, matching the peaks that appear in correspondence of the $3A_2 \rightarrow {}^1E^a$ sidebands (gray dashed lines).
However, at higher energies the model completely fails in describing the feature centered at $2.01\,\mathrm{eV}$ (purple dashed lines) that is present in both configurations. Consequently, the static model has to be modified in order to reproduce the dynamic response.

[6] Our calculations have been performed for the parent compound $KNiF_3$, but we still expect the diffusion time t_d of $RbNiF_3$ to be of the same order of magnitude.

We notice that all the peaks that are present in the transient signal occur in correspondence of a lorentzian sideband (gray dashed lines). By analogy, we theorize the presence of an additional sideband centered at $2.01\,\mathrm{eV}$.

We perform a new fit of the transient signal with a modified model that includes an *extra-peak* at $2.01\,\mathrm{eV}$. We point out that the limited amount of experimental points prevents us from performing a robust quantitative analysis of the *extra-peak* features, e.g. amplitude/linewidth. Nonetheless, the result of the fit returns a satisfactory qualitative agreement with the data (red trace) for both $E_{incident} \parallel \hat{c}$ and $E_{incident} \perp \hat{c}$ configurations, proving that the presence of an extra-sideband is needed to describe our data.
Unfortunately, even if the transient signal associated to the *extra-peak* is very pronounced, we can't find an unambiguous evidence of the $2.01\,\mathrm{eV}$ peak in the static response, signifying that the equilibrium peak is expected to be very weak. Nonetheless, we underline that the magnetic linear dichroism experiment reported in [4] (Figure 3.3 (b), top) shows a signal right at the energy of $16.200\,\mathrm{cm}^{-1}$, in excellent agreement with our experimental evidence.

To address the origin of the *extra-peak*, we track the evolution of the transient signal at different temperatures (Figure 3.8, (c) and (d)). Interestingly, in both configurations the *extra-peak* is completely indistinguishable above $40\,\mathrm{K}$, i.e. well below T_c.
We point out that we track signatures of the other lorentzian peaks up to $150\,\mathrm{K}$, confirming that the vanishing of the signal is not related to a degradation of the experimental sensitivity.

The suppression of the *extra-peak* that occurs when the temperature is increased suggests that the relative transition is not determined by a multiphonon process (*exciton+phonon+phonon*). On the contrary, we expect the *extra-peak* to be connected to the presence of long-range magnetic order and hence to have a magnetic character. From this perspective, the big discrepancy between the temperature at which the signal vanishes ($40\,\mathrm{K}$) and the Curie temperature ($139\,\mathrm{K}$) can be attributed to the loss of spin-spin correlation length, as in the case of NiO [22, 23].

Finally, after noticing that the distance between the *extra-peak* and the *exciton-phonon* peak (purple peaks in Figure 3.4) is roughly twice the distance between the latter and the *exciton-phonon-magnon* sideband (red peaks in Figure 3.4), we advance the hypothesis that the *extra-peak* at $2.01\,\mathrm{eV}$ is related to an *exciton+phonon+2-magnon* transition[7].

[7] We underline that both the creation of a *2-magnon* excitation and the *exciton+phonon+magnon* process involve magnons at the edge of the Brillouin zone [4, 14].

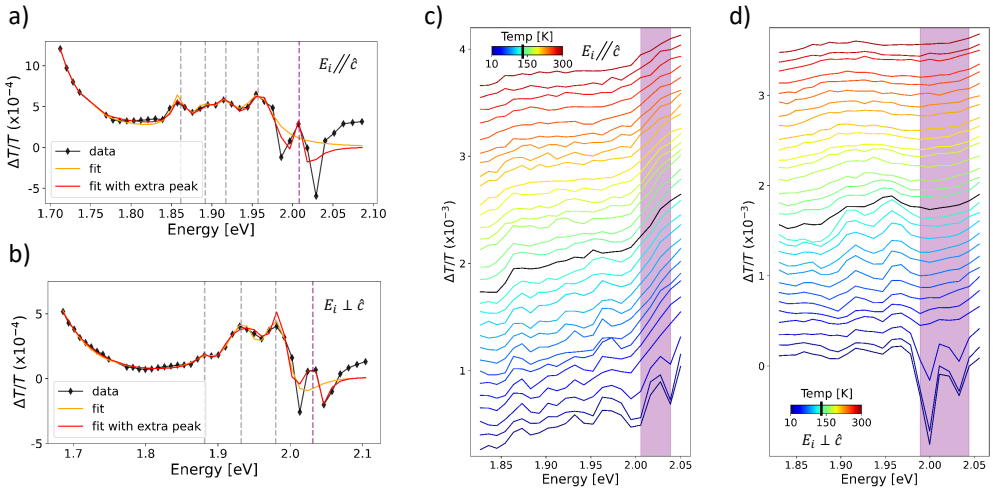

FIGURE 3.8: cuts of the long living transient signal taken at $\Delta t = -250\,\mathrm{fs}$. (a) and (b) display the cuts at T=10 K obtained with $E_{incident} \parallel \hat{c}$ and$E_{incident} \perp \hat{c}$. (c) and (d) present the temperature dependence of the long-living signal for the $E_{incident} \parallel \hat{c}$ and $E_{incident} \perp \hat{c}$ configurations.

3.5 Extinction geometry

In the previous section, we unveiled a long-living transient signal with a possible non-thermal origin. In particular, it is known that $RbNiF_3$ exhibits magneto-optical effects at equilibrium, like Faraday rotation [2]. Hence, we advance the hypothesis that the origin of the dynamic response is a transient magneto-optical Faraday effect, i.e. a rotation of the probe polarization mediated by the action of the pump.

To test this hypothesis, we need to remodel our setup and achieve sensitivity to changes of the probe polarization. The straightforward solution is to insert a polarizer before the detection [24] (Figure 3.9).
In addition, a selection of the detected polarization allows for the isolation of coherent excitations according to their symmetry. We perform PP measurements in *extinction geometry* to study E_{1g} modes (Appendix A), the most dominant excitations in the low frequency regime [14, 17].

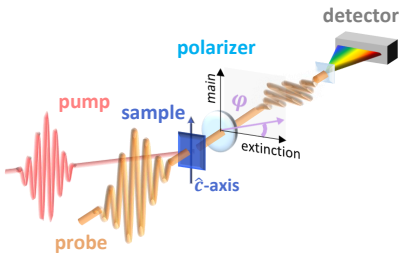

FIGURE 3.9: setup for the PP experiments in *extinction geometry*.

The results of the pump-probe experiment in extinction geometry are plotted in Figure 3.10. In particular, Figure 3.10 (a) and (b) show the pump-probe maps correspondent to the $1.37\,\mathrm{eV}$ (resonant) and $0.12\,\mathrm{eV}$ (non-resonant) pump excitations[8] with $\hat{e}_{pump} \parallel \hat{e}_{probe} \parallel \hat{c}$. Similar results are obtained when the beams are polarized $\perp \hat{c}$.
In Figure 3.10 (a) a long-living signal dominates the transient response of the material. Notably, the intensity of the signal is >10 times higher than the one observed with no selection of the probe polarization (Figure 3.7). This confirms that polarization rotation plays a major role in determining the long-living signal.

On the contrary, the low energy pump triggers just periodic oscillations and no incoherent signal is detected (Figure 3.10, b). The resonant nature of the effect is discussed in the next paragraph.
Finally, by looking at the vertical cuts of the PP maps at negative times $\Delta t = -250\,\mathrm{fs}$ (Figure 3.10, c), we highlight the temperature dependence of the long-living signal. The reduction of the transient signal at high temperatures possibly establishes a link with the magnetic ordering of the sample.

[8] Since the absorption coefficient of $RbNiF_3$ is different for the two pump energies, we increased the incoming fluence of the low energy pump (which is the less absorbed) by a factor of 2. We ensured that the fluence of the two pumps was the same by comparing the amplitude of the transient signal at the temporal overlap.

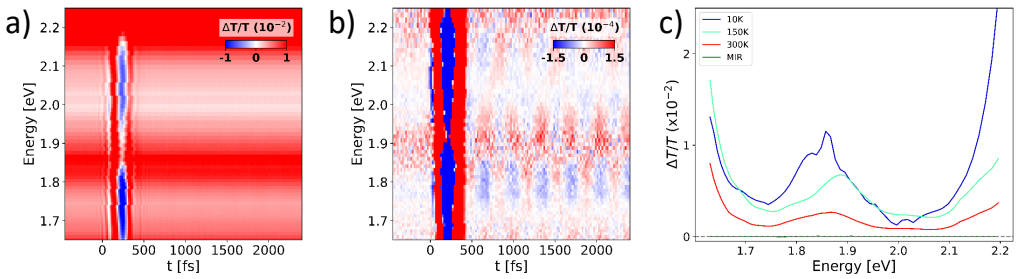

FIGURE 3.10: PP maps obtained in extinction geometry ($\hat{e}_{pump} \parallel \hat{e}_{probe} \parallel \hat{c}$) with E_{pump}=1.37 eV (a) and E_{pump}=0.12 eV (b). In (c) we display the vertical cuts of the maps at negative times ($\Delta t = -250$ fs) for different temperatures.

Ultrafast response

In Figure 3.11 we present the pump-probe map at T=10 K obtained with the high energy pump (Figure 3.10, a) subtracted by the 'quasi-static' response at negative times. In this way, we highlight the ultrafast changes of the dynamic response.
We distinguish two contributions at positive times: an incoherent signal (i.e. positive and negative bands at 1.9/2.2 eV and 1.65/2.0 eV, respectively) and coherent oscillations. We start our investigation from the incoherent signal and in the subsequent section we discuss the coherent contributions.

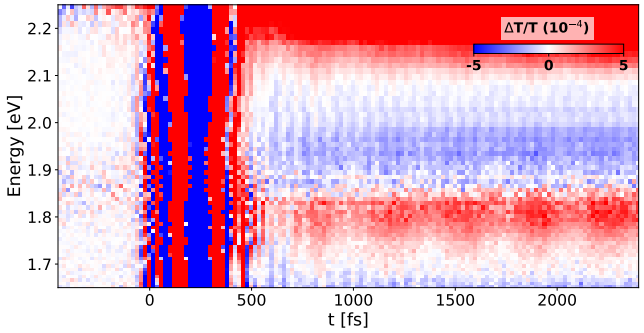

FIGURE 3.11: ultrafast response at 10 K with $\hat{e}_{pump} \parallel \hat{e}_{probe} \parallel \hat{c}$. PP map obtained by subtracting the signal at negative times from the map of Figure 3.10 (a).

3.5.1 Incoherent signal

To isolate the incoherent signal, we mediate the $\Delta T/T$ signal of Figure 3.11 in the temporal window 1500-1900 fs and plot the resulting trace at different temperatures (Figure 3.12, a).
Interestingly, a temperature increase causes a redshift of the curve but doesn't significantly change the amplitude of the signal.

In order to understand if the signal is originated by a change of the probe polarization, we perform a series of equilibrium measurements where we rotate the final polarizer by an angle ϕ with respect to the extinction geometry (ϕ=0°) (Figure 3.9). In such manner, we derive the transient signal associated to a purely static rotation of polarization $\Delta T_{rot}/T = (T_\phi - T_0)/T_0$, where T_ϕ and T_0 are the transmitted equilibrium spectra obtained with a rotation of the polarizer of ϕ and 0° with respect to the extinction geometry.

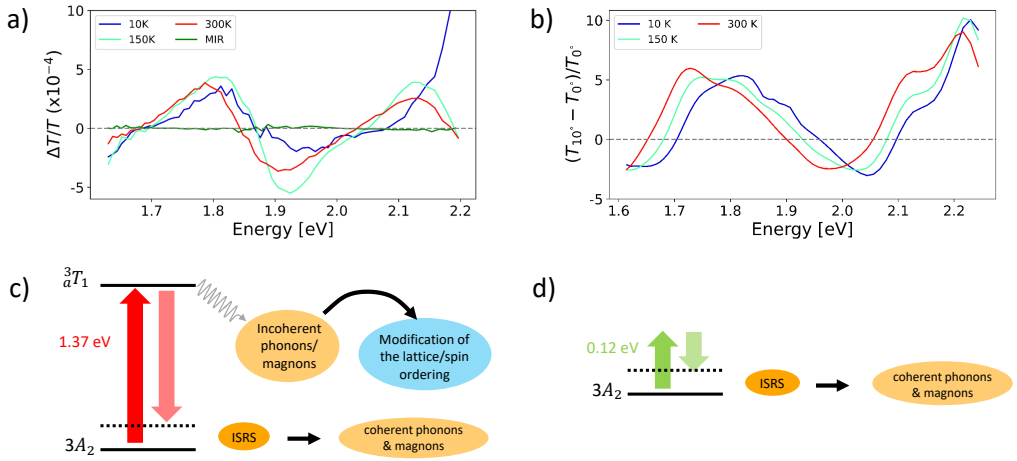

FIGURE 3.12: incoherent signal. (a) Vertical cuts of of the dynamic signal (Figure 3.11) integrated in the time window 1500-1900 fs for different temperatures and pump energies. (b) signal generated by a static rotation of polarization. The resonant character of the incoherent signal originates from the different mechanisms that take place when the 1.37 eV (c) or the 0.12 eV pump (d) excite the system.

The results (Figure 3.12, b) qualitatively reproduce the shape and the temperature dependence of the incoherent signal, thus confirming that it stems from the transient magneto-optical Faraday effect.

Remarkably, by using a low energy pump pulse (0.12 eV), we detect no incoherent signal on short times (Figure 3.12 (a), green trace), as we observed on long timescales (see Figure 3.10, b). This implies that no change in the probe polarization occurs with the MIR pump.
Since the absorption coefficient is different for the 1.37 eV and the 0.12 eV pump, we could picture a process in which the system is characterized by a temperature dependent Faraday effect and we indirectly observe the sample heating caused by the pump pulse. In this scenario, just in the case of the resonant pump at 1.37 eV[9], the sample increases its temperature and hence the Faraday rotation angle experienced by the probe pulse changes with respect to equilibrium.
From this perspective, it is true that $RbNiF_3$ exhibits a temperature dependent Faraday effect [25], but such effect is zero above T_c, while we observe it also at room temperature. Therefore, even if the aforementioned mechanism takes place, it is not the one which leads to our experimental observations.

Instead, since the 1.37 eV pump pulse is resonant with the $3A_2 \rightarrow {}^3T^1$ *dd*-transition while the 0.12 eV pulse isn't resonant with any electronic transition of $RbNiF_3$, we draw a parallelism with the experiment on $KNiF_3$ reported in [6] and frame the following mechanism.
When the pump is resonant to the *dd*-transition, excited *dd* states are populated and relax via incoherent phonons and magnons. The generation of incoherent excitations modifies the lattice/spin environment (e.g. by changing the correlation length of the spin system) and determines a transient Faraday effect (Figure 3.12, c).

[9]Which is the pump energy with the higher absorption coefficient. In this perspective, we recall that we increased the incoming fluence of the low energy pump to account for the difference in the absorption coefficient.

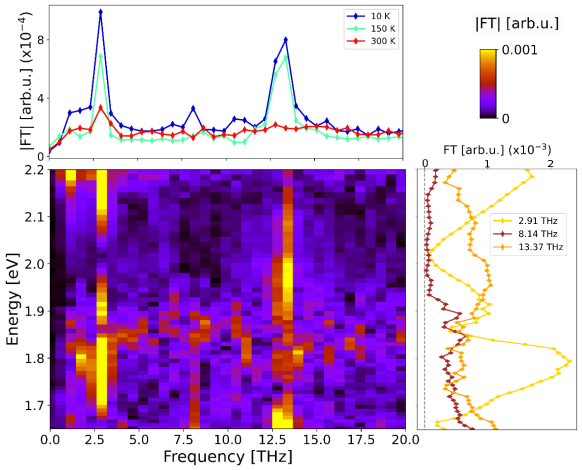

FIGURE 3.13: coherent signal. 2D map of the FT signal as a function of excitation frequency (horizontal axis) and probe energy (vertical axis). Upper panel displays the energy-integrated cuts of the 2D map at three temperatures. Right panel shows the spectral dependence of the $2.9/8/13\,\mathrm{THz}$ excitations (vertical cuts of the 2D map).

On the contrary, when the pump energy is too low to trigger the electronic transition, the only process that takes place is Impulsive Stimulated Raman Scattering and no altering of the vibrational/magnetic environment occurs (Figure 3.12, d).

In this picture, we do not distinguish between a transient Faraday effect generated by a modification of the lattice or by a change of the spin environment.
Indeed, we underline that the interpretation of the experiment isn't univocal, since the amplitude of the ultrafast incoherent signal doesn't change across the phase transition (Figure 3.12, a) while the long-lasting signal is smaller when the magnetic order is lost (Figure 3.10, c).
In the spirit of light-induced phenomena [11, 26–28], we just point out that the evidence of a signal at high temperatures could be linked to a pump-induced enhancement of short range magnetic order. Indeed, optical manipulation of spin and magnetic order is a well-known phenomenon [29–32] and specifically studies on NiO [33, 34] proved that the excitation of Ni^{++} *dd* electrons can lead to an ultrafast reorientation of the spin system.

3.5.2 Coherent oscillations

PP map in Figure 3.11 shows a periodic modulation at positive times. To address the nature of the coherent oscillations, we remove the background signal (fitted with polynomial curves) and perform the Fourier Transform of the temporal traces for each spectral component.
The resulting spectra are packed in a 2D map that displays the intensity of the FT as a function of oscillation frequency and pulse energy (Figure 3.13).

We distinguish two intense oscillations at 2.9 and $13\,\mathrm{THz}$ and a weaker signal at $8\,\mathrm{THz}$[10]. While the slow oscillations at $2.9/8\,\mathrm{THz}$ can unambiguously be attributed to E_{1g} phonon modes [17], the fast oscillation could either be associated to the $12.5\,\mathrm{THz}$

[10]Notably, the same Fourier analysis performed on the PP maps obtained with the low energy pump (Figure 3.10, b) returns a single slow oscillation at $2.9\,\mathrm{THz}$. This is due to the longer temporal duration of MIR pulses (>100 *fs*) that inhibits the coherent excitation of fast modes.

A_{1g} phonon[11] or to the tail of the broad 2-magnon excitation peaked at $14\,\mathrm{THz}$ [14], assuming that the temporal duration of our pump pulse ($\sim$25 *fs*) prevents us from resolving contributions at higher frequencies.

The spectral-integrated FT traces acquired in the ferrimagnetic ($10\,\mathrm{K}$) and paramagnetic state ($300\,\mathrm{K}$) and just above the transition temperature ($150\,\mathrm{K}$) are displayed in the upper panel of Figure 3.13.
Oscillations at $2.9/13\,\mathrm{THz}$ experience a strong reduction across the phase transition and only the 2.9 mode is detected at room temperature.The weak $8\,\mathrm{THz}$ oscillation already disappears at $150\,\mathrm{K}$.

We point out that, with our spectral resolution, it is hard to discriminate if there is frequency-shift of the $13\,\mathrm{THz}$ peak position that could be linked to the softening of the 2-magnon excitation. For this reason, we perform the same experiment in the orthogonal configuration ($E_{pump} \parallel E_{probe} \perp \hat{c}$, see Appendix B) and we compare it with the Raman spectra of $RbNiF_3$ acquired at different temperatures with high frequency resolution (see Appendix C).
The results of these two experiments show that the high energy A_{1g} mode has a temperature dependence which perfectly matches the one observed in PP measurements for the $13\,\mathrm{THz}$ excitation. Therefore, we conclude that the origin of the high energy peak is purely vibrational.

In addition, we reconstruct the intensity profile of the coherent excitations as a function of the probe energy by performing vertical cuts of the 2D FT map (Figure 3.13, right panel).
We unveil a non-trivial spectral dependence for each of the three observed excitations: the $2.9\,\mathrm{THz}$ oscillation presents three dips at the probe energies of $1.65/1.85/2.0\,\mathrm{eV}$, the $8\,\mathrm{THz}$ oscillation is localized at energies lower than $1.9\,\mathrm{eV}$ and the $13\,\mathrm{THz}$ mode has a quasi-uniform spectrum.
These evidences hint at a different coupling of the three excitations with the electronic degrees of freedom that govern the absorption spectrum.

To complete this picture, we extend our study to the phase of the FT traces. Figure 3.14 (a) depicts the spectral dependence of the FT phase for the three excitations.
The 2.9 mode experiences abrupt phase shifts in coincidence with the amplitude drops previously reported. The $8\,\mathrm{THz}$ mode presents a constant phase throughout the whole region where the FT intensity is non-zero (1.6-$1.9\,\mathrm{eV}$). Finally, the $13\,\mathrm{THz}$ oscillation shows a single phase shift just below $1.8\,\mathrm{eV}$.

Interestingly, the phase shifts of the 2.9 mode ($1.85/2\,\mathrm{eV}$) occur in correspondence of the first and last peak of the multi-peak *dd*-transition, namely the first excitonic peak (blue peak in Figure 3.4) and the extra peak unveiled by our analysis on the long-living signal (Figure 3.8).
Since phase shifts are associated to frequency shifts or changes in oscillators linewidths, we recall the dynamic model (equation 3.2) to simulate the transient signals associated to each of the aforementioned changes. We reproduce the spectral dependence of the slow mode by modulating the central frequencies of the two oscillators (Figure 3.14 (b), left). Importantly, the two coordinates oscillate in antiphase, resulting in a change of the intra-peak distance.

[11] This value refers to the one measured in [14].

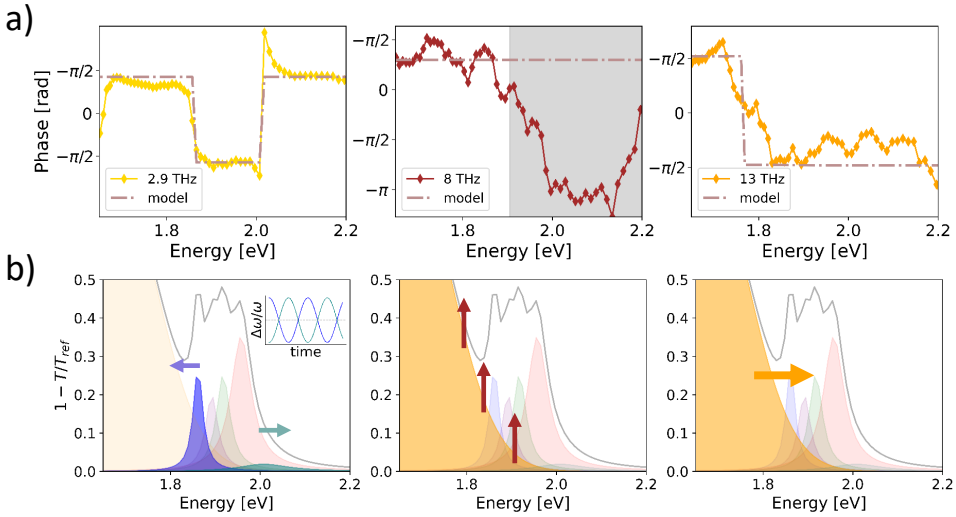

FIGURE 3.14: FT phase spectral dependence. In (a) we plot the FT phase of the 2.9 (left), 8 (central) and 13 THz mode (right) as a function of the probe energy (gray shaded area marks the region where $|FT|$=0). We reproduce the observed spectral dependence (brown dashed line in (a)) with three different dd-phonon coupling mechanisms (b). Specifically, 2.8 mode is caused by a frequency shift (in antiphase) of the external peaks of the $3A_2 \rightarrow {}^1E^a$ transition , while 8/13 THz oscillations originate from an amplitude/linewidth change of the $3A_2 \rightarrow {}^3T^1$ transition.

In analogy, we mimic the behavior of the 8 THz mode with an amplitude modulation of the low energy *dd*-transition (Figure 3.14 (b), center) and the 13 THz mode with a variation of its spectral linewidth (Figure 3.14 (b), right).

Discussion

As reported in recent works [35, 36], we unveil the presence of *dd-phonon coupling* by looking at the spectral dependence of coherent oscillations. Moreover, we draw a picture where the three excited phonons link differently to the electronic degrees of freedom: the 2.9 mode is associated to a periodic translation of the two external peaks of the $3A_2 \rightarrow {}^1E^a$ transition, while 8 and 13 THz modes connect respectively to an amplitude and bandwidth modulation of the saturated $3A_2 \rightarrow {}^3T^1$ transition.

To address the origin of the different coupling mechanisms, we look at the atomic displacements of the specific phonon modes. DFT calculations (see Appendix D) return the following evidence: high frequency modes (8/13 THz) connect to the motion of Ni and F atoms while the low energy phonon (2.9 THz) involves also the displacement of Rb atoms.
From this observation, we frame the following picture. When high frequency phonons are involved, Ni atoms are displaced from their equilibrium positions, determining a change in the crystal field. As a consequence, the electron orbital states of Ni, including the *dd* states, are renormalized.

In the case of the low energy phonon (2.9 THz), the displacement of Ni atoms is small with respect to F and Rb atoms. Hence, we expect Rubidium and Fluorine atoms to determine dd-phonon coupling. In particular, the motion of F atoms (or of Rb atoms,

indirectly) determines a change in the $Ni - F - Ni$ angles inside the unit cell and hence modulates the superexchange interaction between neighbouring Ni atoms.
Consequently, magnetic properties are modulated and in particular we speculate that the frequency of the 2-magnon excitation is varied. Indeed, this frequency change would determine a change of the intra-peak distance between the *exciton* and the *exciton+phonon+2magnon* transitions, in analogy with our findings (Figure 3.14 (b), left).

We point out that this qualitative picture misses three important aspects. First, it doesn't predict the different coupling of the 8 and $13\,\mathrm{THz}$ modes with the $3A_2 \rightarrow {}^3T^1$ transition. Secondly, it isn't clear why a variation of the superexchange interaction should modulate, besides the *exciton+phonon+2magnon* peak, also the *excitonic* transition. Third, the model doesn't explain why the motion of Fluorine atoms (and hence their impact on the superexchange interaction) is relevant just for the $2.9\,\mathrm{THz}$ mode and not for the high frequency ones.
Starting from the first point, we claim that a calculation of the *dd* orbitals and a deeper analysis of the specific motion of Ni atoms should be included in the model to properly address the difference between the two couplings.
Regarding the second point, we do not have a straightforward reply that reconciles our model with the current interpretation of the $3A_2 \rightarrow {}^1E^a$ sidebands [4]. Possibly, other interpretations of the $3A_2 \rightarrow {}^1E^a$ transition than the one of Pisarev et al. [4] should be considered.
Finally, the third point suggests that, in addition to the motion of F atoms, other elements should be taken into account in the case of the slow energy mode, e.g. the action of Rb atoms.

3.6 Conclusions

In this Chapter we reported the non-equilibrium study of the low-temperature ferrimagnet $RbNiF_3$. After characterizing the static response of the sample, we studied the long-living transient response triggered by the $1.37\,\mathrm{eV}$ pump excitation. By fitting the non-equilibrium signal, we unveiled the presence of an additional sideband centered at $2.01\,\mathrm{eV}$, that we linked to an exciton-phonon-2magnon transition.

We addressed the origin of the transient signal to a resonant transient-Magneto-Optical-Faraday effect by performing polarization resolved measurements with different pump energies ($1.37/0.12\,\mathrm{eV}$). In particular, we pictured a process where excited *dd* electrons relax into incoherent phonons/magnons, generating a metastable distortion of the lattice/magnetic order that induces the rotation of the pulse polarization.

Finally, we isolated three coherent modes at $2.9/8/13\,\mathrm{THz}$ that we identified as E_{1g} ($2.9/8\,\mathrm{THz}$) and A_{1g} ($13\,\mathrm{THz}$) phonon modes after performing temperature-dependent measurements.
We addressed an anomalous spectral dependence of the three excitations that we explained with different *dd-phonon coupling* mechanisms. In details, the slow oscillation ($2.9\,\mathrm{THz}$) was linked to an antiphase oscillation of the central frequencies of the $3A_2 \rightarrow {}^1E^a$ external peaks, while the $8/13\,\mathrm{THz}$ oscillations were associated to an amplitude/linewidth modulation of the $3A_2 \rightarrow {}^3T^1$ transition. We theorized that the different couplings are determined by the specific atomic displacements and by their mapping onto the electronic and magnetic degrees of freedom.

Appendices

A First order Raman tensor for D_{6h} symmetry group

According to [37], we write the Raman tensors for the excitations of the D_{6h} symmetry group:

$$A_{1g} = \begin{pmatrix} a & 0 & 0 \\ 0 & a & 0 \\ 0 & 0 & b \end{pmatrix} E_{1g,1} = \begin{pmatrix} 0 & 0 & 0 \\ 0 & 0 & c \\ 0 & c & 0 \end{pmatrix} E_{1g,2} = \begin{pmatrix} 0 & 0 & -c \\ 0 & 0 & 0 \\ -c & 0 & 0 \end{pmatrix}$$
$$E_{2g,1} = \begin{pmatrix} d & 0 & 0 \\ 0 & -d & 0 \\ 0 & 0 & 0 \end{pmatrix} E_{2g,2} = \begin{pmatrix} 0 & -d & 0 \\ -d & 0 & 0 \\ 0 & 0 & 0 \end{pmatrix}$$

from which we write the susceptibility tensor:

$$\chi_{ijk} = \begin{pmatrix} a+d & -d & -c \\ -d & a-d & c \\ -c & c & b \end{pmatrix}$$

According to the specific geometry of the experiment (z axis is in plane), we reduce it to:

$$\chi_{ij} = \begin{pmatrix} a-d & c \\ c & b \end{pmatrix}$$

We notice that the only relevant modes are A_{1g}, $E_{1g,1}$ and $E_{2g,1}$.
We now consider the action of the probe pulse with linear polarization. We define the polarization of the impinging probe as $(cos\theta, sin\theta)$ and the measured one (selected by the analyzer) $(cos\alpha, sin\alpha)$, where both θ and α are defined with respect to the sample $\hat{c}$-axis. We obtain the following angle dependence of the transient transmissivity:

$$\begin{aligned} \Delta T(\theta,\alpha) &= \begin{pmatrix} cos\alpha, & sin\alpha \end{pmatrix} \begin{pmatrix} a-d & c \\ c & b \end{pmatrix} \begin{pmatrix} cos\theta \\ sin\theta \end{pmatrix} \\ &= (a-d)\, cos\theta\, cos\alpha + c\, sin\theta\, cos\alpha + c\, cos\theta\, sin\alpha + b\, sin\theta\, sin\alpha \end{aligned}$$

By setting the analyzer angle at $\alpha = \theta + 90°$ (*extinction geometry*) we get:

$$\Delta T(\theta) = \frac{d-a+b}{2} sin2\theta + \frac{c}{2} cos2\theta$$

Therefore, we isolate $E_{1g,1}$ modes by probing at $\theta = 0°/90°$ and A_{1g} and $E_{2g,1}$ modes by probing at $\theta = 45°$.

We performed measurements just in the first configuration ($\theta = 0°/90°$), but apparently a residual contribution of A_{1g} and $E_{2g,1}$ modes can still be detected, as reported in [17].

B Coherent oscillations with orthogonal configuration

In this Appendix we display the 2D FT map of the coherent oscillations obtained at T=10 K and with $E_{probe} \perp \hat{c}$ (Figure B.1). With respect to the map obtained with the parallel configuration ($E_{probe} \parallel \hat{c}$, Figure 3.13), the coherent signals are more intense and additional contributions are unveiled (e.g. $10\,\mathrm{THz}$).
Importantly, the spectral integrated traces measured at different temperatures (Figure B.1, top panel) show that the $13\,\mathrm{THz}$ mode is the combination of two different components: the high energy contribution vanishes by increasing the temperature while the low energy one survives across the phase transition.

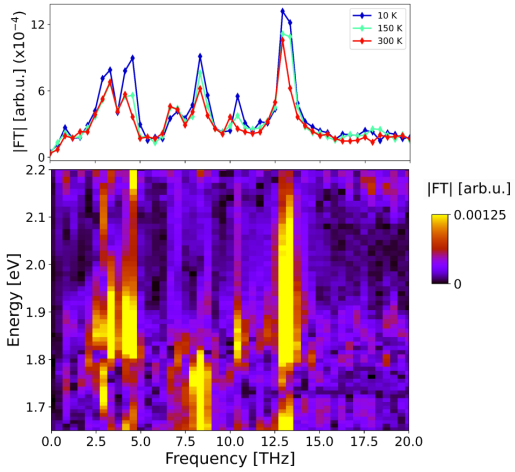

FIGURE B.1: 2D FT map of the coherent oscillations obtained with $E_{probe} \perp \hat{c}$ at T=10 K. Top panel displays the spectral-integrated maps at three different temperatures.

C Raman measurements

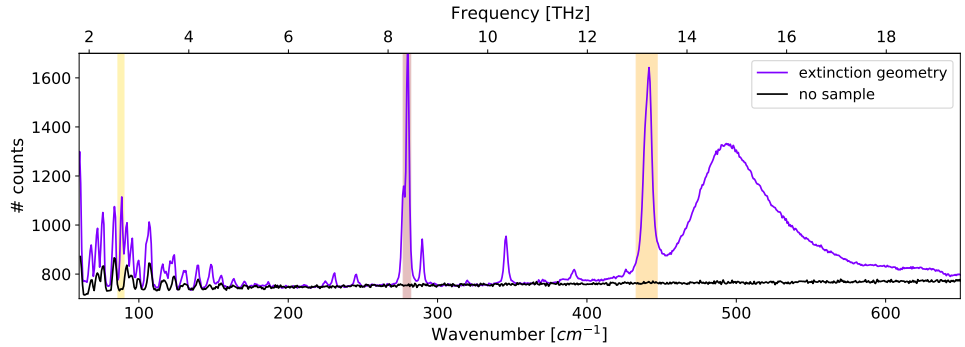

FIGURE C.1: Raman spectrum of $RbNiF_3$ obtained by measuring the cross-polarized photons (*extinction geometry*) scattered by the unoriented sample at T=10 K. Shaded areas highlight the phonon modes that we measured in Section 3.5.2. Black curve reports the spectrum of scattered light when the impinging beam is focused out of the sample.

In this Appendix we present the results of Raman measurements performed on $RbNiF_3$ with a *Trivista* (Triple Monochromator, $S\&I$) System. Measurements have been done by employing a continuous laser with a central wavelength of $532\,\mathrm{nm}$. Figure C.1 reports the spectrum obtained in the ferrimagnetic state of the sample (T=10 K) in the 50-650 cm^{-1} energy range. We report also the Raman spectrum obtained by moving the focus out of the sample (black curve in Figure C.1) to highlight the Raman peaks which are not related to the sample itself but to other scattering sources, e.g. air or vacuum chamber window. The measurement is performed in *extinction geometry* to have a direct comparison with the data presented in Section 3.5.2. Notably, we observe the intense 2-magnon peak centered at $500\,\mathrm{cm}^{-1}$ and the three phonon peaks at $89\,\mathrm{cm}^{-1}$ (2.67 THz), $279\,\mathrm{cm}^{-1}$ (8.4 THz) and $440\,\mathrm{cm}^{-1}$ (13.2 THz) that we previously measured (Section 3.5.2).

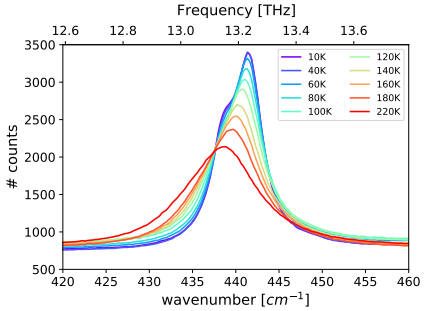

FIGURE C.2: Temperature dependence of the A_{1g} phonon mode. To improve the visibility of the mode, this measurement is performed in *parallel geometry*. Notably, at low temperatures the peak consists of a doublet.

We exploit the high frequency resolution of the Raman apparatus to study the temperature dependence of the high frequency A_{1g} phonon (13.2 THz). The result of the temperature study[12] is displayed in Figure C.2.
Interestingly, the low temperature measurements show that the 13.2 THz mode consists of a doublet which redshifts and broadens by increasing the temperature.

[12] To maximize the visibility of the A_{1g} phonon mode, the measurement is performed in *parallel geometry*.

This result matches the temperature dependence of the high frequency mode observed in Appendix B, confirming that the origin of the doubled peak is purely phononic.

D DFT simulations

In this Appendix we present the results of DFT calculations performed to simulate $RbNiF_3$ vibrational modes. In order to obtain the eigenvalues/eigenvectors of the system, we adopted the *PBEsol approximation*, a generalized-gradient approximation (GGA) which is optimized for periodic systems, i.e. solids [38]. Calculations were performed by Niklas Enderlein and Philipp Hansmann[13].
In Figure D.1 we display the eigenmodes that better match the phonon frequencies and the selection rules (extinction geometry, see Appendix A) of the experiment[14]. Notably, the agreement between the experimental values and the simulations is excellent for the high and low energy phonons while it is slightly off in the case of the $8\,\mathrm{THz}$ mode.
Summarizing, DFT simulations show that:

- Rb atoms are displaced just in the case of the slow modes ($2.67\,\mathrm{THz}$).
- Ni and F atoms are always displaced.

In general, high-frequency modes primarily involve the oscillation of light Fluorine atoms, with Nickel atoms contributing less, and Rubidium atoms the least. Conversely, low-frequency modes feature strong displacements of the heavy Rubidium atoms. These trends can be explained by the differences in atomic masses and their associated inertia. Indeed, heavier atoms like Rubidium have higher inertia due to their larger mass, making them oscillate more slowly and at lower frequencies with respect to Nickel and Fluorine atoms.

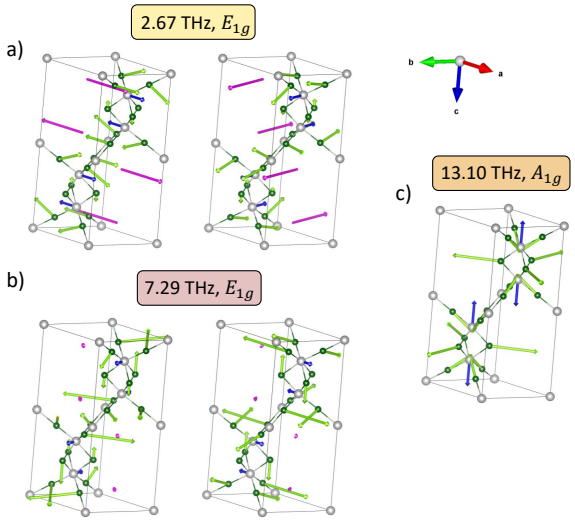

FIGURE D.1: DFT simulations of the 2.9 (a), 8 (b) and $13\,\mathrm{THz}$ (c) coherent phonons detected in Figure 3.13. Vectors indicate the atomic displacements. To improve the visualization, Rb atoms are omitted. Images were generated with VESTA software by N. Enderlein.

[13] *University of Erlangen-Nürnberg*
[14] We point out that in Figure D.1 (a) and (b) simulations return two degenerate modes.

References

[1] W Rudorff, J Kandler, and D Babel. "UNTERSUCHUNGEN AN TERNAREN FLUORIDEN. 1. STRUKTUR, MAGNETISMUS UND REFLEXIONSSPEKTREN VON ALKALI, AMMONIUM UND THALLIUM-NICKEL (II)-FLUORIDEN". In: *ZEITSCHRIFT FUR ANORGANISCHE UND ALLGEMEINE CHEMIE* 317.5-6 (1962), pp. 261–287.

[2] MW Shafer et al. "Magnetic and optical properties of transparent RbNiF3". In: *Applied Physics Letters* 10.7 (1967), pp. 202–204.

[3] G Zanmarchi and PF Bongers. "Magnon sidebands in the optical spectrum of RbNiF3". In: *Solid State Communications* 6.1 (1968), pp. 27–31.

[4] RV Pisarev et al. "Magneto-optical study of the 3A2 to 1Ea transition in magnetic crystals KNiF3, Rb2NiF4d4, K3Ni2F7, RbNiF3". In: *Journal of Physics C: Solid State Physics* 7.22 (1974), p. 4143.

[5] Claudio Giannetti et al. "Ultrafast optical spectroscopy of strongly correlated materials and high-temperature superconductors: a non-equilibrium approach". In: *Advances in Physics* 65.2 (2016), pp. 58–238.

[6] Davide Bossini et al. "Controlling coherent and incoherent spin dynamics by steering the photoinduced energy flow". In: *Physical Review B* 89.6 (2014), p. 060405.

[7] Giovanni Batignani et al. "Probing ultrafast photo-induced dynamics of the exchange energy in a Heisenberg antiferromagnet". In: *Nature Photonics* 9.8 (2015), pp. 506–510.

[8] Davide Bossini et al. "Macrospin dynamics in antiferromagnets triggered by sub-20 femtosecond injection of nanomagnons". In: *Nature communications* 7.1 (2016), p. 10645.

[9] D Bossini et al. "Laser-driven quantum magnonics and terahertz dynamics of the order parameter in antiferromagnets". In: *Physical Review B* 100.2 (2019), p. 024428.

[10] Petr Němec et al. "Antiferromagnetic opto-spintronics". In: *Nature Physics* 14.3 (2018), pp. 229–241.

[11] Alexandre Marciniak et al. "Vibrational coherent control of localized d–d electronic excitation". In: *Nature Physics* 17.3 (2021), pp. 368–373.

[12] Lili Hu et al. "Spin-phonon coupling in two-dimensional magnetic materials". In: *National Science Open* 2.4 (2023), p. 20230002.

[13] JA Kafalas and JM Longo. "Effect of pressure on the structure and magnetic properties of RbNiF3". In: *Materials Research Bulletin* 3.6 (1968), pp. 501–506.

[14] SR Chinn, HJ Zeiger, and JR O'Connor. "Two-Magnon Raman Scattering and Exchange Interactions in Antiferromagnetic KNi F 3 and K 2 Ni F 4 and Ferrimagnetic RbNi F 3". In: *Physical Review B* 3.5 (1971), p. 1709.

[15] Philip W Anderson. "Theory of magnetic exchange interactions: exchange in insulators and semiconductors". In: *Solid state physics*. Vol. 14. Elsevier, 1963, pp. 99–214.

[16] John B Goodenough. "Magnetism and the chemical bond". In: *(No Title)* (1963).

[17] PA Fleury, JM Worlock, and HJ Guggenheim. "Light Scattering from Phonons and Magnons in RbNi F 3". In: *Physical Review* 185.2 (1969), p. 738.

[18] K Knox, RG Shulman, and S Sugano. "Covalency Effects in KNi F 3. II. Optical Studies". In: *Physical Review* 130.2 (1963), p. 512.

[19] J Ferguson, HJ Guggenheim, and DL Wood. "Electronic Absorption Spectrum of Ni II in Cubic Perovskite Fluorides. I". In: *The Journal of Chemical Physics* 40.3 (1964), pp. 822–830.

[20] Yasutaka Suemune and Hyō Ikawa. "Thermal conductivity of KMnF3, KCoF3, KNiF3, and KZnF3 single crystals". In: *Journal of the Physical Society of Japan* 19.9 (1964), pp. 1686–1690.

[21] J Nouet et al. "Determination of TN for KNiF3 through elastic, magneto-optical, and heat capacity measurements". In: *Applied Physics Letters* 21.4 (1972), pp. 161–162.

[22] Nina Mironova-Ulmane et al. "Influence of radiation defects on exciton-magnon interactions in nickel oxide". In: *Optical Materials and Applications*. Vol. 5946. SPIE. 2006, pp. 93–97.

[23] Davide Bossini et al. "Ultrafast amplification and nonlinear magnetoelastic coupling of coherent magnon modes in an antiferromagnet". In: *Physical Review Letters* 127.7 (2021), p. 077202.

[24] Katsuaki Sato and Takayuki Ishibashi. "Fundamentals of magneto-optical spectroscopy". In: *Frontiers in Physics* 10 (2022), p. 946515.

[25] GA Smolensky et al. "Magneto-optical and Nuclear Magnetic Resonance Studies of RbNiF 3". In: *Journal of Applied Physics* 39.2 (1968), pp. 568–570.

[26] Daniele Fausti et al. "Light-induced superconductivity in a stripe-ordered cuprate". In: *science* 331.6014 (2011), pp. 189–191.

[27] A. von Hoegen et al. "Amplification of Superconducting Fluctuations in Driven $YBa_2Cu_3O_{6+x}$". In: *Phys. Rev. X* 12 (3 July 2022), p. 031008. DOI: 10.1103/PhysRevX.12.031008. URL: https://link.aps.org/doi/10.1103/PhysRevX.12.031008.

[28] Sebastian Fava et al. "Magnetic field expulsion in optically driven YBa2Cu3O6. 48". In: *Nature* (2024), pp. 1–6.

[29] Junjie He and Thomas Frauenheim. "Optically driven ultrafast magnetic order transitions in two-dimensional ferrimagnetic MXenes". In: *The Journal of Physical Chemistry Letters* 11.15 (2020), pp. 6219–6226.

[30] Nanshu Liu, Si Zhou, and Jijun Zhao. "Photoinduced spin injection and ferromagnetism in 2D group III monochalcogenides". In: *The Journal of Physical Chemistry Letters* 13.2 (2022), pp. 590–597.

[31] Zhaobo Zhou et al. "Ultralong lifetime for fully photogenerated spin-polarized current in two-dimensional ferromagnetic/nonmagnetic semiconductor heterostructures". In: *Physical Review B* 103.24 (2021), p. 245411.

[32] Yingzhen Tian et al. "Optically driven magnetic phase transition of monolayer RuCl3". In: *Nano Letters* 19.11 (2019), pp. 7673–7680.

[33] Nguyen Phuc Duong, Takuya Satoh, and Manfred Fiebig. "Ultrafast manipulation of antiferromagnetism of NiO". In: *Physical review letters* 93.11 (2004), p. 117402.

[34] Andrea Rubano et al. "Influence of laser pulse shaping on the ultrafast dynamics in antiferromagnetic NiO". In: *Physical Review B* 82.17 (2010), p. 174431.

[35] Emre Ergeçen et al. "Magnetically brightened dark electron-phonon bound states in a van der Waals antiferromagnet". In: *Nature Communications* 13.1 (2022), p. 98.

[36] Emre Ergeçen et al. "Coherent detection of hidden spin–lattice coupling in a van der Waals antiferromagnet". In: *Proceedings of the National Academy of Sciences* 120.12 (2023), e2208968120.

[37] Hans Kuzmany. *Solid-state spectroscopy*. 1998.

[38] John P Perdew, Kieron Burke, and Matthias Ernzerhof. "Generalized gradient approximation made simple". In: *Physical review letters* 77.18 (1996), p. 3865.

Chapter 4

Ultrafast characterization of the electronic excitations in Cuprates

Abstract

The superconducting state of high temperature superconductors is characterized by electronic excitations that, according to their symmetry, are localized in different regions of the first Brillouin zone. Hence, by isolating the aforementioned excitations, it is possible to perform a momentum-resolved investigation and probe anisotropic properties of Cuprates, like the d-wave superconducting gap.
In this Chapter we show how we can account on electronic Raman scattering to isolate the response of B_{1g} and B_{2g} electronic modes with pump-probe birefringence measurements. Moreover, we perform polarimetry measurements to test the selection rules of the modes, unveiling a strong asymmetric response that suggests a possible *symmetry breaking* scenario.
In details, we first introduce the general framework of high temperature superconductivity, with a special focus on the symmetry of the superconducting gap and on the out-of-equilibrium response of unconventional superconductors.
Then, we introduce the formalism of electronic Raman scattering and we derive two models that describe the process in static and dynamic Raman measurements.
Subsequently, we present the results of a dynamic study performed on two different $Bi_2Sr_2CaCu_2O_{8+\delta}$ samples characterized by a different level of doping. We first characterize their birefringence response as a function of the pump fluence and temperature. Later, we perform a complete study of the birefringence signal as a function of the pump and probe polarization, in order to test the selection rules previously derived.
Finally, we discuss the experimental results and propose a possible scenario that explains the anomalous asymmetric response observed.

4.1 High-temperature superconductivity

It was 1911 when H.K.Onnes reported an anomalous drop in the resistivity of Mercury at $4.2\,\mathrm{K}$, opening a new fundamental problem in Physics: *superconductivity*. It took more than 40 years of experimental and theoretical efforts to characterize this phenomenon and fully understand its origin. Indeed, in 1957, Bardeen, Cooper and Schrieffer formulated the first microscopic description of superconductivity in the so-called *BCS theory* [1], where they addressed the superconducting phase to the formation of bounded electronic states (*Cooper pairs*) through electron-lattice interaction. But the story wasn't over yet.

In 1986 Bednorz and Müller discovered that LaBaCuO presented characteristic superconducting properties up to $35\,\mathrm{K}$ [2], a temperature much higher than the ones previously observed. Subsequently, other materials, e.g. BSCCO or YBCO, where found to be superconductors above the boiling point of Nitrogen ($77\,\mathrm{K}$) and the phenomenon of *High Temperature Superconductivity* was validated. This finding was of great relevance for two reasons:

- the potential impact of materials that could sustain superconductivity at high temperatures on technological devices
- the failure of *BCS theory* in describing the highly correlated ground state of these materials

In particular, after almost 40 years, the mediating particle that plays the role of phonons in condensing electron pairs is still unknown and the development of a comprehensive theory for high-temperature superconductivity remains one of the puzzling problems of modern physics.

4.1.1 Cuprate superconductors

Starting from the synthesis of LBCO, the search for room temperature superconductivity has led to the finding of many different families of high temperature superconductors. However, the most studied remains the very first discovered: Cuprates.

Cuprates are a class of ceramic materials with perovskite-like structure. They are characterized by layers of CuO_2 planes intertwined with insulating layers that act as charge reservoirs. In particular, most of the peculiar superconducting properties of cuprates are determined by CuO_2 planes (Figure 4.1).

Cuprates properties heavily depend on a set of parameters, e.g. *temperature*, *pressure* and *doping*[1], giving rise to a rich *phase diagram*. In Figure 4.2 we report a typical phase diagram as a function of hole doping and temperature. We identify different phases:

- In the absence of additional charges, pristine Cuprates are Mott insulators, in contrast with conventional band theory that predicts a metallic behavior (odd number of electrons per *Cu* site). This is due to the strong electron-electron repulsion that forbids the creation of doubly-occupied sites and hence blocks electronic motion at low temperatures [4].
  Importantly, virtual charge fluctuations generate super-exchange interaction involving *Cu-O-Cu* atoms that results in long range antiferromagnetic ordering [5]. The presence of a precursor antiferromagnetic state has stimulated the discussion on the possible role of spin fluctuations in the onset of high-temperature superconductivity [6–8].

[1] i.e. We define *doping* (p) the concentration of carriers (electrons/holes) in the system obtained by the addition/substitution of chemical elements.

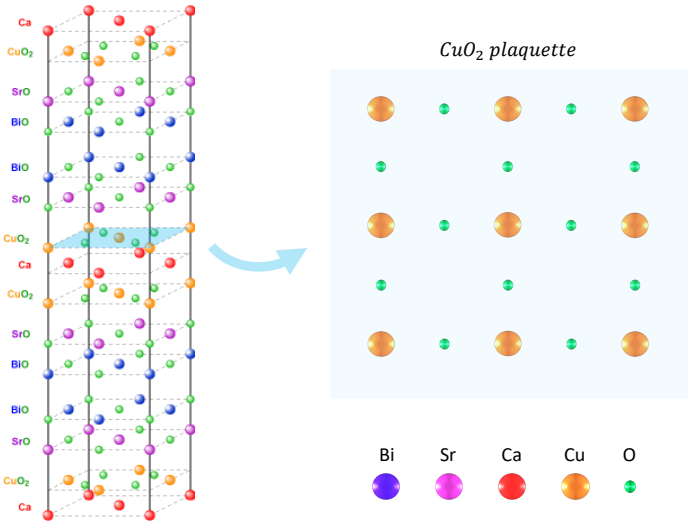

FIGURE 4.1: atomic structure of $Bi_2Sr_2CaCu_2O_{8+\delta}$, a prototypical cuprate superconductor. On the right, the frontal view of the CuO_2 plaquette. Adapted from [3].

- By increasing the hole concentration, the antiferromagnetic phase disappears and at low temperatures we access the superconducting phase (SC: green dome in Figure 4.2). We define the critical temperature (T_c) as the doping dependent temperature below which the system is a superconductor. T_c reaches a maximum in correspondence of the *optimal doping* (OP, $p \sim 0.16$) and diminishes both at lower (*underdoping*, UD) and higher (*overdoping*, OD) concentrations of carriers.
  Importantly, SC phase in Cuprates is characterized by the presence of an anisotropic electronic gap Δ with *d-wave symmetry* (see Section 4.1.2).

- A peculiar phase of Cuprates is the so-called *pseudogap phase* (PG: blue area, Figure 4.2). This phase arises in underdoped and optimally doped samples by increasing the temperature and endures up to $T^*(p)$. Pseudogap presents some characteristic hybrid properties that don't reconnect nor to superconductors neither to metals, like resistivity [9], specific heat [10] and optical conductivity [11]. Remarkably, electron tunneling and ARPES experiments have revealed the presence of an electronic gap also in the pseudogap phase [12–15].
  There is still no unanimous consensus on the interpretation of this exotic phase, whether it is an actual phase in competition with superconductivity or a precursor of the superconducting state that lacks long-range coherence [16, 17].

- Above the SC and PG phase, Cuprates exhibit a metallic behavior that is usually referred to as *normal phase*. In particular, Cuprates behave as *strange metals* above T^* and experience a transition to a *Landau Fermi liquid* in the overdoped regime.
  The study of superconducting properties has diverted attention from the normal phase, but recently this phase has been brought back to the center of discussion by studies on the existence of a quantum critical point [18] and on the occurrence of competing magnetic orders at high levels of doping [19–21] .

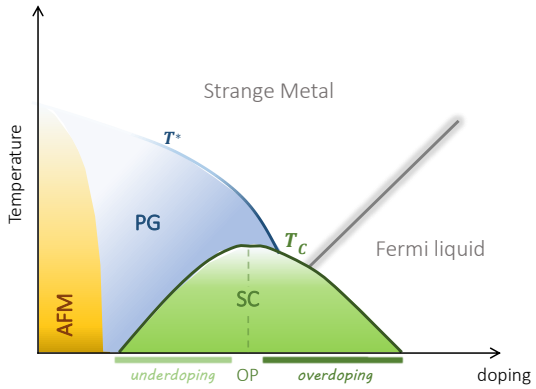

FIGURE 4.2: schematic phase diagram of a hole-doped Cuprate.

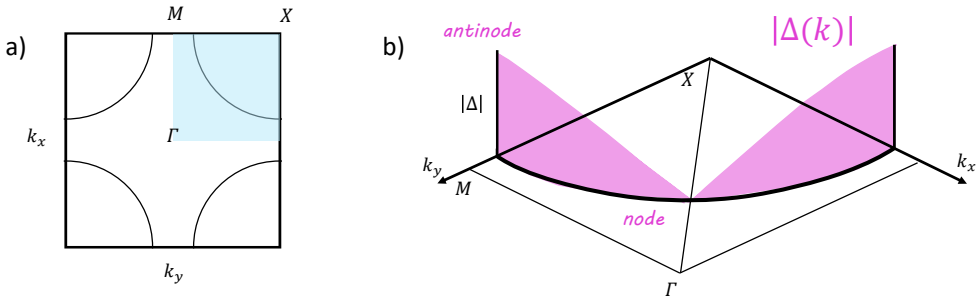

FIGURE 4.3: (a) Energy surface of Cuprates in the first Brillouin zone. (b) sketch of the modulus of the energy gap with d-wave symmetry. Notably, the gap reaches its maximum value $|\Delta|$ along the $\overline{\Gamma M}$ direction (antinodes) and vanishes along $\overline{\Gamma X}$ (nodes).

4.1.2 Superconducting gap

An important difference between Cuprates and conventional BCS superconductors concerns the symmetry of the electronic gap. While the latter exhibits an isotropic gap with *s-wave* symmetry in the momentum space, Cuprates display a strong anisotropic gap with *d-wave symmetry* [22–24]. This means that the amplitude of the energy gap modulates across the Brillouin zone, moving from regions where the gap value is maximum (*antinodes*, $\overline{MX}$ direction) to regions where the gap vanishes (*nodes*, $\overline{\Gamma X}$ direction) and changes sign [25]. We visualize the aforementioned behavior in Figure 4.3.

The direct consequence of the band anisotropy is that the required energy to break a Cooper pair into two quasiparticles changes across the Brillouin zone: while *nodal quasiparticles* are created at all excitation energies, *antinodal quasiparticles* are generated just when the excitation energy exceeds the threshold of the energy gap $|\Delta|$ (Figure 4.3). This results in a thermal population of nodal quasiparticles that even at temperatures close to $0\,\mathrm{K}$ dominates the equilibrium response of Cuprates. In this perspective, out-of-equilibrium studies offer the possibility to measure the non thermal response and address the relaxation dynamics of antinodal quasiparticles [26–28].

4.1.3 Non-equilibrium physics in Cuprates

The non-equilibrium dynamics in superconductors is usually well reproduced by the phenomenological description developed by Rothwarf and Taylor [29]. In their model, when the pump pulse impinges on the sample, it breaks $n/2$ Cooper pairs creating n excited

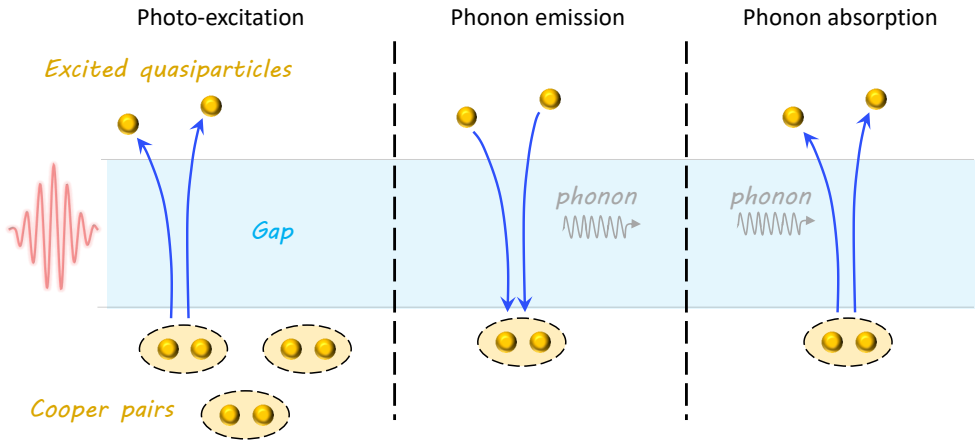

FIGURE 4.4: Rothwarf-Taylor model. When a superconductor is photo-excited by an ultrashort light-pulse, Cooper pairs are broken and excited quasiparticles are created (left). The subsequent recovery dynamic is ruled by the recombination of quasiparticles into Cooper pairs via phonon emission (center) and by phonon absorption, which generates other quasiparticles (right).

quasiparticles. In the presence of *phonon-quasiparticle interaction*, two opposite processes occur:

- excited quasiparticles tend to recombine into Cooper pairs by the emission of phonons with energy $E_{ph} \geq 2\Delta$
- emitted phonons can interact with other Cooper pairs, break them and generate excited quasiparticles

The whole process is sketched in Figure 4.4. Notably, the longer is the phonon lifetime, the higher is the probability of breaking Cooper pairs into quasiparticles, slowing down the recovery dynamics. At the same time, there is a limit to the maximum slowdown of the dynamics that is determined by the balance between the creation of quasiparticles and phonons. This equilibrium is named *phonon bottleneck regime*.

Rothwarf and Taylor framed the process with the following coupled equations:

$$\frac{\partial n}{\partial t} = I_{qp}(t) + \eta p - \beta n^2 \tag{4.1}$$

$$\frac{\partial p}{\partial t} = I_p(t) - \frac{\eta p}{2} + \frac{\beta n^2}{2} - \gamma(p - p_T) \tag{4.2}$$

where n and p represent the number of quasiparticles/phonons in the system, I_{qp}/I_p the number of quasiparticles/phonons injected by the pump pulse, η the transition probability for pair breaking due to phonon absorption , βn the phonon-emission rate and γ accounts for all the other phonon-decay channels. Finally, p_T is the population of phonons in thermal equilibrium at temperature T.

The *bottleneck regime* is described by the condition $\gamma << \eta$, i.e. the most favourable decay channel of phonons is the generation of excited quasiparticles (Figure 4.4, right panel) rather than thermalization.

Rothwarf-Taylor mechanism well describes the non-equilibrium response of Cuprates in the

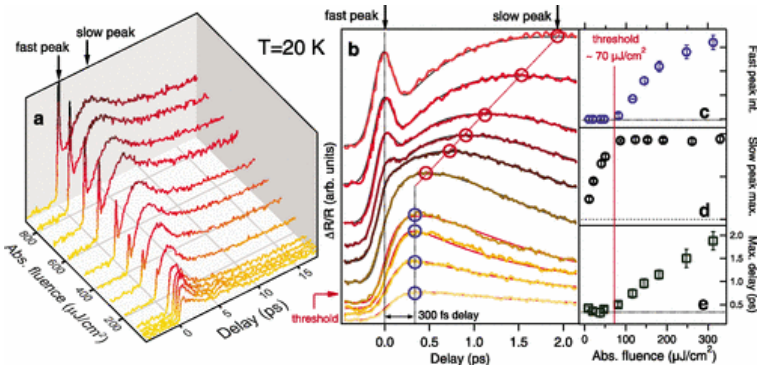

FIGURE 4.5: ultrafast melting of the SC phase. Above a threshold fluence of $70\mu J/cm^2$, transient reflectivity traces display a structured temporal dynamics that the authors [31] address to the ultrafast melting (fast peak) and subsequent recovery of the SC state. From [31].

weak-perturbative regime. Notably, the model reproduces[2] the increase in decay time of the SC signal that occurs when T_c is approached [30].

However, an intriguing picture emerges when the density of excitations is increased. Giannetti et al [31] showed that intense pump pulses can induce a fast quench of the SC state that is subsequently recovered after few *ps* (Figure 4.5). Moreover, other works proved that it is possible to photo-induce a transient melting of the SC state without breaking the Cooper pairs but by destroying the long-range coherence of the condensate [32].

A particularly interesting case is the one of resonant sub-gap optical excitations ($\omega \leq 2\Delta(T)$). In a gapped system, the quasiparticle distribution at equilibrium affects the value of the energy gap [27]. Hence, by modifying the QP distribution, it is possible to enhance the gap value and, reconnecting to superconductors, to obtain superconductivity at temperatures $> T_c$. Importantly, to achieve an increase in the gap value, it is crucial to keep the total number of excitations constant, i.e. photo-excitation must not create additional QPs by destroying Cooper pairs.
Sub-gap excitations are perfectly fit for fulfilling these requirements, since they do not possess enough energy to break Cooper pairs but they can promote thermal quasi particles from $\Delta < E_k < \Delta + \hbar\omega$ states to less populated states at $E_k > \Delta + \hbar\omega$ [27].
This effect was observed on thin metallic films [33] but it is difficult to extend such formalism to the case of unconventional superconductors with anisotropic gaps. Indeed, the presence of nodal regions prevents the condition ($\omega \leq 2\Delta(T,k)$) from being fulfilled at every k value and the creation of QPs is expected where the gap vanishes.

Nonetheless, the experimental efforts towards the achievement of photo-induced superconductivity produced many evidences which indicate that sub-gap pulses[3] can generate a transient SC state also in high temperature superconductors [34–40].
Yet, it isn't clear if the observation of superconductivity above T_c is due to the melting of competing charge orders [34], to a change of the inter-layer distance between CuO planes

[2] Considering that the amplitude of the superconducting gap diminishes by approaching T_c , a higher number of phonons will be able to break Cooper pairs, i.e. η and βn will increase with respect to γ. As a result, a quasi equilibrium between phonons and quasiparticles establishes, slowing down the dynamics of recombination.

[3] Since superconducting gaps are typically of the order of tenths of meV, resonant radiation lies in the mid-Infrared (MIR) spectral range.

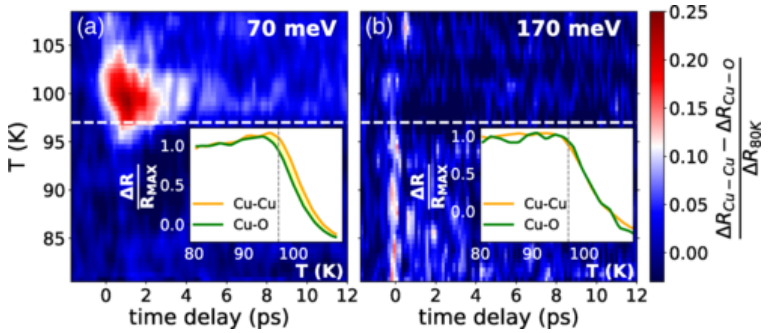

FIGURE 4.6: Photo-induced superconductivity. By measuring the difference between the transient reflectivities due to *Cu-Cu* and *Cu-O* polarized pump, *Giusti and al.* [37] identify a signal above T_c appearing in the resonant condition ($E_{pump} = 70\text{meV} \sim 2\Delta$) that they link to the SC state. From [37].

[41] or to other processes mediated by the action of mid-IR pulses.

Summarizing, while high energy excitations ($> 2\Delta$) can destroy superconductivity by breaking Cooper pairs or shattering phase coherence, resonant pumping ($\sim 2\Delta$) can lead to the onset of a transient SC state also above T_c.

4.2 Electronic Raman Scattering in Cuprates

When light impinges on a material, most of the radiation is elastically scattered out and just a tiny portion experiences inelastic interaction, leaving or absorbing energy from the system. This process, named after C.V Raman who firstly discovered the effect [42], is known as *Raman scattering*.
Commonly associated to phonons, Raman scattering is a general phenomenon that involves elementary excitations in solids, no matter if they originate from lattice, spin or electronic degrees of freedom. Indeed, after the first studies on the breaking of Cooper pairs in BCS superconductors [43], Raman scattering from electronic excitations has been extensively studied for characterizing electron correlated systems.
Notably, by selecting the polarization of the incoming/scattered photons, *Electronic Raman Scattering* allows for the isolation of the electron dynamics in different regions of the Brillouin zone. This is a crucial aspect for the study of high-temperature superconductors, since it permits to measure independently the contributions coming from the nodes/antinodes [44].

In this Section, we provide a full-quantum description description of Raman Scattering, deriving the general expression for the Raman tensor. Then, we discuss the specific case of Cuprates, calculating the first-order tensor elements for the D_{4h} point symmetry group. In conclusion, we propose a full non-equilibrium treatment of electronic excitations by introducing a third-order Raman tensor that accounts for the pump polarization.

4.2.1 Quantum model for Raman Scattering

Raman scattering is a photon-in photon-out process that occurs when light impinges on a target material involving the creation/annihilation of an elementary excitation in it.
The general process can be framed in the following way:

- The incident radiation couples with the electronic system. In particular, photon absorption promotes the system in a virtual intermediate state and creates an electron-hole pair
- The electron-hole pair migrates to another state, determining the creation/annihilation of an elementary excitation
- The recombination of the electron-hole pair causes the emission of the scattered photon

A classical phenomenological description of Raman scattering has been provided by Smekal in [45] in terms of a periodically modulated polarizability. Even if this description qualitatively catches the important features of the process, including selection rules, the effect remains purely quantum mechanical.
For this reason, we limit the discussion to the full quantum treatment of Raman Scattering.

A quantum description of Raman scattering can be obtained through second-order perturbation theory, where the perturbation is given by the vector potential $\hat{A}$ [44].

We can write the Hamiltonian H of a system with N electrons with mass m and charge e interacting with the electromagnetic field as:

$$H = \sum_{i}^{N} \frac{\left[\hat{p}_i + \frac{e}{c}\hat{A}(r_i)\right]^2}{2m} + H_C + H_F \tag{4.3}$$

where $\hat{p}_i$ and r_i are the momentum operator and spatial-temporal coordinates of the i^{th} particle. The last terms, H_C and H_F, represent the Coulomb interaction and the free electromagnetic field Hamiltonian, respectively.
By expanding the kinetic term in equation 4.3, we obtain:

$$\begin{aligned} H &= \tilde{H} + \frac{e}{2mc}\sum_i^N \left[\hat{p}_i\hat{A}(r_i) + \hat{A}(r_i)\hat{p}_i\right]^2 + \frac{e^2}{2mc^2}\sum_i^N \hat{A}(r_i)\hat{A}(r_i) \\ &\equiv \tilde{H} + H'_{INT} + H''_{INT} \end{aligned} \tag{4.4}$$

where we defined

$$\tilde{H} = \frac{1}{2m}\sum_i^N \hat{p_i}^2 + H_C + H_F$$

In Electronic Raman Scattering experiments, we measure the total cross section from all the electrons illuminated by the incident light. We can derive it starting from the *Fermi Golden Rule*, that evaluates the probability of an incoming photon with frequency ω_i and polarization $\boldsymbol{e_i}$ to be scattered within the solid angle $(\Omega, \Omega + d\Omega)$ and with an energy that lies in the range $(\omega_s, \omega_s + d\omega_s)$:

$$\frac{\partial^2\sigma}{\partial\Omega\partial\omega_s} \propto \frac{\omega_s}{\omega_i}\frac{1}{\mathcal{Z}}\sum_{I,F} e^{-\frac{E_I}{k_b t}}|M_{F,I}|^2\delta\big(E_F - E_I - \hbar(\omega_i - \omega_s)\big) \tag{4.5}$$

where k_b is the Boltzmann constant, $\mathcal{Z}$ the partition function[4], I and F mark the initial and final states and $M_{F,I}$ is the matrix element of the effective light-scattering operator up to the second order perturbation-theory.

We point out that in equation 4.5 the Dirac delta guarantees the energy conservation while the matrix element $M_{F,I} = \langle F|H'_{INT} + H''_{INT}|I\rangle$ determines the polarization selection rules.

To evaluate the matrix element $M_{F,I}$ we use second-quantization formalism for the electronic states [46] and obtain:

$$\begin{aligned} M_{F,I} = \boldsymbol{e_i}\cdot\boldsymbol{e_s}\sum_{\alpha,\beta}\rho_{\alpha,\beta}(\boldsymbol{q}_i - \boldsymbol{q}_s)\langle F|c^\dagger_\alpha c_\beta|I\rangle + \frac{1}{m}\sum_\nu\sum_{\alpha,\alpha',\beta,\beta'} p_{\alpha,\alpha'}(\boldsymbol{q}_s)\, p_{\beta,\beta'}(\boldsymbol{q}_i)\times \\ \times\left(\frac{\langle F|c^\dagger_\alpha c_{\alpha'}|\nu\rangle\,\langle\nu|c^\dagger_\beta c_{\beta'}|I\rangle}{E_I - E_\nu + \hbar\omega_i} + \frac{\langle F|c^\dagger_\beta c_{\beta'}|\nu\rangle\,\langle\nu|c^\dagger_\alpha c_{\alpha'}|I\rangle}{E_I - E_\nu - \hbar\omega_s}\right) \end{aligned} \tag{4.6}$$

where c_γ and $c^\dagger_\gamma$ are the annihilation and creation operators of the electronic states, $\rho_{\gamma,\gamma'}(\boldsymbol{q})$ is the matrix element for single-particle density fluctuations and $p_{\gamma,\gamma'}(\boldsymbol{q})$ is the momentum density matrix element [47].

We identify two distinct terms in equation 4.6:

- The first term describes *non resonant Raman scattering*, a process where the impinging photon is absorbed to create an electron-hole pair and is subsequently re-emitted.

[4] $\frac{1}{\mathcal{Z}}\sum_j e^{-\frac{E_j}{k_b t}}$ represents the probability of the system to be in the j^{th} microstate with energy E_j.

- The second term involves an intermediate state, created by the absorption of the incoming photon, that later decays in the final state by emitting the scattered photon.

We notice that resonance condition can occur when the incident/scattered photons match the energy difference between the initial and the intermediate states, resulting in an increase of the second term of equation 4.6 and hence in an enhancement of the Raman cross section.
Notably, the presence of resonances enables the possibility of using Raman scattering to extract information on the electronic structure of the system.

4.2.2 Selection rules for Cuprates

A big simplification in the calculation of equation 4.6 can be done by applying group theory arguments. Indeed, the matrix element $M_{F,I}$ can be generally expressed as:

$$M_{F,I} = \langle F|M|I\rangle \tag{4.7}$$

and the Raman tensor M can be decomposed in the basis functions ϕ_μ of the irreducible point group of the crystal [44]

$$M = \sum_\mu R_\mu \phi_\mu \tag{4.8}$$

We point out that the terms that contribute to the sum in equation 4.8 depend on the specific geometry of the experiment, i.e. on the polarization of the incident and scattered photons.

Most of the Cuprates are described by the D_{4h} symmetry group of the tetragonal lattice. Since they have inversion centers, excited modes can either be even (g, *gerade*) or odd (u, *ungerade*) under inversion operation. In addition, just g modes are *Raman active*[5] and hence the only relevant modes for the Raman tensor will be A_{1g},A_{2g}, B_{1g}, B_{2g} and E_g modes. We can write the Raman matrix elements M for a generic crystal with D_{4h} symmetry as [48]:

$$\begin{aligned} M = \frac{1}{2}\Big[& R_{A_{1g}^{(1)}}(e_i^x e_s^x + e_i^y e_s^y) + R_{A_{1g}^{(2)}}(e_i^z e_s^z) + R_{B_{1g}}(e_i^x e_s^x - e_i^y e_s^y) \\ & + R_{B_{2g}}(e_i^x e_s^y + e_i^y e_s^x) + R_{A_{2g}}(e_i^x e_s^y - e_i^y e_s^x) + R_{E_g^{(1)}}(e_i^x e_s^z + e_i^z e_s^x) \\ & + R_{E_g^{(2)}}(e_i^y e_s^z + e_i^z e_s^y)\Big] \end{aligned} \tag{4.9}$$

where R_μ indicates operators projected in the $\mu-$representation and $e^\alpha_{i/s}$ identifies the polarization of the incoming/scattered photons.
We can explicitly write the different terms of equation 4.9 as:

$$A_{1g}^{(1)} \to \begin{pmatrix} a & & \\ & a & \\ & & \end{pmatrix} \quad A_{1g}^{(2)} \to \begin{pmatrix} & & \\ & & \\ & & b \end{pmatrix} \quad B_{1g} \to \begin{pmatrix} c & & \\ & -c & \\ & & \end{pmatrix} \quad B_{2g} \to \begin{pmatrix} & d & \\ d & & \\ & & \end{pmatrix}$$

$$A_{2g} \to \begin{pmatrix} & d & \\ -d & & \\ & & \end{pmatrix} \quad E_g^{(1)} \to \begin{pmatrix} & & e \\ & & \\ e & & \end{pmatrix} \quad E_g^{(2)} \to \begin{pmatrix} & & e \\ & & \\ e & & \end{pmatrix}$$

[5] On the contrary, u modes are *IR-active*.

By properly selecting the polarization of the incoming/scattered photons, we can access the specific projections of the Raman tensor.
However, some projections are characterized by the presence of multiple modes (e.g. $e_i^x e_s^x$ projection measures both A_{1g} and B_{1g} modes). Therefore, the complete isolation of the excited modes often requires experimental geometries that go beyond the detection of the main polarization channel [38].

We now discuss a specific experimental configuration, i.e. when light propagates along the $\hat{c}$ axis of the Cuprate superconductor and hence impinges perpendicularly to the CuO_2 plaquette[6] (Figure 4.1).
With this geometry, Raman tensor becomes:

$$M = \frac{1}{2}\begin{bmatrix} R_{A_{1g}} + R_{B_{1g}} & R_{B_{2g}} \\ R_{B_{2g}} & R_{A_{1g}} - R_{B_{1g}} \end{bmatrix} \tag{4.10}$$

Remarkably, we omitted $R_{A_{2g}}$ from equation 4.10 because A_{2g} mode becomes relevant just in the case of photons with circular polarization [44].

Before moving to the actual computation of $M_{F,I}$ with respect to the incoming/scattered photon polarization, we highlight one of the most important features of electronic Raman scattering, i.e. the ability to focus on the electron dynamics of different regions of the Brillouin zone.
We write the representative basis functions $\phi_\mu(\boldsymbol{k})$ taken from the complete set of Brillouin-zone harmonics for the D_{4h} space group [44, 49] for the three relevant Raman modes:

$$\begin{aligned} A_{1g} &\rightarrow \frac{1}{2}\Big[cos\big(k_x a\big) + cos\big(k_y a\big)\Big] \\ B_{1g} &\rightarrow \frac{1}{2}\Big[cos\big(k_x a\big) - cos\big(k_y a\big)\Big] \\ B_{2g} &\rightarrow sin\big(k_x a\big) \cdot sin\big(k_y a\big) \end{aligned} \tag{4.11}$$

Then, we plot the momentum-dispersion described in equation 4.11 for each of the Raman modes (Figure 4.7). We notice that Raman scattering is sensitive to different regions of the Brillouin zone. In particular, while the A_{1g} mode is total-symmetric, B_{1g} and B_{2g} excitations are strongly anisotropic in the momentum-space: B_{1g} mode maps charge excitations along $\overline{\Gamma M}$ and B_{2g} mode is maximum along $\overline{\Gamma X}$.
Reconnecting to the anisotropy of the superconducting gap (Figure 4.3), B_{1g} mode probes electronic excitations at the antinodes and B_{2g} mode at the nodes.

4.2.3 First order model

There are two possible ways to model Raman scattering in a pump probe experiment. The first option is to neglect the action of the pump and adopt a *static* approach, considering only the interaction of the probe pulse with the system. We refer to this methodology as *First order model* .
The alternative is to provide a comprehensive description of the four-wave mixing process that accounts for both the pump and the probe polarization. Since this method involves the third-order susceptibility tensor, we name it *Third order model*.
We start describing the First order model, that is the one commonly employed in literature

[6] This is the configuration we adopt in the experiments presented in 4.3.

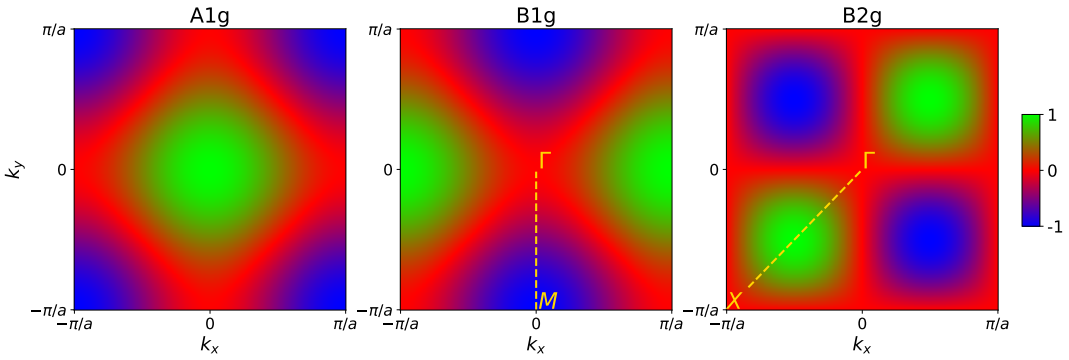

FIGURE 4.7: Momentum-dispersion of Raman active modes, While A_{1g} mode is isotropic, B_{1g} and B_{2g} are strongly anisotropic. In particular, B_{1g} mode is maximum at the antinodes ($\overline{\Gamma M}$) and B_{2g} mode at the nodes ($\overline{\Gamma X}$).

[38, 50].

In the *First order model* there are three important elements to consider:

- the Raman tensor of the system (equation 4.10)
- the Jones vector of the incoming probe light
- the Jones vector of the scattered probe light

Limiting the discussion to linearly polarized beams[7], we write the Jones vector of the incoming/scattered light as:

$$|I\rangle = \begin{pmatrix} cos\theta \\ sin\theta \end{pmatrix} \qquad |F\rangle = \begin{pmatrix} cos\alpha \\ sin\alpha \end{pmatrix} \tag{4.12}$$

where θ and α are referred to the CuO axis. Then, we use them to compute:

$$\begin{aligned} M_{F,I} = \langle F|M|I\rangle &= \begin{pmatrix} cos\alpha, & sin\alpha \end{pmatrix} \begin{pmatrix} a+c & d \\ d & a-c \end{pmatrix} \begin{pmatrix} cos\theta \\ sin\theta \end{pmatrix} \\ &= A_{1g}cos(\theta-\alpha) + B_{1g}cos(\theta+\alpha) + B_{2g}sin(\theta+\alpha) \end{aligned} \tag{4.13}$$

Since θ and α are tunable parameters in the experiment[8], we can properly change them to select specific Raman modes. Among the different configurations that allow for the isolation of the excited modes, we discuss the one that is used for the so-called *birefringence measurements* (a detailed discussion on *extinction geometry* can be found in [46]).

In Birefringence measurements, two orthogonal projections of the probe pulse are measured and subtracted to account for changes in the probe polarization. Connecting to equation 4.16, we describe the transient signal[9] of a birefringence measurement by calculating the contributions $\Delta R^{+/-}$ for the two projections $\alpha = \theta \pm 45°$

$$\Delta R^{+/-} \propto A_{1g}cos(\mp 45°) + B_{1g}cos(2\theta \pm \alpha) + B_{2g}sin(2\theta \pm \alpha)$$

[7] We recall that we already excluded from the discussion circularly polarized light when we derived expression 4.10.

[8] We can control the polarization of the incoming beam θ with a polarizer+halfwave plate and we can select the polarization of the scattered radiation α by placing an analyzer after the sample.

[9] In the main text we discuss a transient reflectivity signal ΔR, but analogous statements can be done for transmission mearurements.

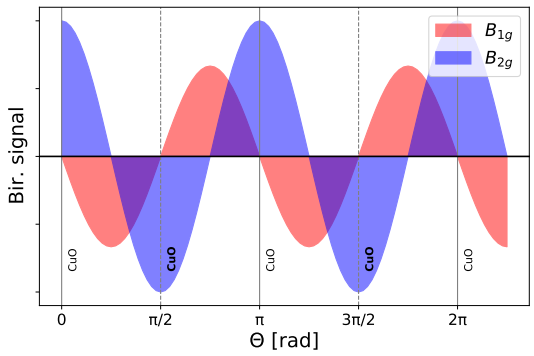

FIGURE 4.8: First order model. Predictions of the birefringence signal as a function of the probe polarization angle. Continuous and dashed vertical lines mark the two CuO axis in the CuO_2 plaquette.

and by subtracting them

$$\Delta\Delta R = \Delta R^{+} - \Delta R^{-} \propto -B_{1g}sin(2\theta) + B_{2g}cos(2\theta) \tag{4.14}$$

Equation4.14 shows that birefringence measurements are not sensitive to the total-symmetric A_{1g} mode, but only to the B_{1g} and B_{2g} ones. Moreover, B_{1g} mode is observed when the probe polarization is parallel to the $CuCu$ direction ($\theta = 45°$) whereas B_{2g} mode is detected when the probe is aligned to the CuO axis ($\theta = 0/90°$). The behavior described by equation4.14 is plotted in Figure 4.8.
In summary, First order model predicts signal for all probe polarization angles: for $k\pi/2$ angles, the signal is completely determined by the B_{2g} excitation while at $\pi/4 + k\pi/2$ the signal is ruled by the B_{1g} mode.

4.2.4 Third order model for non-equilibrium experiments

The main limitation of the First order model consists in ignoring completely the action of the pump, that instead has a crucial role in pump-probe experiments. This oversimplification reduces the capabilities of the model which, for example, fails in describing anisotropic responses reported in [37, 38, 51]. In the tentative to provide a comprehensive description of Raman scattering, we introduce a *Third order model* that accounts also for the pump polarization.

From a theoretical point of view, pump-probe process can be modelled by expanding the interacting Hamiltonian in Equation 4.4. This leads to the formulation of a 4^{th} rank Raman tensor

$$R^{(3)}_{ijkl} = R^{ij}_{A_{1g}} R^{kl}_{A_{1g}} + R^{ij}_{B_{1g}} R^{kl}_{B_{1g}} + R^{ij}_{B_{2g}} R^{kl}_{B_{2g}}$$

with i, j, k, l running on the two indices representing the axis of the CuO_2 plaquette [52]. In this way, the expression of equation 4.10 becomes:

$$R^{(3)}_{ijkl} = \begin{pmatrix} \begin{pmatrix} a^2+c^2 & \\ & a^2-c^2 \end{pmatrix} & \begin{pmatrix} & d^2 \\ d^2 & \end{pmatrix} \\ \begin{pmatrix} & d^2 \\ d^2 & \end{pmatrix} & \begin{pmatrix} a^2-c^2 & \\ & a^2+c^2 \end{pmatrix} \end{pmatrix}$$

where the first two indices are linked to the pump polarization and the last two belong to the polarization of the incoming and the scattered probe. In other words, we model the process as a *four-wave mixing* process, where two pump photons and one probe photon

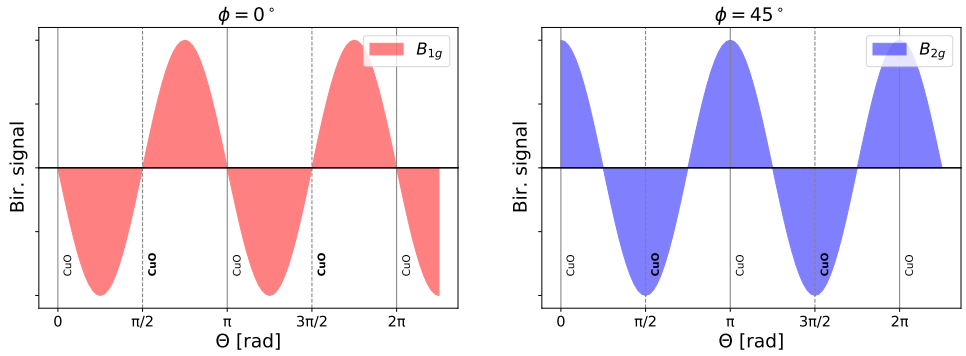

FIGURE 4.9: Third order model. Two scenarios emerge when pump polarization is taken into account: B_{1g} dominates the birefringence response when $\hat{e}_{pump}//CuO$ ($\phi = 0°$, left), while B_{2g} mode is isolated when $\hat{e}_{pump}//CuCu$ ($\phi = 45°$, right).

interact via the third order susceptibility tensor to generate the emitted field.

We now consider the action of a pump pulse with linear polarization. By defining the pump polarization angle ϕ with respect to the CuO sample axis

$$|\phi\rangle = \begin{pmatrix} cos\phi & 0 \\ 0 & cos\phi \\ sin\phi & 0 \\ 0 & sin\phi \end{pmatrix}$$

we compute:

$$\langle\phi|R|\phi\rangle = \begin{pmatrix} a^2 + c^2 cos(2\phi) & d^2 sin(2\phi) \\ d^2 sin(2\phi) & a^2 + c^2 cos(2\phi) \end{pmatrix}$$

In analogy with the calculation in 4.2.3, we include the incoming $\begin{pmatrix} cos\theta \\ sin\theta \end{pmatrix}$ and scattered polarization $\begin{pmatrix} cos\alpha \\ sin\alpha \end{pmatrix}$ as $\langle\alpha|R|\theta\rangle$ and obtain:

$$\Delta R(\theta, \alpha) \propto A_{1g} cos(\theta - \alpha) + B_{1g} cos(\theta + \alpha) cos(2\phi) + B_{2g} sin(\theta + \alpha) sin(2\phi)$$

By subtracting the two orthogonal components with $\alpha = \theta \pm 45°$, we describe the polarization dependence of the birefringence signal:

$$\begin{aligned} \Delta\Delta R &= \Delta R(\alpha = \theta + 45°) - \Delta R(\alpha = \theta - 45°) \\ &\propto -B_{1g} sin(2\theta) cos(2\phi) + B_{2g} cos(2\theta) sin(2\phi) \end{aligned} \tag{4.15}$$

In analogy with equation 4.14, also the Third order model predicts no contribution from the A_{1g} mode to the birefringence signal. However, there are important differences concerning B_{1g} and B_{2g} modes:

- B_{1g} mode is isolated just when the pump polarization $\hat{e}_{pump}$ is parallel to the CuO axis ($\phi = 0°/90°$) and the probe polarization is aligned with the $CuCu$ axis
- oppositely, B_{2g} mode is measured when $\hat{e}_{pump}$ is parallel to the $CuCu$ axis ($\phi = 45°$) and the probe polarization is aligned with the CuO axis

Notably, the inclusion of the pump polarization describes a different scenario with respect to the First order model one. Indeed, the First order model predicts a signal at all probe polarization angles that alternatively originates in the B_{1g} or B_{2g} mode, depending on the orientation of the probe with respect to the sample axis. On the contrary, Third order predicts null signals when $\hat{e}_{pump} \parallel \hat{e}_{probe}$ or $\hat{e}_{pump} \perp \hat{e}_{probe}$ and measures a birefringence signal just when $\theta = \phi + 45^{\circ} + k\pi/2$.

4.3 Dynamic birefringence measurements of the B_{1g} and B_{2g} electronic modes

In order to test the models described in the previous Section, we arrange a pump-probe experiment in reflection geometry on $Bi_2Sr_2CaCu_2O_{8+\delta}$ (BSCCO or Bi-2212), a cuprate superconductor (see structure in Figure 4.1). In details, we test two samples characterized by a different doping level: an underdoped sample (UD, $T_c = 80\,\mathrm{K}$) and an optimally doped sample (OP, $T_c = 90\,\mathrm{K}$).
Starting from the optical setup described in Section 2.2, we employ the MIR beam (tuned at 10 or $17\,\mu\mathrm{m}$) to pump the sample above/on resonance with the superconducting gap and the visible beam, tuned at $750\,\mathrm{nm}$ $(1.65\,\mathrm{eV})$, to probe the excited sample.
In particular, we're interested in performing birefringence measurements to conveniently isolate the B_{1g} and B_{2g} electronic modes [38]. Therefore, we insert on the probe optical path a pair of half-wave plates, one before and one after the sample, to control the orientation of the incoming and outcoming polarization. Then, we place a polarizing beam splitter (PBS) after the second half-wave plate to divide the $\pm 45°$ projections of the scattered probe that are finally measured by two identical NMOS detectors.
The setup is sketched in Figure 4.10.

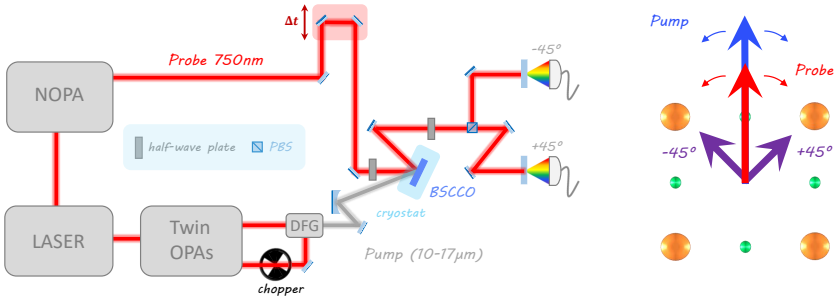

FIGURE 4.10: Setup for the birefringence measurements on BSCCO. The combined action of half-wave plates and piezoelectric rotator provides a full tunability of the orientation of pump/probe polarization with respect to the sample axis.

We recall equations 4.14 and 4.15 to highlight that the birefringence signal is obtained by subtracting the $\pm 45°$ projections.
Since the Third order model predicts changes in the birefringence signal determined by the pump polarization (equation 4.15), we mount the sample on a piezoelectric rotator to properly align the sample axis with the fixed vertical polarization of the MIR pump.

Summarizing, we exploit the optical setup of Figure 4.10 to study two BSCCO samples with a different level of doping. The setup is suited for a full characterization of the birefringence signal, following its dependence on the pump/probe polarization and on the pump energy.

Birefringence signal

In order to measure the dynamic birefringence signal in BSCCO, we measure independently the transient reflectivity maps $\Delta R/R$ of the $\pm 45°$ projections of the probe (*Channel 0* and *Channel 1* plots in Figure 4.11) as a function of the probe energy (y-axis) and pump-probe delay (x-axis). Then, we subtract the two maps to obtain a *birefringence map* $\Delta\Delta R/R$

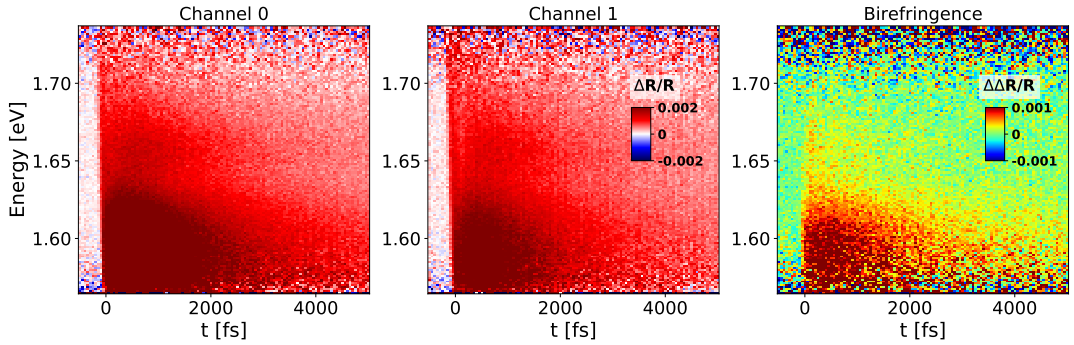

FIGURE 4.11: Example of B_{2g} signal (T=45K) in UD BSCCO sample ($T_c = 80K$). We reconstruct the birefringence signal (right) by measuring the projections of the probe pulse at $+45°$ (left, *Channel 0*) and at $-45°$ (center, *Channel 1*) and subtracting the two dynamic maps.

(right map in Figure 4.11).
Before presenting a full description of the doping/pump-energy/polarization dependence of the birefringence signal, we discuss some general properties of the B_{1g} and B_{2g} signals that we derive from a preliminary fluence study.

4.3.1 Fluence study

To properly isolate the B_{2g} mode, we cool down the UD sample below T_c (T=$55\,\mathrm{K}$) and we set $\hat{e}_{pump} \parallel CuCu$ and $\hat{e}_{probe} \parallel CuO$, since it is the configuration in which both the First and the Third order model predict a birefringence signal (see eq. 4.14 and 4.15). By varying the fluence of the $17\,\mu\mathrm{m}$ Pump, we obtain the maps presented in Figure 4.12.
We unveil a different behavior of the high and low probe energies:

- A birefringence signal is present at all pump fluences in the region around $1.60\,\mathrm{eV}$. The temporal cuts integrated in the 1.58-$1.63\,\mathrm{eV}$ energy range (Figure 4.12, bottom-left) show that a fast response+slow recovery dynamics emerge by increasing the pump fluence ($\phi_{pump} > 480\,\mu\mathrm{J\,cm^{-2}}$). This observation is commonly associated to the ultrafast melting of the superconducting phase that is then recovered on the *ps* timescales[10] [31].

- The high energy region of the probe spectrum is characterized by a fluence dependent signal that is not present in the weak perturbative regime (Figure 4.12, bottom-right).

By rotating the sample by $45°$, hence ending up with $\hat{e}_{pump} \parallel CuO$ and $\hat{e}_{probe} \parallel CuCu$, we isolate the B_{1g} mode that we study with different pump fluences (Figure 4.13).
Also in this case, we observe a different behavior between high and low energies of the probe spectrum, where high energies (Figure 4.13, bottom-right) dynamics emerge just at high pump fluences, while at low energies (Figure 4.13, bottom-left) a birefringence signal is always present.
The main difference between the B_{1g} and B_{2g} geometries concerns the signal localized at low energies. Indeed, while the birefringence signal of the B_{2g} mode is always positive, the one associated to the B_{1g} mode experiences a sign flip on short timescales. A similar

[10] Notably, the onset of the fast response occurs above the threshold $\phi_{pump} = 480\,\mu\mathrm{J\,cm^{-2}}$, that is higher than the one reported in [31] ($\phi_{th} = 70\,\mu\mathrm{J\,cm^{-2}}$) . We address this difference to an overestimation of the average power of the MIR beam that impinges on the sample.

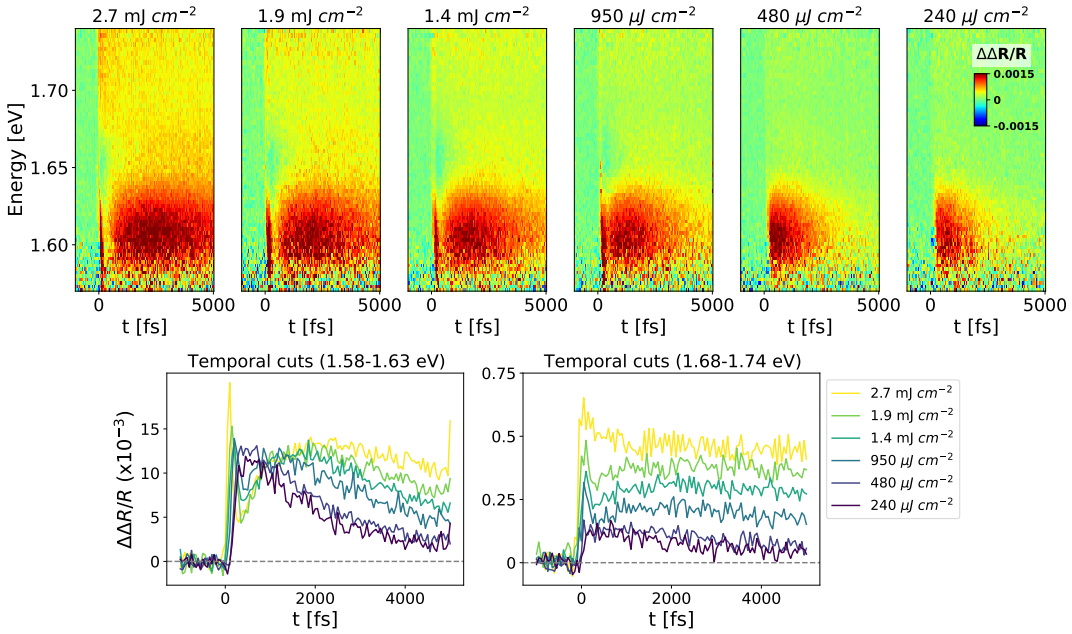

FIGURE 4.12: Fluence dependence of the B_{2g} mode at low temperatures (T=55 K) in UD sample. By properly aligning the pump and the probe polarization ($\hat{e}_{pump} \parallel CuCu$, $\hat{e}_{probe} \parallel CuO$), we isolate the B_{2g} mode. We identify a different relaxation dynamics at low (bottom-left) and high (bottom-right) probe energies.

observation was previously reported by *Giusti et al.* in [38], but with an opposite behavior (i.e. B_{1g} mode was always positive and B_{2g} mode showed an ultrafast negative peak). However, we highlight that the sample studied in [38] is an optimally doped Y-Bi2212 sample ($Bi_2Sr_2Y_{0.08}Ca_{0.92}Cu_2O_{\delta+8}$) and hence we attribute the discrepancy between the two experimental observations to the different chemical composition of the samples.

4.3.2 Temperature dependence

We proceed with our analysis by characterizing the temperature dependence of the birefringence signal. From previous studies [38, 47], we know that the superconducting-to-pseudogap phase transition is marked by a sign change of the birefringence signal associated to the B_{2g} mode. Therefore, we limit our discussion to the B_{2g} geometry for both the UD and the OP samples.

Since the major contribution to the birefringence signal comes from the low energy side of the probe spectrum (Figure 4.12 and 4.13), we display the temperature dependence of the birefringence traces integrated in the 1.58-$1.61\,\mathrm{eV}$ energy range for the UD (Figure 4.14) and the OP samples (Figure 4.15).

In both samples, the dynamic signal of the PG phase is characterized by a fast negative peak that disappears after $\sim 500\,\mathrm{fs}$ (see central panels in Figure 4.14 and 4.15). This is confirmed by looking at the time integrated traces as a function of temperature (right panels in Figure 4.14 and 4.15): negative signal appears in the PG when integrating on the temporal window 0-$500\,\mathrm{fs}$ and washes out when integrating on longer timescales (0-$2\,\mathrm{ps}$). Notably, the sign change that we link to the phase transition occurs approximately $10\,\mathrm{K}$ below the nominal transition temperature for both samples. We attribute this evidence to the thermal heating generated by the pump pulse.

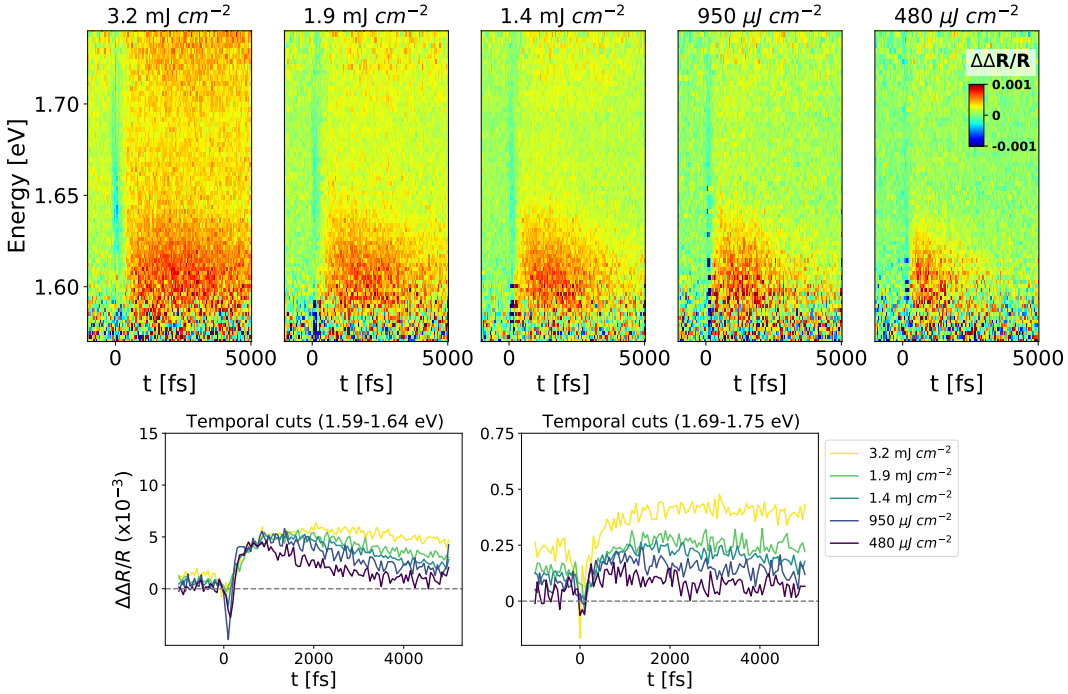

FIGURE 4.13: Fluence dependence of the B_{1g} mode at low temperatures (T=55 K) in UD sample. We isolate the B_{1g} mode by setting $\hat{e}_{pump} \parallel CuO$ and $\hat{e}_{probe} \parallel CuCu$) . In analogy with B_{2g} mode, we identify a different relaxation dynamics at low (bottom-left) and high (bottom-right) probe energies.

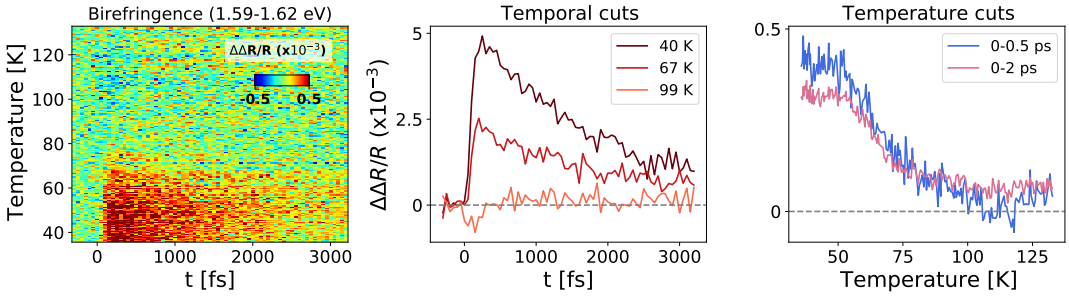

FIGURE 4.14: Temperature dependence of the B_{2g} birefringence signal in the UD sample ($T_c = 80$ K).

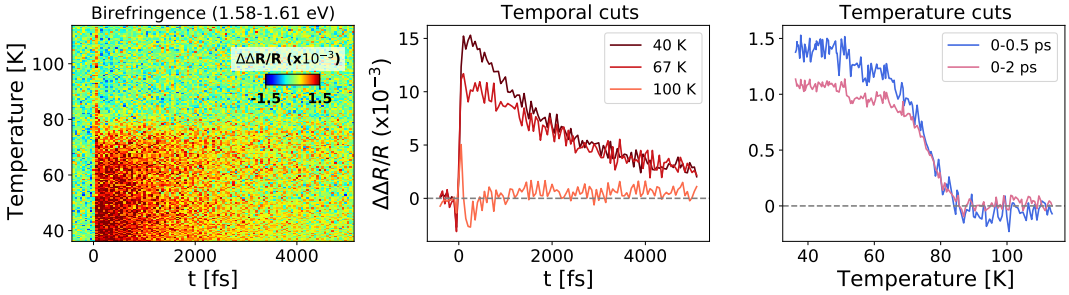

FIGURE 4.15: Temperature dependence of the B_{2g} birefringence signal in the OP sample ($T_c = 90$ K).

4.3.3 Polarimetry measurements

In this section we characterize the birefringence signal associated to the superconducting phase in order to test the selection rules previoulsy derived (equation 4.14 and 4.15). In particular, we study the birefringence signal as a function of the pump energy, pump and probe polarization on two BSCCO samples with a different doping level.
Notably, all the measurements are performed in the low-fluence regime ($480\,\mu\mathrm{J\,cm^{-2}}$), where the superconducting signal is localized around $1.60\,\mathrm{eV}$ (see Figure 4.12 and 4.13) and at temperatures well below T_c (T=$45\,\mathrm{K}$).

Pump ∥ CuCu

We start our investigation by aligning the pump polarization with the CuCu axis of the sample. We recall that with this geometry, according to the *Third order* model, we isolate just the B_{2g} mode and measure it when the probe polarization is set parallel to the CuO axis.

Pump energy $17\,\mu\mathrm{m}$

In Figure 4.16 we report the birefringence maps obtained with a pump energy of $17\,\mu\mathrm{m}$ ($\sim 70\,\mathrm{meV}$) on the UD sample (T_c =$80\,\mathrm{K}$) for different orientations of the probe polarization. In particular, we indicate with θ the angle of the probe polarization with respect to the CuO axis of the sample[11].
We clearly unveil a birefringence signal when $\theta = 0, \pi/2$, i.e. when the probe is polarized along the CuO axis.
Since the signal is localized at low energies, we integrate the dynamic response in the 1.58-$1.615\,\mathrm{eV}$ range and we display the integrated temporal cuts of the four maps (Figure 4.16, bottom-left). Notably, besides the two long-living signals measured when $\hat{e}_{probe} \parallel CuO$ (purple and blue traces), we unveil a fast-decaying signal when the pump is polarized along one of the two CuCu axis (red trace).
Since we expect B_{1g} and B_{2g} signals to live for few ps, we integrate the temporal traces in the 0-$2\,\mathrm{ps}$ time window and we display the obtained values as a function of θ (Figure 4.16, bottom-right). We compare the energy and time integrated values of the birefringence maps with the ones obtained in the normal phase (green dots in Figure 4.16, bottom-right), where the dynamic response is dominated by an ultrafast signal (see Appendix A). In this way, we address to the superconducting state all the features greater than the NP ones (i.e., all values out of the green area in Figure 4.16).
We conclude that superconducting signals are unambiguously measured at $\theta = 0, \pi/2$, while the fast signal detected at $\theta = \pi/4$ may have a different origin.

The scenario changes when we study the OP sample with the same pump energy ($E_{pump} = 17\,\mu\mathrm{m}$) and orientation ($\hat{e}_{pump} \parallel CuCu$). Results are presented in Figure 4.17. All birefringence maps show more intense signals with respect to the ones measured on the UD sample (Figure 4.16). This can be explained by a difference in the actual pump spot size on the sample that results in a higher fluence for the OP sample.

The temporal cuts integrated in the 1.58-$1.615\,\mathrm{eV}$ energy range (Figure 4.16, bottom-left) show a long living signal when the probe is parallel to the CuO axis ($\theta = 0, \pi/2$) and when its polarized along one of the two CuCu axis ($\theta = \pi/4$, red trace). On the contrary, a fast signal is measured at $\theta = 3\pi/4$ (orange trace).

[11] i.e. $\theta = k\pi/2$ corresponds to $\hat{e}_{probe} \parallel CuO$ while $\theta = \pi/4 + k\pi/2$ to $\hat{e}_{probe} \parallel CuCu$.

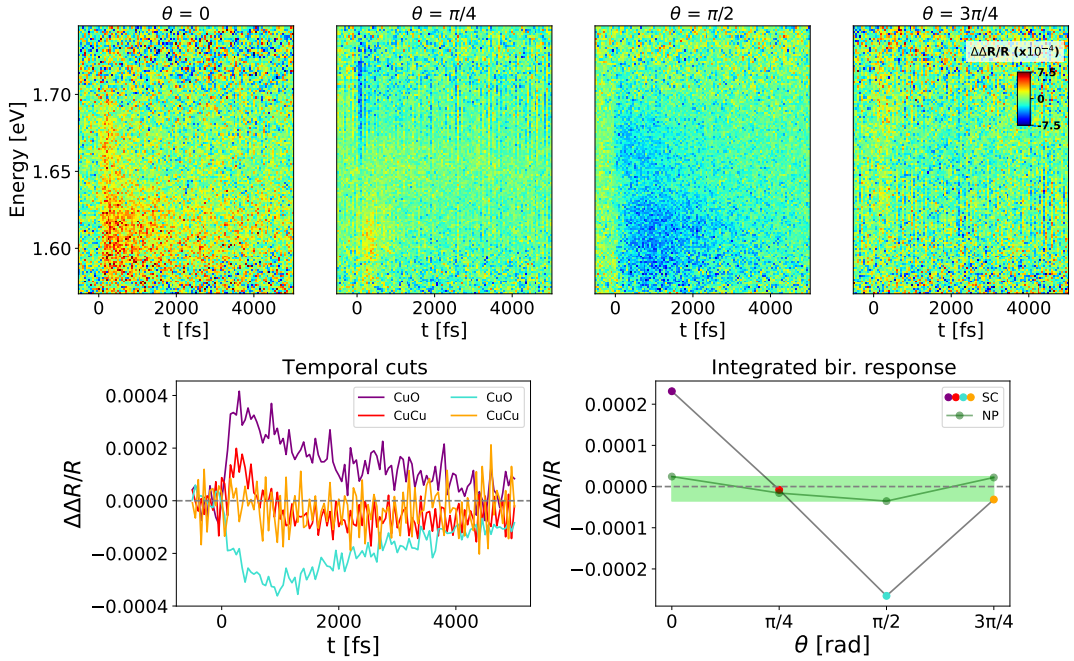

FIGURE 4.16: birefringence maps obtained on the UD sample with $E_{pump} = 17\,\mu\mathrm{m}$ and $\hat{e}_{pump} \parallel CuCu$. On the bottom row, we display the energy-integrated (1.58-1.615 eV) cuts and the energy and time integrated (1.58-1.615 eV, 0-2 ps) values as a function of the probe polarization angle θ.

We postpone the complete discussion on the electronic modes after the presentation of the data with the $10\,\mu\mathrm{m}$ pump. We just report that, by looking at the energy and time integrated plots (Figure 4.17, bottom-right), we can link the signals measured at $\theta = 0, \pi/2$ and $\theta = \pi/4$ to the superconducting state, while the origin of the fast signal at $\theta = 3\pi/4$ (orange) is not clear.

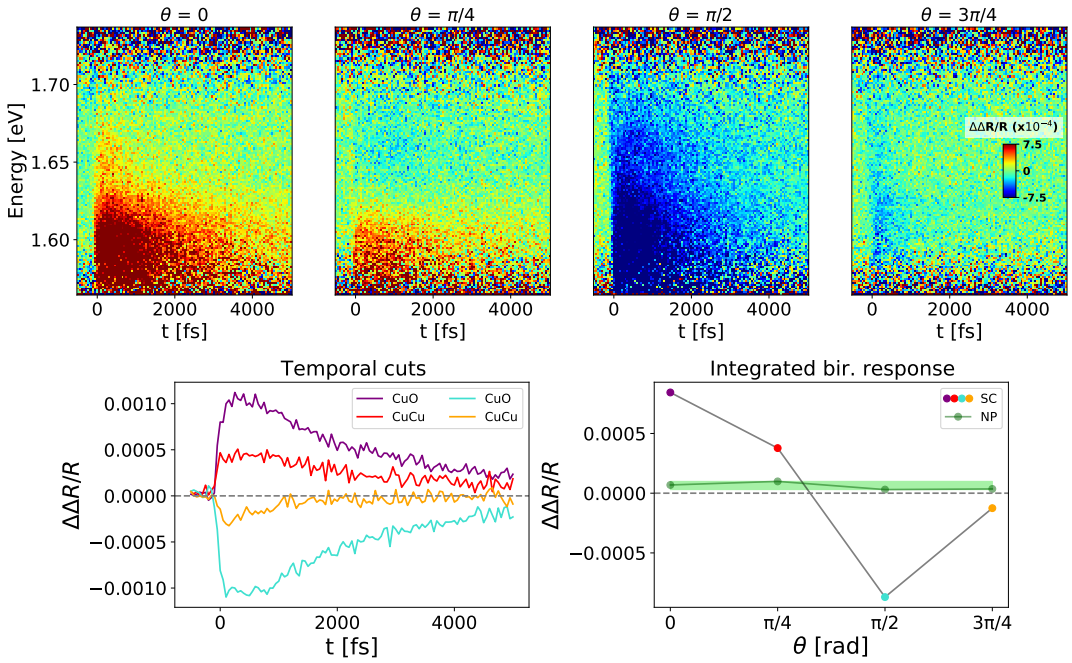

FIGURE 4.17: birefringence maps obtained on the OP sample with $E_{pump} = 17\,\mu\mathrm{m}$ and $\hat{e}_{pump} \parallel CuCu$. On the bottom row, we display the energy-integrated (1.58-1.615 eV) cuts and the energy and time integrated (1.58-1.615 eV, 0-2 ps) values as a function of the probe polarization angle θ.

Pump energy $10\,\mu m$

We now present the results obtained with the high energy pump ($E_{pump} = 10\,\mu m$) with $\hat{e}_{pump} \parallel CuCu$.
In Figure 4.18 we show the results obtained on the UD sample. The main differences with respect to the measurements performed with the $17\,\mu m$ pump (Figure 4.16) concern the birefringence signal at $\theta = \pi/4, 3\pi/4$, i.e. when the probe is aligned with the CuCu axis. In details, the fast signal at $\theta = \pi/4$ (red trace) has a maximum intensity equal to the signal at $\theta = 0$ (purple trace) and hence is considerably enhanced with respect to the $17\,\mu m$ measurement. Moreover, we measure a fast positive signal also at $\theta = 3\pi/4$ (orange trace), while we didn't measure any with the low energy pump (see Figure 4.16, bottom-left panel, orange trace).

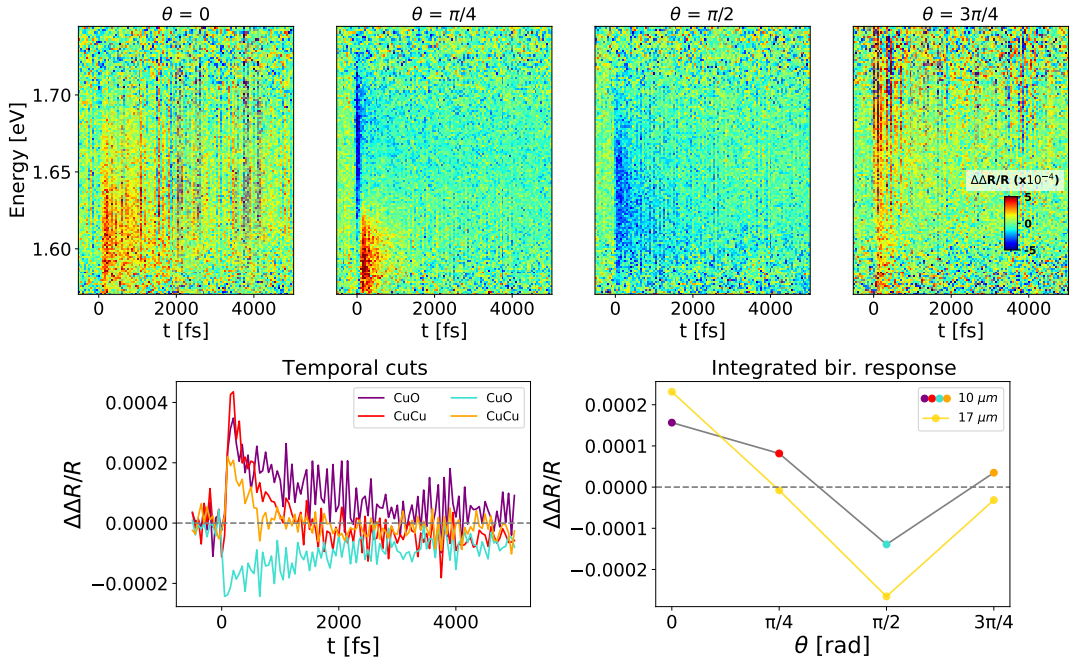

FIGURE 4.18: birefringence maps obtained on the UD sample with $E_{pump} = 10\,\mu m$ and $\hat{e}_{pump} \parallel CuCu$. Temporal cuts (bottom-left) and angle dependence plots (bottom-right) are obtained by integrating the signal on the same intervals of Figure 4.16.

Finally, we present the birefringence maps obtained on the OP sample with the $10\,\mu m$ pump (Figure 4.19).
In analogy with the results on the UD sample, the main differences that occur by changing the pump energy concern the maps obtained when the probe polarization is aligned with the CuCu axis. In particular, we observe a symmetric fast signal at $\theta = \pi/4, 3\pi/4$ (red and orange traces in Figure 4.19, bottom-left) while we unveiled a strong asymmetric response in the case of the $17\,\mu m$ pump (see Figure 4.17).

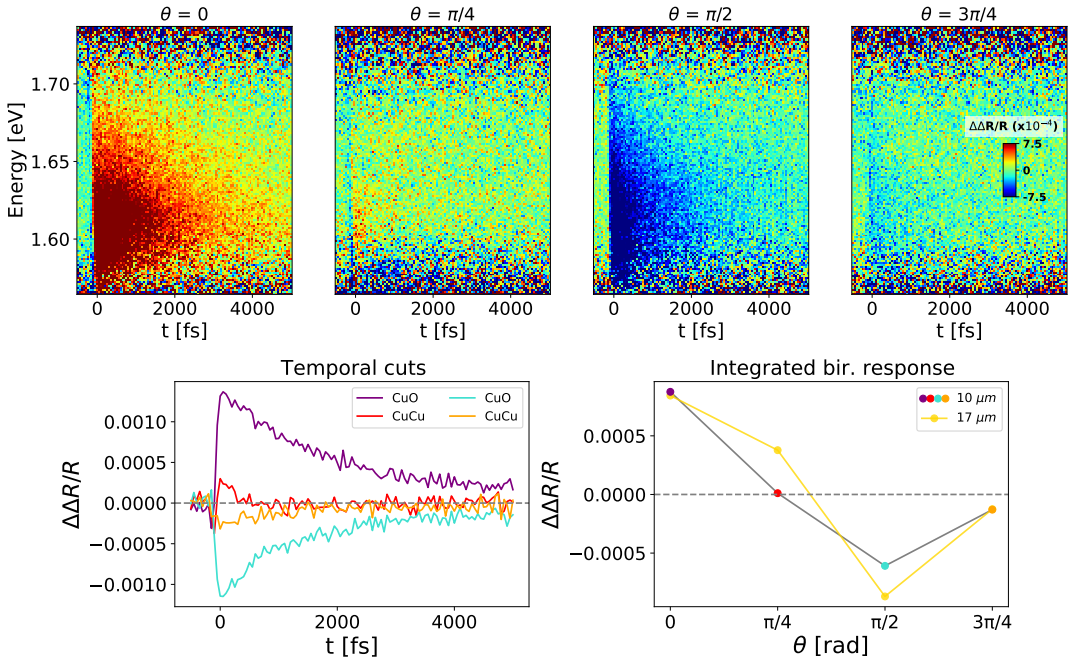

FIGURE 4.19: birefringence maps obtained on the OP sample with $E_{pump} = 10\,\mu m$ and $\hat{e}_{pump} \parallel CuCu$. Temporal cuts (bottom-left) and angle dependence plots (bottom-right) are obtained by integrating the signal on the same intervals of Figure 4.17.

$\hat{e}_{pump} \parallel CuCu$						
θ	1^{st} order model	3^{rd} order model	E_{pump}=17 μm		E_{pump}=10 μm	
			UD	OP	UD	OP
0	✓	✓	✓	✓	✓	✓
$\pi/4$	✓	✗	✗	✓	✗	✗
$\pi/2$	✓	✓	✓	✓	✓	✓
$3\pi/4$	✓	✗	✗	✗	✗	✗

TABLE 4.1: Summary of the results for $\hat{e}_{pump} \parallel CuCu$. To build this table, we considered just the long-living signals

Comparison with the models

In this section we compare the obtained results for the two pump energies with the predictions of the *First* and *Third order* model.
In Figure 4.20 we plot the integrated birefringence signals of the UD sample. Starting from the data with $E_{pump} = 17\,\mu m$ (black circles), we see that they're well described by the *Third order* model. Indeed, we measure a signal just at $\theta = 0, \pi/2$ that corresponds to the B_{2g} excitation. On the contrary, we measure no signal at $\theta = \pi/4, 3\pi/4$ where the *First order* model predicts a contribution from the B_{1g} mode.

Data obtained with $E_{pump} = 10\,\mu m$ show a different behavior (brown circles). Indeed, the positive signal measured at $\theta = \pi/4$ would be compatible with the *First order* model, but the positive signal $\theta = 3\pi/4$ is strongly in contrast with the expected negative signal of the B_{1g} excitation. Therefore, also by taking into account the short-living nature of the signals[12] at $\theta = \pi/4, 3\pi/4$ (see Figure 4.18), we link them to a spurious birefringence signal that isn't related to the B_{1g} signal. In particular, since the signal doesn't depend on the orientation of the probe (i.e. it is positive both at $\theta = \pi/4$ and $\theta = 3\pi/4$), we tentatively link it to a residual contribution from the A_{1g} mode.
In conclusion, for the UD sample the *Third order* model is respected also in the case of $E_{pump} = 10\,\mu m$.

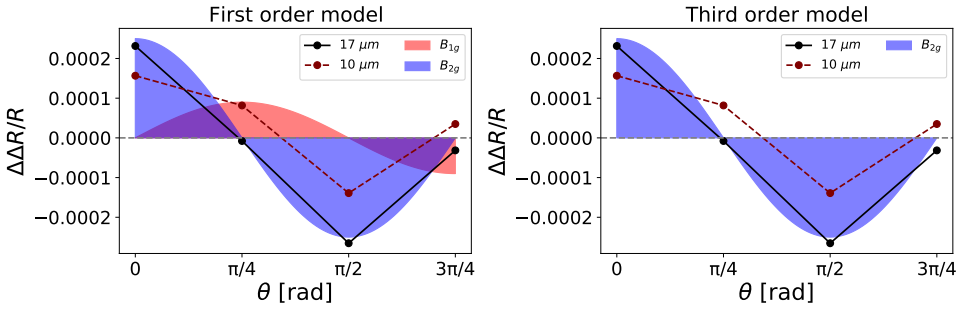

FIGURE 4.20: comparison of the integrated birefringence signals of the UD sample with the *First* and *Third order* model .

In Figure 4.21 we plot the integrated birefringence signals for the OP sample.
Starting from the data collected with $E_{pump} = 10\,\mu m$ (brown circles), we report a good agreement with the *Third order* model, with non-zero signals just when the probe polarization is set parallel to the CuO axis of the sample ($\theta = 0, \pi/2$).
Notably, the integrated signals obtained with $E_{pump} = 17\,\mu m$ show a really different behavior. Indeed, we measure a positive signal at $\theta = \pi/4$ that derives from a long-living signal (see Figure 4.17, red trace) and hence is compatible with a B_{1g} excitation. As a consequence, the *Third order* model isn't descriptive of the data.
We point out that it isn't clear if the weaker negative signal[13] at $\theta = 3\pi/4$ is related to the B_{1g} mode too or if it has a different origin. Hence, we can't undoubtedly assert that the *First order* model is descriptive of OP data with $E_{pump} = 17\,\mu m$.

Summarizing, when the pump polarization is set parallel to the CuCu axis, birefringence measurements are well described by the *Third order* model when the energy of the pump is above the one of the superconducting gap ($E_{pump} = 10\,\mu m$) for both samples and when

[12] We recall that, from our fluence studies, we expect the B_{1g} signal to live for few *ps* (see Figure 4.13).
[13] Notably, the negative signal originates from a fast decaying response (orange trace, 4.17).

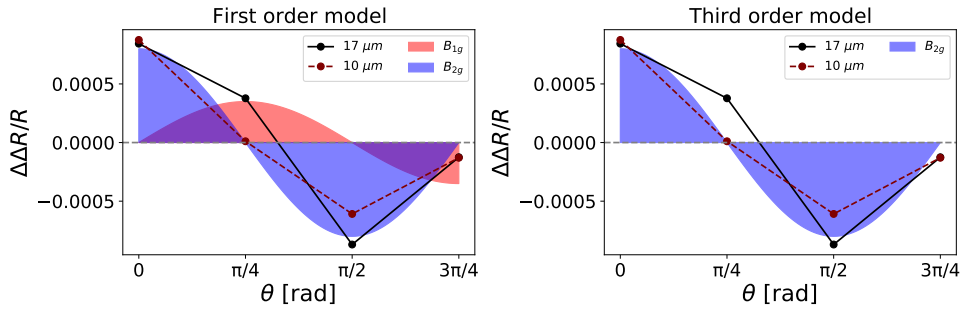

FIGURE 4.21: comparison of the integrated birefringence signals of the OP sample with the *First* and *Third order* model.

$E_{pump} = 17\,\mu\text{m}$ for the UD sample.
In contrast, the measurements with the low-energy pump on the OP sample show an asymmetric response when $\hat{e}_{probe} \parallel CuCu$ that can't be described by the *Third order* model.

Pump ∥ CuO

We proceed by presenting the birefringence measurements performed with the pump polarization set parallel to the CuO axis of the sample. According to the *Third order* model, this geometry allows for the isolation of the B_{1g} mode that is revealed when the probe polarization is aligned with the CuCu axis.

Pump energy $17\,\mu m$

In Figure 4.22 we plot the birefringence maps obtained with the low energy pump ($E_{pump} = 17\,\mu m$) on the UD sample. We unveil a strong asymmetric response. Indeed, while positive and negative signals alternate when the probe polarization is parallel to the CuO axis (positive signals at $\theta = 0, \pi$ and negative signals at $\theta = \pi/2, 3\pi/2$), we detect just positive signals when $\hat{e}_{probe} \parallel CuCu$ ($\theta = \pi/4, 5\pi/4$), missing the correspondent negative values ($\theta = 3\pi/4, 7\pi/4$).
By looking at the temporal cuts (Figure 4.22, bottom-left) and at the energy and time integrated signals (Figure 4.22, bottom-right) it is clear that the signals measured at $\theta = \pi/4, 5\pi/4$ (red traces) pertain to the superconducting state.

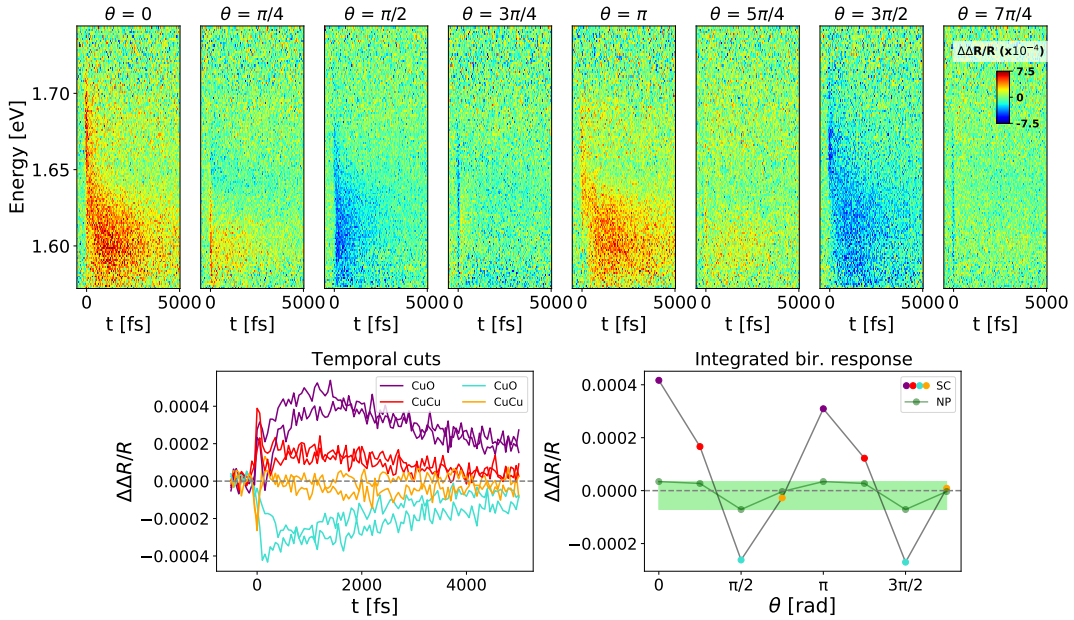

FIGURE 4.22: birefringence maps of the UD sample obtained with $\hat{e}_{pump} \parallel CuO$ and $E_{pump} = 17\,\mu m$. Temporal traces (bottom-left) are obtained by integrating over the 1.58-$1.615\,eV$ energy range and integrated signal (bottom-right) results from the integration over the same energy range and over the 0-$2\,ps$ time window.

The birefringence maps that belong to the OP sample present a non-null symmetric signal at all θ angles (Figure 4.23). In particular, positive signals are measured at $\theta = 0, 3\pi/4$ and negative ones at $\theta = \pi/4, \pi/2$.
Remarkably, the temporal traces (Figure 4.23, bottom-left) of the signals measured when the probe polarization is parallel to the CuCu axis ($\theta = \pi/4, 3\pi/4$, red and orange traces) present a fast peak and a slow recovery dynamics.

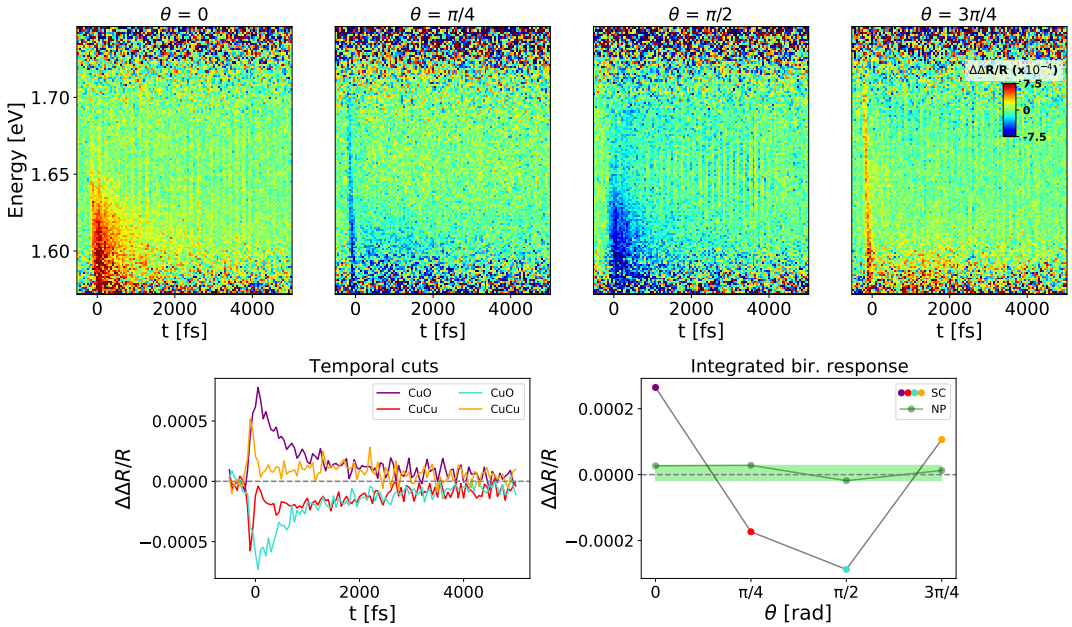

FIGURE 4.23: birefringence maps of the OP sample obtained with $\hat{e}_{pump} \parallel CuO$ and $E_{pump} = 17\,\mu\mathrm{m}$. Temporal traces (bottom-left) and integrated signals (bottom-right) are obtained by integrating over the 1.58-$1.615\,\mathrm{eV}$ energy range and the 0-$2\,\mathrm{eV}$ time window.

Pump energy $10\,\mu m$

Figure 4.24 presents the data acquired with $E_{pump} = 10\,\mu m$. We unveil an intense birefringence signal at $\theta = 0, \pi/2$ and weaker contributions at $\theta = \pi/4, 3\pi/4$.
In particular, the fast signal at $\theta = 3\pi/4$ (orange trace in Figure 4.24, bottom-left) results in a positive integrated value (Figure 4.24, bottom-right) that wasn't observed with $E_{pump} = 17\,\mu m$.

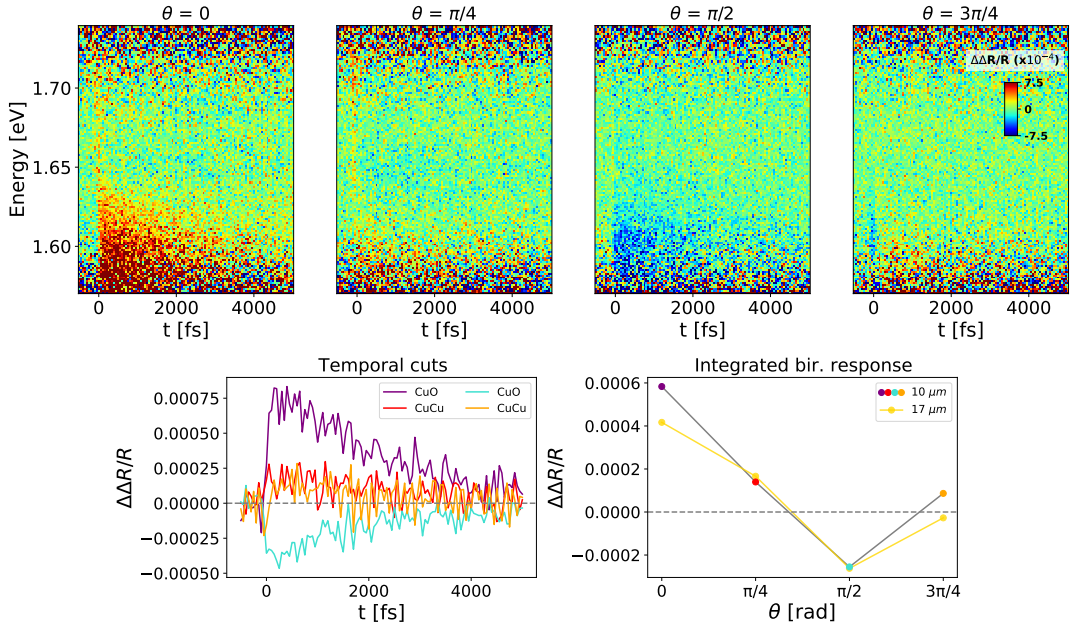

FIGURE 4.24: birefringence maps of the UD sample obtained with $\hat{e}_{pump} \parallel CuO$ and $E_{pump} = 10\,\mu m$.

Finally, we display the birefringence maps of the OP sample with the high energy pump in Figure 4.25.
In this case, the main difference with respect to the maps acquired with the low energy pump ($E_{pump} = 17\,\mu m$) resides in the disappearing of the negative signal at ($\theta = 3\pi/4$). Instead, we detect a fast signal without the slow recovery dynamics (red trace in Figure 4.25, bottom-left).

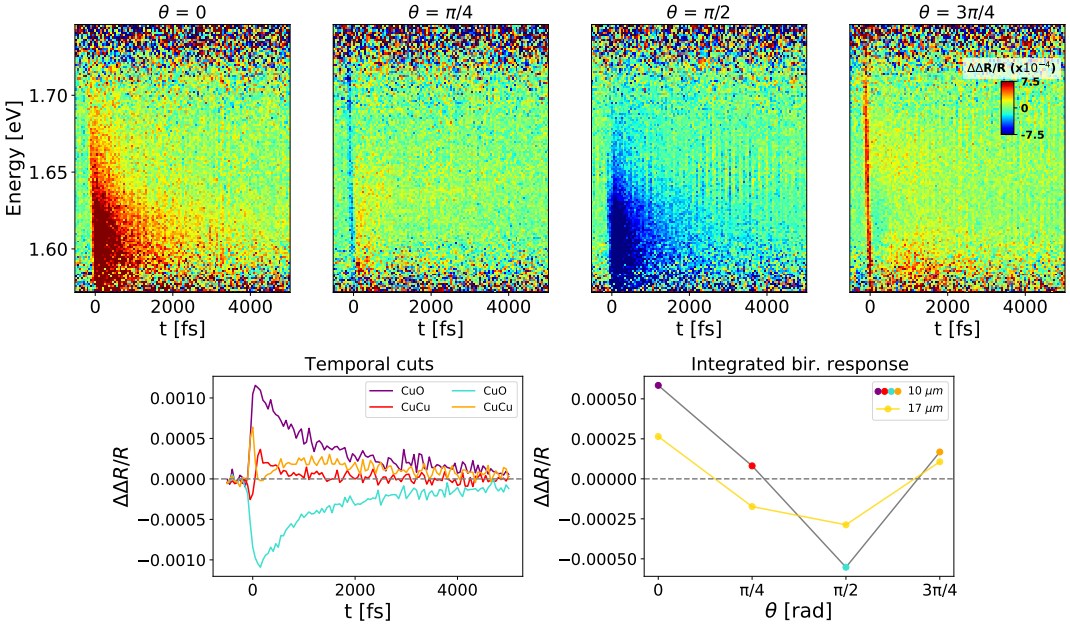

FIGURE 4.25: birefringence maps of the OP sample obtained with $\hat{e}_{pump} \parallel CuO$ and $E_{pump} = 10\,\mu\text{m}$.

Comparison with the models

We now comment on the dependence of the integrated birefringence signals from the probe polarization angle in order to compare the experimental results with the predictions of the models.
Starting from the UD sample, we see that for both pump energies, the *Third order* model is never respected (Figure 4.26). Indeed, we measure the most intense birefringence signal when the probe polarization is parallel to the CuO axis (i.e. $\theta = 0, \pi/2$), where the *Third order* model actually predicts nodes. Recalling the *First order* model, we link those signals to the B_{2g} excitation.
Moreover, also the *First order* model fails in describing the experimental observations. The positive signal measured at $\theta = \pi/4$ for both pump wavelengths doesn't couple to a negative signal at $\theta = 3\pi/4$, hence determining a strong asymmetric response. Especially concerning the measurements at $E_{pump} = 17\,\mu\text{m}$, where the node at $\theta = 3\pi/4$ is unambiguous, the periodicity of the B_{1g} signal scales as a $cos^2\theta$-like function rather than the predicted $sin2\theta$ behavior.

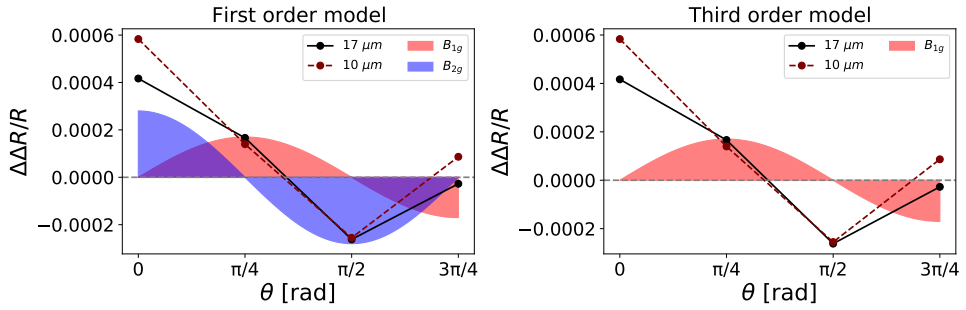

FIGURE 4.26: comparison of the integrated birefringence signals of the UD sample, obtained with $\hat{e}_{pump} \parallel CuO$, with the *First* and *Third order* model.

In Figure 4.27 we report the comparison of the integrated signals with the models for the OP sample.
As for the UD sample, also in this case the *Third order* model fails in reproducing the observed data, since we measure B_{2g} contributions ($\theta = 0, \pi/2$) that are predicted just by the *First order* model.
When the probe polarization is aligned to the CuCu axis ($\theta = \pi/4, 3\pi/4$), we measure a symmetric response when $E_{pump} = 17\,\mu\text{m}$ and an asymmetric one when $E_{pump} = 10\,\mu\text{m}$. Therefore, the measurements with the low-energy pump are consistent with the *First order* description, while the high-energy ones aren't represented by any of the proposed models.
We point out that, in general, the sign of the birefringence signal isn't meaningful, since it arbitrarily depends on how we subtract the two projections of the probe[14] However, since we are consistent with our choices throughout the whole dataset presented, it isn't clear why, for the OP sample, we measure a negative signal when $\theta = \pi/4$ and $\hat{e}_{pump} \parallel CuO$ and a positive one when $\hat{e}_{pump} \parallel CuCu$ (see Figure 4.21).

[14] i.e. how we decide which is the + and the - projection in equations 4.14 and 4.15.

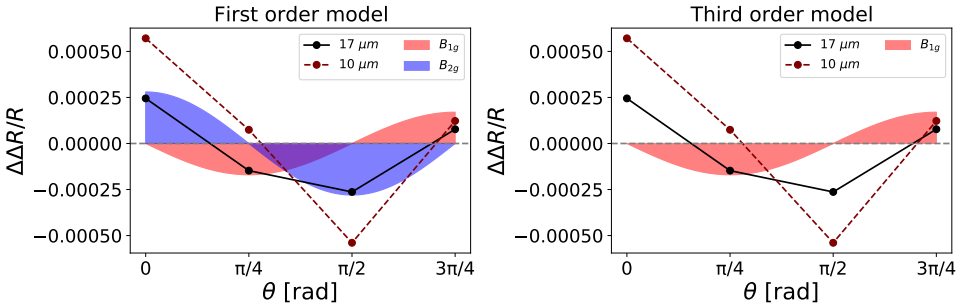

FIGURE 4.27: comparison of the integrated birefringence signals of the OP sample, obtained with $\hat{e}_{pump} \parallel CuO$, with the *First* and *Third order* model.

$\hat{e}_{pump} \parallel CuO$						
θ	1^{st} order model	3^{rd} order model	E_{pump}=17 μm		E_{pump}=10 μm	
			UD	OP	UD	OP
0	✓	✗	✓	✓	✓	✓
$\pi/4$	✓	✓	✓	?	✗	✗
$\pi/2$	✓	✗	✓	✓	✓	✓
$3\pi/4$	✓	✓	✗	?	✗	?

TABLE 4.2: Summary of the results for $\hat{e}_{pump} \parallel CuO$. The table reports just the long-living signals.

4.4 Discussion and conclusions

We started our investigation on the selection rules of B_{1g} and B_{2g} electronic modes thinking that they would have obeyed either the *First* or the *Third order* model. However, a puzzling scenario emerged from the experimental results, that we summarize in the following paragraphs.

We always measure an intense birefringence signal when the probe polarization is set parallel to the CuO sample axis ($\theta = 0, \pi/2$). In the *First order* formalism, this probe configuration allows for the isolation of the B_{2g} mode, that we recall is the electronic excitation localized at the *nodes* of the first Brillouin zone (Figure 4.7). In other words, in the absence of a superconducting gap, excitations aren't sensitive to the pump polarization and/or to the pump energy.

Results obtained when $\hat{e}_{probe} \parallel CuCu$ are much more diversified. There are configurations under which we don't observe any B_{1g} signal ($\hat{e}_{pump} \parallel CuCu$ on the UD sample or $\hat{e}_{pump} \parallel CuCu$ + $E_{pump} = 10\,\mu\mathrm{m}$ on the OP sample) and the data are described by the *Third order* model. Then, there are conditions under which we measure both positive and negative signals ($\hat{e}_{pump} \parallel CuO$ + $E_{pump} = 17\,\mu\mathrm{m}$) and therefore data are represented by the *First order* model. Finally, there are configurations where the birefringence signal is strongly asymmetric and doesn't respond to neither the *First* nor the *Third order* description.
In particular, we recall the measurements performed with $\hat{e}_{pump} \parallel CuCu$ and $E_{pump} = 17\,\mu\mathrm{m}$ on the OP sample (Figure 4.17) and the ones with $\hat{e}_{pump} \parallel CuO$ and $E_{pump} = 17\,\mu\mathrm{m}$ on the UD sample (Figure 4.22). In both cases, we measure a different response along the two CuCu axis of the CuO_2 plaquette: at $\theta = \pi/4$ we measure a positive signal while at $\theta = 3\pi/4$ we detect a node.
This evidence can't be explained by a model that is based on the D_{4h} point group, whether it accounts for the pump polarization or not. Therefore, we theorize that our system undergoes a symmetry reduction under the action of the pump, as proposed in [50]. Since we observe an anisotropic response along the two CuCu axis, we propose a $D_{4h} \rightarrow D_{2h}$ pump-induced transition. Unfortunately, by testing the selection rules of the D_{2h} point group (see Appendix B), we unveil that no asymmetric response is expected also in this case.

Time-reversal symmetry breaking

Hence, we adopt a more general treatment, in the attempt of understanding if there is a specific symmetry that explains our experimental findings. In particular, we focus on the general formulation of the interaction of the probe pulse with the sample. We write the general 2x2 Raman tensor of the system[15]

$$M = \begin{pmatrix} A & B \\ C & D \end{pmatrix}$$

[15] We underline that this formulation is valid for both the *First order* and the *Third order* model. Indeed, whether we take into account or not the action of the pump, we always end up with a 2x2 matrix M on which we compute the action of the initial $|I\rangle$ and final $|F\rangle$ states of the probe as $\langle F|M|I\rangle$.

and we compute the action of the incoming $|I\rangle = \begin{pmatrix} cos\theta \\ sin\theta \end{pmatrix}$ and scattered probe $|F\rangle = \begin{pmatrix} cos\alpha \\ sin\alpha \end{pmatrix}$ as:

$$\begin{aligned} M_{F,I} = \langle F|M|I\rangle &= \begin{pmatrix} cos\alpha, & sin\alpha \end{pmatrix} \begin{pmatrix} A & B \\ C & D \end{pmatrix} \begin{pmatrix} cos\theta \\ sin\theta \end{pmatrix} \\ &= A\, cos\theta\, cos\alpha + C\, cos\theta\, sin\alpha + B\, sin\theta\, cos\alpha + D\, sin\theta\, sin\alpha \end{aligned} \tag{4.16}$$

In analogy with Section 4.2.3, we isolate the birefringence signal by imposing $\alpha = \theta \pm 45°$ and by subtracting the two projections $\Delta R^{\pm}$:

$$\Delta\Delta R = \Delta R^{+} - \Delta R^{-} = \frac{D - A}{2} sin2\theta + C\, cos^2\theta - B sin^2\theta \tag{4.17}$$

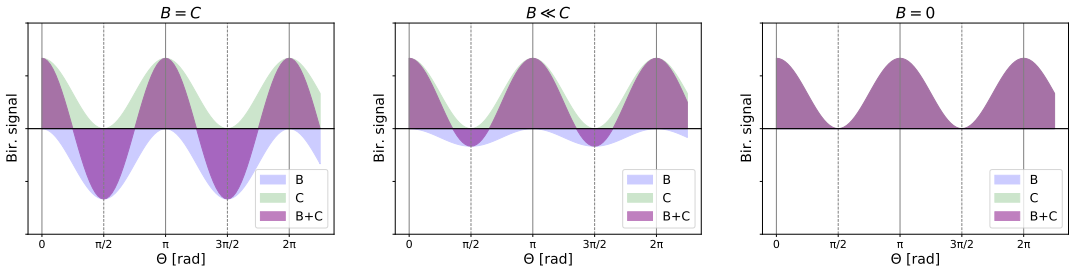

FIGURE 4.28: polarization dependence of the out-of-diagonal components of the Raman matrix M. By increasing the unbalance between the B and the C term, we go from a $cos2\theta$ to a $cos^2\theta$ dependence of the birefringence signal from the probe polarization angle.

We notice that there are three different contributions characterized by a different dependence from the orientation of the probe polarization:

- the first term involves A and D terms and varies periodically with $sin2\theta$. Typically, A_g modes are characterized by $A = D$ and so are not detected by birefringence measurements[16]. On the contrary, E_g and B_g modes show $A = -D$ and therefore they preserve the $sin2\theta$ dependence from the probe polarization angle [48].
- the last two terms, related to the out-of-diagonal components, depend on $cos^2\theta$ and $sin^2\theta$, respectively. When $B = C$, the Raman tensor is symmetric and it gives rise to B_g and E_g excitations [48] that vary with $cos2\theta$ (Figure 4.28, left). However, if $B \neq C$ and $B << C$ (or vice versa) the signal will be dominated by the intense C (B) component (Figure 4.28, center) and, in the limit of $B \to 0$ ($C \to 0$), the signal will have a $cos^2\theta$ ($sin^2\theta$) periodicity (Figure 4.28, right).

We underline that no symmetry point group presents an asymmetric Raman tensor at equilibrium [48].

Summarizing, we discover that an unbalance between the out-of-diagonal elements of the Raman tensor can generate a $cos^2\theta$-like dependence of the birefringence signal, that indeed matches our observations (see Figure 4.22). Rephrasing, a distortion of the Raman tensor symmetry may explain our results.

[16] We point out that this isn't always true. Indeed, there are cases (see Appendix B) where A_g modes show $A \neq D$ and hence determine a birefringence signal.

Remarkably, the main implication of an asymmetry in the Raman tensor is the breaking of time-reversal symmetry. This leads to one of the open problems in Cuprates, i.e. the existence of a low-temperature state where time-reversal symmetry is broken.
Different models for such states have been proposed [53–55] and several experiments of tunneling and charge transport have shown positive indications of their existence [56–61]. Yet, no unanimous consensus has been reached on the topic.
In this perspective, the possibility of transiently induce a state where time-reversal symmetry is broken is particularly suggestive.

Nonetheless, we underline that further studies are needed to properly validate our results and understand the nature of the symmetry-breaking process. At the moment, the only clear evidence is that a strong asymmetry of the B_{1g} signal arises when the pump is resonant to the energy of the superconducting gap ($E_{pump} = 17\,\mu\mathrm{m}$). On the contrary, we don't have an adequate understanding of the doping and pump polarization dependence of the process.
Therefore, we plan to investigate other $Bi_2Sr_2CaCu_2O_{8+\delta}$ samples characterized by different doping levels. Moreover, measuring intermediate θ angles of the probe polarization would provide a complete polarimetric study of the asymmetric B_{1g} response and this would confirm or not the $cos^2\theta$ angular dependence of the birefringence signal.

Appendices

A Birefringence measurements in NP

In Figure A.1 we report the birefringence maps obtained by measuring the UD sample[17] in the normal phase (T=300 K).
By looking at the energy integrated (1.58-1.615 eV) temporal cuts (Figure A.2), we unveil no significant contribution to the birefringence signal besides a fast response that decays in less than 1 *ps*.

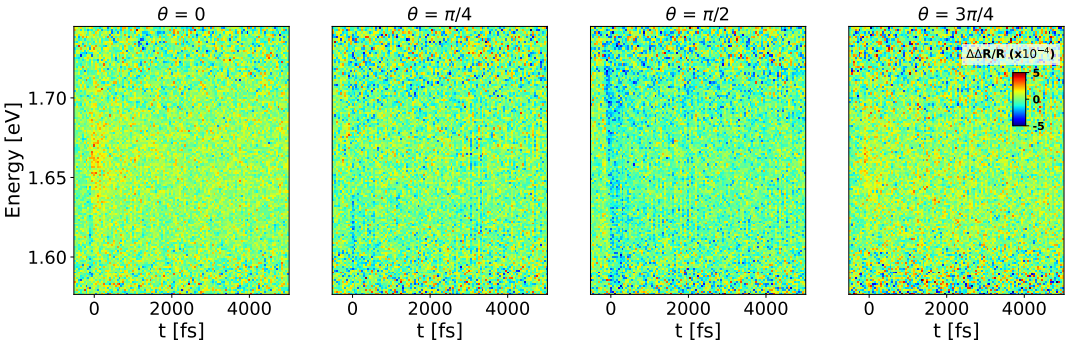

FIGURE A.1: birefringence maps obtained as a function of the probe polarization angle θ in the normal phase (NP) of the sample (T=300 K).

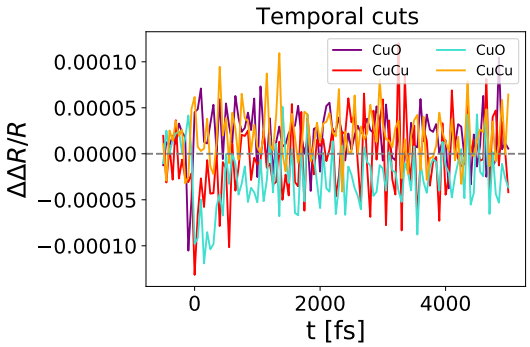

FIGURE A.2: temporal cuts of the birefringence maps reported in Figure A.1 obtained by integration in the 1.58-1.615 eV energy range.

[17] Similar results have been obtained on the OP sample.

B Selection Rules for D_{2h} symmetry group

In the following, we derive the selection rules for the D_{2h} symmetry group. According to [48], the possible excitations are:

$$A_g = \begin{pmatrix} a & 0 & 0 \\ 0 & b & 0 \\ 0 & 0 & c \end{pmatrix} B_{1g} = \begin{pmatrix} 0 & d & 0 \\ d & 0 & 0 \\ 0 & 0 & 0 \end{pmatrix} B_{2g} = \begin{pmatrix} 0 & 0 & e \\ 0 & 0 & 0 \\ e & 0 & 0 \end{pmatrix} B_{3g} = \begin{pmatrix} 0 & 0 & 0 \\ 0 & 0 & f \\ 0 & f & 0 \end{pmatrix}$$

In analogy with Chapter 4, we focus on the CuO planes (the ones orthogonal to the *z* direction) to build the 4^{th} rank Raman tensor:

$$M = \begin{pmatrix} a^2 & 0 & 0 & d^2 \\ 0 & ab & d^2 & 0 \\ 0 & d^2 & ab & 0 \\ d^2 & 0 & 0 & b^2 \end{pmatrix}$$

Notably, the only relevant modes are the ones with A_g or B_{1g} symmetry.

We now consider the action of a pump pulse with linear polarization. By defining the pump polarization angle ϕ with respect to the sample axis (CuO)

$$\begin{pmatrix} cos\phi & 0 \\ 0 & cos\phi \\ sin\phi & 0 \\ 0 & sin\phi \end{pmatrix}$$

we get:

$$\langle\phi|M|\phi\rangle = \begin{pmatrix} a^2cos^2\phi + absin^2\phi & d^2sin2\phi \\ d^2sin2\phi & abcos^2\phi + b^2sin^2\phi + \end{pmatrix}$$

Analogously, we compute the action of the probe $\begin{pmatrix} cos\theta \\ sin\theta \end{pmatrix}$ and of the analyzer $\begin{pmatrix} cos\alpha \\ sin\alpha \end{pmatrix}$. The result is:

$$\Delta R = d^2\ sin2\phi sin(\alpha+\theta) + (a\ cos^2\phi + b\ sin^2\phi)(a\ cos\theta\ cos\alpha + b\ sin\theta\ sin\alpha)$$

By setting the analyzer angle at $\alpha = \theta \pm 45°$ we get:

$$\Delta R^{\pm} = d^2 sin2\phi\Big(\frac{sin2\theta}{\sqrt{2}} \pm \frac{cos2\theta}{\sqrt{2}}\Big) + \Big(acos^2\phi + bsin^2\phi\Big)\Big[acos\theta\Big(\frac{cos\theta}{\sqrt{2}} \mp \frac{sin\theta}{\sqrt{2}}\Big) + \\ + bsin\theta\Big(\frac{sin\theta}{\sqrt{2}} \pm \frac{cos\theta}{\sqrt{2}}\Big)\Big]$$

Since we do a birefringence measurement, we're interested in the difference between the two components. The final expression for the birefringence signal is:

$$\Delta\Delta R = \sqrt{2}d^2 sin2\phi\, cos2\theta + \frac{b-a}{\sqrt{2}}(a\, cos^2\phi + b\, sin^2\phi)sin2\theta \tag{4.18}$$

We now discuss the results for three relevant configurations of the pump:

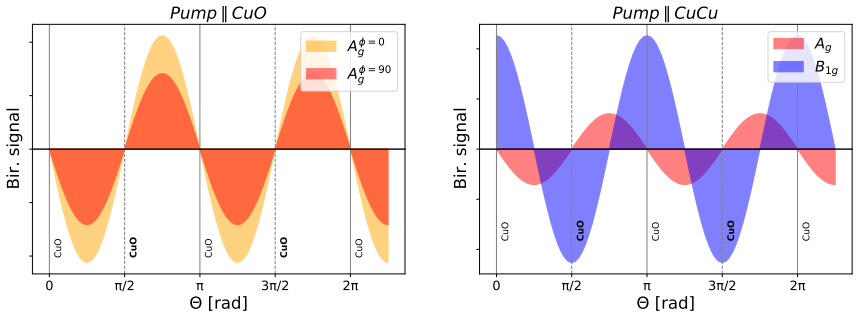

FIGURE B.1: Predictions of the model for a>b=d. Left panel: a sequence of nodes and antinodes is realized when the polarization of the pump is $\phi = 0, 90°$. We highlight that the amplitude of the signal is different for the two angles. Right panel: a signal is visible for all the probe polarization angles.

- $\phi = 0°$. Equation 4.18 reduces to:

$$\Delta\Delta R(\phi = 0) = a\frac{b-a}{\sqrt{2}} sin2\theta$$

The only contribution is the one relative to the A_g mode, that oscillates with a periodicity 2θ (see Figure B.1, left panel).

- $\phi = 45°$. Equation 4.18 becomes:

$$\Delta\Delta R(\phi = 45°) = \sqrt{2}\, d^2 cos2\theta + \frac{b^2-a^2}{2\sqrt{2}} sin2\theta$$

Both the A_g and the B_{1g} mode are selectively detected, according to the polarization of the probe. Nodes aren't predicted (Figure B.1, right panel).

- $\phi = 90°$. From equation 4.18 we obtain:

$$\Delta\Delta R(\phi = 0) = b\frac{b-a}{\sqrt{2}} sin2\theta$$

The signal is qualitative the same as in the case of $\phi = 0°$. We highlight that there is a difference in amplitude (in left panel of Figure B.1 we used $a > b$).

In summary, the Third order model for the D_{2h} symmetry point group predicts nodes when the pump is polarized parallel to the CuO axis ($\phi = 0°/90°$) and no nodes when it is polarized along the CuCu axis ($\phi = 45°$). Importantly, all the signals are characterized by a $cos2\theta$ or $sin2\theta$ angular dependence. Hence, no asymmetric signal is predicted.

References

[1] John Bardeen, Leon N Cooper, and John Robert Schrieffer. "Theory of superconductivity". In: *Physical review* 108.5 (1957), p. 1175.

[2] J George Bednorz and K Alex Müller. "Possible high T c superconductivity in the Ba- La- Cu- O system". In: *Zeitschrift für Physik B Condensed Matter* 64.2 (1986), pp. 189–193.

[3] URL: %5Curl%7Bhttps://commons.wikimedia.org/w/index.php?curid=864040%7D.

[4] J Orenstein and AJ Millis. "Advances in the physics of high-temperature superconductivity". In: *Science* 288.5465 (2000), pp. 468–474.

[5] Philip W Anderson. "New approach to the theory of superexchange interactions". In: *Physical Review* 115.1 (1959), p. 2.

[6] DJ Scalapino, E Loh Jr, and JE Hirsch. "D-wave pairing near a spin-density-wave instability". In: *Physical Review B* 34.11 (1986), p. 8190.

[7] Douglas J Scalapino. "The case for dx2- y2 pairing in the cuprate superconductors". In: *Physics Reports* 250.6 (1995), pp. 329–365.

[8] Douglas J Scalapino. "A common thread: The pairing interaction for unconventional superconductors". In: *Reviews of Modern Physics* 84.4 (2012), p. 1383.

[9] H Takagi et al. "Systematic evolution of temperature-dependent resistivity in La 2- x Sr x CuO 4". In: *Physical review letters* 69.20 (1992), p. 2975.

[10] JW Lorama et al. "Specific heat evidence on the normal state pseudogap". In: *Journal of Physics and Chemistry of Solids* 59.10-12 (1998), pp. 2091–2094.

[11] AV Puchkov, DN Basov, and T Timusk. "The pseudogap state in high-superconductors: an infrared study". In: *Journal of Physics: Condensed Matter* 8.48 (1996), p. 10049.

[12] HJ Tao, Farun Lu, and EL Wolf. "Observation of pseudogap in Bi2Sr2CaCu2O8+ δ single crystals with electron tunneling spectroscopy". In: *Physica C: Superconductivity* 282 (1997), pp. 1507–1508.

[13] N Miyakawa et al. "Strong dependence of the superconducting gap on oxygen doping from tunneling measurements on Bi 2 Sr 2 CaCu 2 O 8- δ". In: *Physical review letters* 80.1 (1998), p. 157.

[14] Ch Renner et al. "Pseudogap precursor of the superconducting gap in under-and overdoped Bi 2 Sr 2 CaCu 2 O 8+ δ". In: *Physical Review Letters* 80.1 (1998), p. 149.

[15] T Valla et al. "The ground state of the pseudogap in cuprate superconductors". In: *science* 314.5807 (2006), pp. 1914–1916.

[16] VJ Emery and SA Kivelson. "Importance of phase fluctuations in superconductors with small superfluid density". In: *Nature* 374.6521 (1995), pp. 434–437.

[17] Michael R Norman, D Pines, and C Kallin. "The pseudogap: friend or foe of high T c?" In: *Advances in Physics* 54.8 (2005), pp. 715–733.

[18] Su-Di Chen et al. "Incoherent strange metal sharply bounded by a critical doping in Bi2212". In: *Science* 366.6469 (2019), pp. 1099–1102.

[19] Angela Kopp, Amit Ghosal, and Sudip Chakravarty. "Competing ferromagnetism in high-temperature copper oxide superconductors". In: *Proceedings of the National Academy of Sciences* 104.15 (2007), pp. 6123–6127.

[20] Bernardo Barbiellini and Thomas Jarlborg. "Importance of local band effects for ferromagnetism in hole-doped La 2 CuO 4 cuprate superconductors". In: *Physical review letters* 101.15 (2008), p. 157002.

[21] Johannes Nokelainen et al. "Ab initio description of the Bi 2 Sr 2 CaCu 2 O 8+ δ electronic structure". In: *Physical Review B* 101.21 (2020), p. 214523.

[22] WN Hardy et al. "Precision measurements of the temperature dependence of λ in YBa 2 Cu 3 O 6.95: Strong evidence for nodes in the gap function". In: *Physical Review Letters* 70.25 (1993), p. 3999.

[23] JR Kirtley et al. "Symmetry of the order parameter in the high-Tc superconductor YBa2Cu3O7-δ". In: *Nature* 373.6511 (1995), pp. 225–228.

[24] Dale J Van Harlingen. "Phase-sensitive tests of the symmetry of the pairing state in the high-temperature superconductors—Evidence for d x 2- y 2 symmetry". In: *Reviews of Modern Physics* 67.2 (1995), p. 515.

[25] Qiangqiang Gu et al. "Directly visualizing the sign change of d-wave superconducting gap in Bi2Sr2CaCu2O8+ δ by phase-referenced quasiparticle interference". In: *Nature Communications* 10.1 (2019), p. 1603.

[26] Federico Cilento et al. "Photo-enhanced antinodal conductivity in the pseudogap state of high-T c cuprates". In: *Nature communications* 5.1 (2014), p. 4353.

[27] Claudio Giannetti et al. "Ultrafast optical spectroscopy of strongly correlated materials and high-temperature superconductors: a non-equilibrium approach". In: *Advances in Physics* 65.2 (2016), pp. 58–238.

[28] Angela Montanaro et al. "Dynamics of non-thermal states in optimally-doped Bi 2 Sr 2 Y 0.08 Ca 0.92 Cu 2 O 8+ δ revealed by mid-infrared three-pulse spectroscopy". In: *arXiv preprint arXiv:2310.10279* (2023).

[29] Allen Rothwarf and BN Taylor. "Measurement of recombination lifetimes in superconductors". In: *Physical Review Letters* 19.1 (1967), p. 27.

[30] YH Liu et al. "Direct observation of the coexistence of the pseudogap and superconducting quasiparticles in Bi 2 Sr 2 CaCu 2 O 8+ y by time-resolved optical spectroscopy". In: *Physical review letters* 101.13 (2008), p. 137003.

[31] Claudio Giannetti et al. "Discontinuity of the ultrafast electronic response of underdoped superconducting Bi 2 Sr 2 CaCu 2 O 8+ δ strongly excited by ultrashort light pulses". In: *Physical Review B* 79.22 (2009), p. 224502.

[32] F Boschini et al. "Collapse of superconductivity in cuprates via ultrafast quenching of phase coherence". In: *Nature materials* 17.5 (2018), pp. 416–420.

[33] Matthias Beck et al. "Transient increase of the energy gap of superconducting NbN thin films excited by resonant narrow-band terahertz pulses". In: *Physical Review Letters* 110.26 (2013), p. 267003.

[34] Daniele Fausti et al. "Light-induced superconductivity in a stripe-ordered cuprate". In: *science* 331.6014 (2011), pp. 189–191.

[35] Wanzheng Hu et al. "Optically enhanced coherent transport in YBa 2 Cu 3 O 6.5 by ultrafast redistribution of interlayer coupling". In: *Nature materials* 13.7 (2014), pp. 705–711.

[36] Matteo Mitrano et al. "Possible light-induced superconductivity in K3C60 at high temperature". In: *Nature* 530.7591 (2016), pp. 461–464.

[37] F Giusti et al. "Signatures of enhanced superconducting phase coherence in optimally doped Bi 2 Sr 2 Y 0.08 Ca 0.92 Cu 2 O 8+ δ driven by midinfrared pulse excitations". In: *Physical review letters* 122.6 (2019), p. 067002.

[38] Francesca Giusti et al. "Anisotropic time-domain electronic response in cuprates driven by midinfrared pulses". In: *Physical Review B* 104.12 (2021), p. 125121.

[39] A. von Hoegen et al. "Amplification of Superconducting Fluctuations in Driven $YBa_2Cu_3O_{6+x}$". In: *Phys. Rev. X* 12 (3 July 2022), p. 031008. DOI: 10.1103/PhysRevX.12.031008. URL: https://link.aps.org/doi/10.1103/PhysRevX.12.031008.

[40] Sebastian Fava et al. "Magnetic field expulsion in optically driven YBa2Cu3O6. 48". In: *Nature* (2024), pp. 1–6.

[41] Roman Mankowsky et al. "Nonlinear lattice dynamics as a basis for enhanced superconductivity in YBa2Cu3O6. 5". In: *Nature* 516.7529 (2014), pp. 71–73.

[42] Chandrasekhara Venkata Raman and Kariamanikkam Srinivasa Krishnan. "A new type of secondary radiation". In: *Nature* 121.3048 (1928), pp. 501–502.

[43] SB Dierker et al. "Electronic raman scattering by superconducting-gap excitations in Nb 3 Sn and V 3 Si". In: *Physical review letters* 50.11 (1983), p. 853.

[44] Thomas P Devereaux and Rudi Hackl. "Inelastic light scattering from correlated electrons". In: *Reviews of modern physics* 79.1 (2007), p. 175.

[45] Adolf Smekal. "Zur quantentheorie der dispersion". In: *Naturwissenschaften* 11.43 (1923), pp. 873–875.

[46] Francesca Giusti. "Intensity and fluctuation dynamics in pump-probe experiments in complex materials". PhD thesis. University of Trieste, 2018.

[47] Angela Montanaro. "Non-equilibrium response of quantum materials to resonant low-energy electronic photo-excitations". PhD thesis. University of Trieste, 2022.

[48] Hans Kuzmany. *Solid-state spectroscopy*. 1998.

[49] Philip B Allen. "Fermi-surface harmonics: A general method for nonspherical problems. Application to Boltzmann and Eliashberg equations". In: *Physical Review B* 13.4 (1976), p. 1416.

[50] Y Toda et al. "Rotational symmetry breaking in Bi 2 Sr 2 CaCu 2 O 8+ δ probed by polarized femtosecond spectroscopy". In: *Physical Review B* 90.9 (2014), p. 094513.

[51] Y Toda et al. "Quasiparticle relaxation dynamics in underdoped Bi 2 Sr 2 CaCu 2 O 8+ δ by two-color pump-probe spectroscopy". In: *Physical Review B* 84.17 (2011), p. 174516.

[52] Francesco Randi. "Low-energy physics in strongly correlated materials via nonlinear spectroscopies". PhD thesis. University of Trieste, 2016.

[53] J Orenstein. "Optical nonreciprocity in magnetic structures related to high-T c superconductors". In: *Physical review letters* 107.6 (2011), p. 067002.

[54] Mikael Håkansson, Tomas Löfwander, and Mikael Fogelström. "Spontaneously broken time-reversal symmetry in high-temperature superconductors". In: *Nature Physics* 11.9 (2015), pp. 755–760.

[55] N Wall Wennerdal et al. "Breaking time-reversal and translational symmetry at edges of d-wave superconductors: Microscopic theory and comparison with quasiclassical theory". In: *Physical Review Research* 2.4 (2020), p. 043198.

[56] M Covington et al. "Observation of surface-induced broken time-reversal symmetry in YBa 2 Cu 3 O 7 tunnel junctions". In: *Physical review letters* 79.2 (1997), p. 277.

[57] K Krishana et al. "Plateaus observed in the field profile of thermal conductivity in the superconductor Bi2Sr2CaCu2O8". In: *Science* 277.5322 (1997), pp. 83–85.

[58] Y Dagan and G Deutscher. "Doping and magnetic field dependence of in-plane tunneling into YBa 2 Cu 3 O 7- x: possible evidence for the existence of a quantum critical point". In: *Physical Review Letters* 87.17 (2001), p. 177004.

[59] RS Gonnelli et al. "Evidence for pseudogap and phase-coherence gap separation by Andreev reflection experiments in Au/La 2-x Sr x CuO 4 point-contact junctions". In: *The European Physical Journal B-Condensed Matter and Complex Systems* 22 (2001), pp. 411–414.

[60] G Elhalel et al. "Transition from a mixed to a pure d-wave symmetry in superconducting optimally doped yba 2 cu 3 o 7- x thin films under applied fields". In: *Physical review letters* 98.13 (2007), p. 137002.

[61] David Gustafsson et al. "Fully gapped superconductivity in a nanometre-size YBa2Cu3O7–δ island enhanced by a magnetic field". In: *Nature nanotechnology* 8.1 (2013), pp. 25–30.

Part II

Femtosecond Covariance Spectroscopy

Chapter 5

Stochastic Spectroscopy for Complex Materials

Abstract

Noise is commonly associated to something disturbing, pesky, something to get rid of. This happens in everyday life, when we can't distinguish the words of our interlocutor because of the environmental noise, or in research activities, where scientists arrange complex experimental setups to minimize the amount of external noise in their measurements. Whatever the context, noise is seen as a source of degradation of a signal that we want to unveil. Nonetheless, noise isn't always detrimental to the detection of signals.
Indeed, in some cases noise can lead to the amplification of signals [1, 2] and is exploited to enhance the detection resolution [3, 4]. Moreover, quantum noise itself can carry information that is inaccessible by looking at the mean value of observables only [5, 6].

In this Chapter we present a novel approach that exploits noise to disclose weak non-linear signal in optical spectroscopy experiments: *Femtosecond Covariance Spectroscopy* (FCS). In details, FCS studies the mapping of non-linear signals into high order statistical momenta. Furthermore, by measuring multimode photonic correlations, it is possible to reveal non linear light-matter interaction features hidden to standard mean value approaches.

In this Chapter we first introduce Femtosecond Covariance Spectroscopy principles and discuss the experimental implementation of the technique. Special focus is made on the generation of uncorrelated optical pulses with a pulse shaper based on liquid-crystals technology (SLM).
We present an equilibrium study of Raman excitations performed with FCS. In particular, we explore the capabilities of the technique in measuring magnetic excitations in the ferrimagnetic compound $RbNiF_3$.
Finally, by combining pump-probe spectroscopy with FCS, we perform a dynamic study of electronic Raman scattering in the Cuprate superconductor $Bi_2Sr_2CaCu_2O_{8+\delta}$.

5.1 Basic principles

The study of non linear processes is particularly challenging because of the intrinsic weak intensity of non linear signals with respect to the linear ones. Therefore, high signal-to-noise ratios are required to unveil non linear response.
This is commonly achieved with a *mean value approach*, i.e. by reducing the level of experimental noise as much as possible and by averaging over repeated iterations of the same experiment.
In the field of ultrafast optical spectroscopies, this has led to significant efforts towards the improvement of pulse-to-pulse stability of laser sources. Nowadays, the standard of commercial laser sources for pulse-to-pulse fluctuations is <1%.

However, there are other approaches that go beyond the mean value one and emphasise the role of noise as a source of information [2, 7–10]. In this framework, each pulse represents a new experiment characterized by its proper experimental conditions. Hence, each pulse carries different information with respect to the others.
In particular, non linear light-matter interaction can imprint multimode correlation on optical pulses. Notably, the averaged response looses this additional information encoded in the single pulse that however can be recovered through other statistical tools, e.g. covariance.

Femtosecond Covariance Spectroscopy (FCS) is a technique that relies on this second approach to measure weak non linear signals in the framework of light-matter interaction. In particular, FCS quantifies multimode photonic correlations to unveil signatures of the non linear response.
Figure 5.1 illustrates the basic principles of the technique. A set of ultrashort light pulses is acquired with a single-shot frequency resolved detection. Remarkably, each spectrum is acquired independently and hence it is possible to measure multimode correlations by evaluating the covariance (or the *Pearson coefficient*, see next Section) between the different spectral components.
The outcome of a FCS experiment is a 2D map (Figure 5.1, bottom right) where every point is obtained by quantifying the correlation between the two correspondent spectral components (ν_i, ν_j).

We underline that the stability of the laser source is not a requirement anymore, but is also detrimental for FCS experiments. Indeed, if the degree of coherence of the probe pulses is too high, intrinsic correlations overcome the weaker ones established by non linear light-matter interaction and dominate the measurement.
Therefore, a crucial precondition for FCS is the use of completely uncorrelated pulses. We fulfill this requirement by introducing spectrally narrow stochastic fluctuations across the bandwidth of the probe pulses that indeed destroy the preexisting intrinsic correlations.
From the experimental point of view, this is done via *ultrafast pulse shaping*. Further details are provided in Section 5.2 and in Chapter 6.

5.1.1 Pearson coefficient

To quantify multimode correlations between the different spectral components we use the *Pearson correlation coefficient*. In general, the Pearson coefficient evaluates the degree of linear correlation between two variables. For the case of multimode photonic correlation,

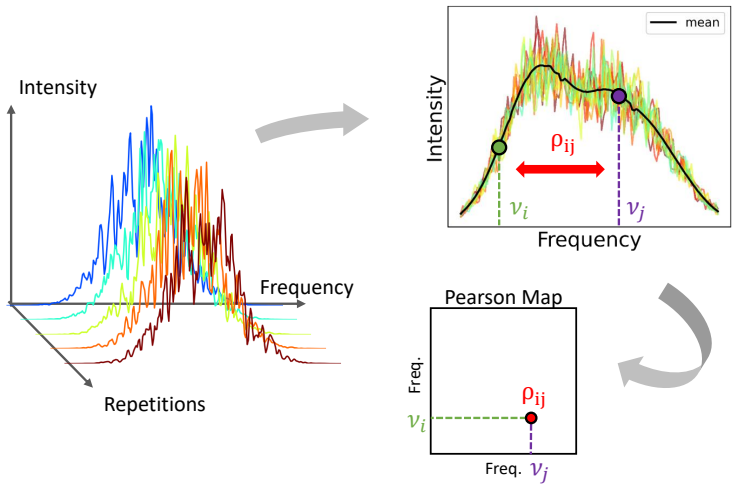

FIGURE 5.1: Femtosecond Covariance Spectroscopy. Each repetition represents a single experiment itself. With this approach, information is encoded in multimode correlations that can be measured through the Pearson coefficient ρ_{ij}. A *Pearson map* is built by computing ρ_{ij} for all the possible combinations of frequencies (ν_i, ν_j) inside the pulse spectrum.

we can express it as:

$$\rho_{ij} = \frac{\langle I(\nu_i)I(\nu_j)\rangle - \langle I(\nu_i)\rangle\langle I(\nu_j)\rangle}{\sigma_i\sigma_j} \tag{5.1}$$

where $I(\nu_i)$ represents the spectral intensity of the i^{th} mode and $\langle ...\rangle$ and σ_i indicate the mean value/standard deviation computed over the dataset of pulses.

By looking at equation 5.1 we picture the Pearson coefficient as a normalized covariance with values that range from -1 (perfect anticorrelation) to +1 (perfect correlation). Notably, if $I(\nu_i)$ and $I(\nu_j)$ are completely uncorrelated, $\rho_{ij} = 0$.
As previously mentioned, Pearson coefficient is computed for each couple of frequencies (ν_i, ν_j) of the pulse spectrum in order to build a 2D map (Figure 5.1). Each point of the *Pearson map* displays the value of ρ_{ij} calculated between the two frequencies ν_i (x-axis) and ν_j (y-axis).

In Figure 5.2 we present a set of simulations where different kind of noise is added to a set of broadband pulses. In particular, we show what are the photonic correlations associated to intensity fluctuations (Figure 5.2, a), jitter of the central frequency (Figure 5.2, b) and stochastic noise (Figure 5.2, c).
When intensity fluctuations are added to the light pulses, a positive correlation signal is measured at all frequencies (Figure 5.2, a bottom). This happens because all the spectral components experience the same sign shift with respect to the average (black line) and hence there is perfect correlation throughout the whole spectrum.
The Pearson map correspondent to the dataset affected by jitter (Figure 5.2, b bottom) presents both positive and negative correlation. Indeed, while modes lying on the same side of the pulse experience the same sign shift (as in the case of intensity fluctuations), spectral components on opposite sides of the pulse spectrum behave oppositely: when intensity is increased on the high energy modes, low energy ones see a decrease and vice versa. Consequently, modes on opposite sides of the spectrum are perfectly anticorrelated.
Finally, when stochastic fluctuations are added to the pulses (Figure 5.2, c bottom), correlation disappear (zero signal) apart from the main diagonal (visible also in the first

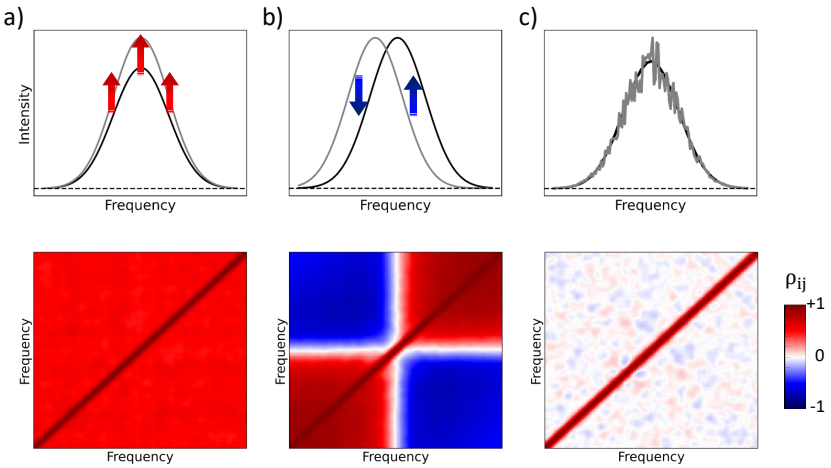

FIGURE 5.2: simulations of intensity fluctuations (a), jitter of the central frequency (b) and stochastic noise (c) on a set of light pulses with the relative Pearson maps (bottom row). Adapted from [11].

two maps), which indicates the trivial correlation between each frequency and itself.
In conclusion, the addition of stochastic noise is essential for having zero-correlation maps that otherwise would be dominated by the coherent fluctuations of the laser source.

5.1.2 Impulsive Stimulated Raman Scattering

We now consider the effect of *Impulsive Stimulated Raman Scattering* (ISRS) on a set of stochastic pulses and in particular the way it maps into photonic correlations.
ISRS is a Raman process that occurs when an ultrashort light pulse interacts with a transparent medium [12]. If the temporal duration of the pulse is shorter than the typical vibrational lifetimes, light-matter interaction causes an instantaneous perturbation of the atoms that coherently oscillate around their equilibrium position.
The stimulated nature of the process is instead related to the way Raman resonance is established [13]. Raman mode is driven into resonance by two off-resonance fields whom phase difference determines the initial phase of the oscillation.
Since ultrashort pulses are intrinsically broadband, both fields are found within the bandwidth and coherent excitation occurs[1].
In a quantum effective description, ISRS process is expressed by the following Hamiltonian [14]:

$$\hat{H}_{ISRS} = \sum_j \hat{a}_{\omega_j+\Omega}\hat{a}^\dagger_{\omega_j}\hat{b}^\dagger_\Omega + \hat{a}^\dagger_{\omega_j+\Omega}\hat{a}_{\omega_j}\hat{b}_\Omega \tag{5.2}$$

where $\hat{a}/\hat{a}^\dagger$ are the creation/annihilation operators of the photonic degrees of freedom while $\hat{b}/\hat{b}^\dagger$ are the phononic ones.
The first term indicates a *Stokes* process (Figure 5.3, a), where a photon of frequency $\omega + \Omega$ is absorbed and a ω frequency photon is emitted, creating also an elementary excitation Ω in the material. On the contrary, *Anti-Stokes* process describes the creation of a high energy photon $\omega + \Omega$ via annihilation of a photon ω and of a phonon Ω.

[1] We underline that this doesn't happen in the case of *sponaneous Raman scattering*, where a single incoming field interacts with vacuum fluctuations to generate incoherent excitations.

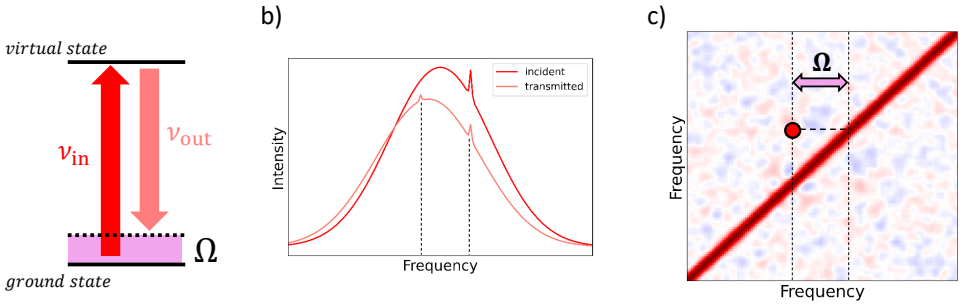

FIGURE 5.3: ISRS. We show the effect of a *Stokes* process (a) on the spectrum (b) of an incoming pulse. In particular, multimode correlation is established among different spectral components and is revealed in Pearson maps (c) by the presence of an off-diagonal signal.

We now consider ISRS, and specifically the Stokes process, in the context of a FCS experiment. Let us consider an incoming pulse with a spectrally narrow fluctuation at a given frequency ω (red curve in Figure 5.3, b). When Stokes process takes place, part of the photons are absorbed and re-emitted at lower frequencies, causing a global red-shift of the transmitted pulse (pink curve in Figure 5.3, b). Importantly, the fluctuation introduced at ω will be mapped onto the spectral component $\omega - \Omega$, hence establishing multimode correlation between the two modes. By repeating the measurement with different stochastic fluctuations, correlation will be revealed by the presence of an off-diagonal signal in the *Pearson map.*

5.1.3 FCS on α- quartz

In the following, we present an equilibrium study of Raman scattering in α-quartz performed with FCS [7].
Figure 5.4 compares the Pearson maps obtained when probe pulses interact (right) or not (left) with the crystalline α-quartz sample before being detected. First, the left map confirms that the experiment is performed with uncorrelated light pulses, since only the trivial correlation signal along the diagonal ($\omega_i = \omega_j$) is present.
Oppositely, when light interacts with the Raman-active medium, additional correlations appear (Figure 5.4, right) as off diagonal sidebands. Remarkably, the distance of the sidebands from the main diagonal matches the Raman shifts of the main vibrational modes in α-quartz.
This indicates ISRS has generated correlation between all the modes which differ just the energy of a Raman excitation.
We point out that correlation features appear as diagonal sidebands in Pearson maps because ISRS is a frequency-independent process and hence can occur throughout the whole pulse spectrum.

5.1.4 Noise configurations

So far, we have discussed the injection of stochastic noise as an essential tool to destroy preexisting photonic correlations and unveil the Raman signatures of light-matter interaction. However, we haven't analyzed yet the possible noise configurations that can be adopted in a FCS experiment:

- when stochastic fluctuations are added to the whole frequencies that lie in the pulse spectrum, we have the so-called *full noise modulation*.

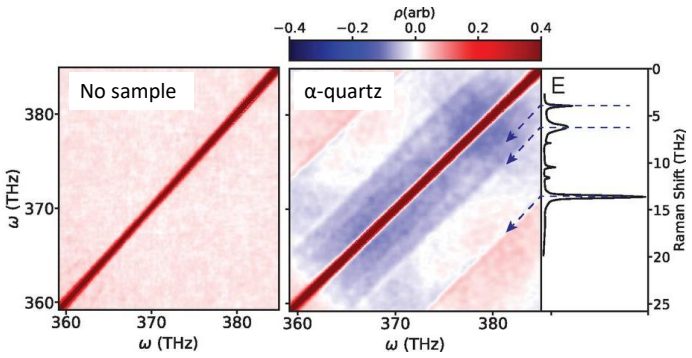

FIGURE 5.4: FCS experiment on crystalline α-quartz. Adapted from [7].

- since ultrafast pulse shaping allows to independently control the different spectral components of the probe (see Section 5.2), we can selectively add stochastic fluctuations to a defined spectral region. We refer to this configuration as *partial noise modulation*.
- by adding stochastic fluctuations to a selected region of the spectrum (as in the case of partial noise modulation) and setting at zero the spectral amplitude of the remaining modes, we achieve the configuration of *mean value shaping*.

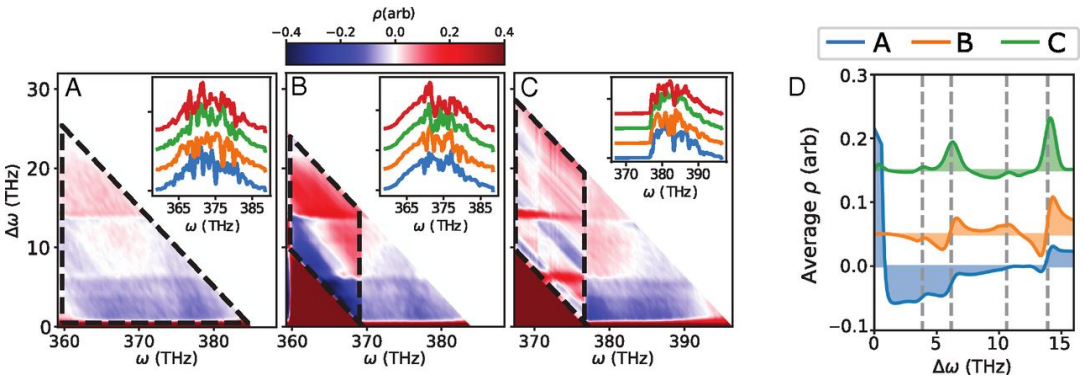

FIGURE 5.5: FCS with different noise configurations. The rolled Pearson maps of the *full* (a), *partial noise modulation* (b) and *mean value shaping* (c) are displayed with the correspondent integrated traces (d). From [7].

In Figure 5.5 we present the results of FCS experiments performed with the three different noise configurations on an α-quartz sample [7]. By integrating the rolled Pearson maps[2] (Figure 5.5, d), it is clear that the lineshape of the Raman correlations depends on the specific noise configuration adopted, as a consequence of the self-heterodyining character of ISRS. Indeed, when a heterodyining field is present (full and partial noise modulation), the lineshape is dispersive, while in the case of mean value shaping, where there is no heterodyining field, we observe a completely positive lineshape.
Moreover, we underline that the visibility of the Raman features is enhanced when the heterodyining field is coherent (orange line) with respect to the case where it is affected by stochastic fluctuations (blue line).

[2]With respect to the standard Pearson maps showed in Figure 5.4, *rolled Pearson maps* are obtained by rolling the 2D data in order to display the main diagonal on the x-axis and the distance in frequency from it on the y-axis. Since the map is symmetric, just half of it is plotted.

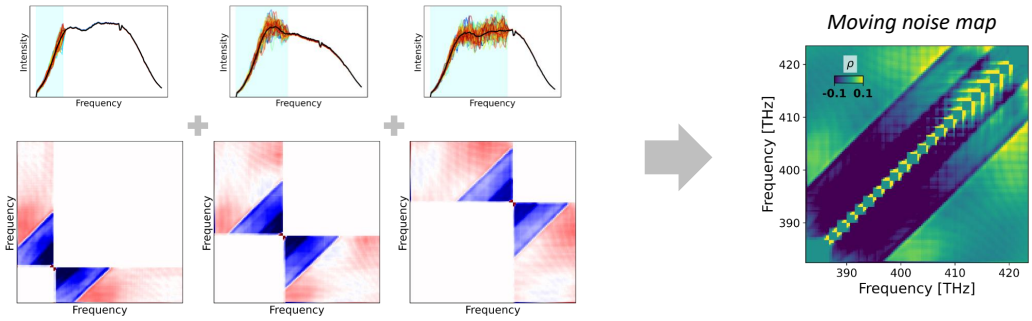

FIGURE 5.6: *moving noise configuration*. By changing the extension of the stochastic region, we collect a set of Pearson maps that we combine all together in a *moving noise* map (right), where we display the correlation signal of partial modulation on the whole spectrum.

5.1.5 Moving noise configuration

When we use *partial noise modulation*, we selectively add stochastic fluctuations to a limited region of the pulse spectrum. In this way, we obtain a pulse that is coherent on a side of the spectrum and stochastic on the other one. This reflects also into the Pearson maps, where 4 quadrants are associated to the possible combinations of the different spectral regions: coherent-coherent, stochastic-stochastic and 2 mixed coherent-stochastic quadrants. Since the signal benefits of a coherent heterodyining field [7], the meaningful quadrants are the mixed ones.
By considering just the mixed quadrants, we measure the correlation signal on a limited region of the 2D map, losing the information encoded in the stochastic-stochastic[3] and coherent-coherent quadrants. This is not a problem if the system has a uniform spectral response, but can be an important issue in the opposite case.

For this reason, we introduce the *moving noise configuration*, i.e. a static measurement where the edge frequency of the stochastic/coherent regions is shifted across the whole spectrum. In this way, we obtain a set of Pearson maps where the mixed coherent-stochastic quadrants are localized on different regions of the 2D map. By summing them and normalizing the map[4], we obtain a *moving noise map* (Figure 5.6) that displays the characteristic signal of *partial modulation* on the whole spectral range.

In Figure 5.7 we show an example of moving noise map obtained with an α-quartz sample. Both in the correlation 2D map (Figure 5.7, a) and in the integrated curves (Figure 5.7, b and c), correlation signals emerge in correspondence of the 6.2, 10.7 an $14\,\mathrm{THz}$ phonon frequencies.
By looking at the integrated curves of the single *partial modulation* maps (Figure 5.7, b) we notice that the peak positions slightly shift across the spectrum. This means that the diagonal features in the 2D map aren't exactly parallel to the main diagonal but are slightly shifted. We tentatively explain this observation as an effect of pulse chirp.

[3] The stochastic-stochastic quadrants encode the same information of a *full modulation* Pearson map. However, if the correlation signal is weak, it can be invisible to *full noise* configuration but visible with the *partial noise* one.

[4] We divide each point by the number of times the point has been summed.

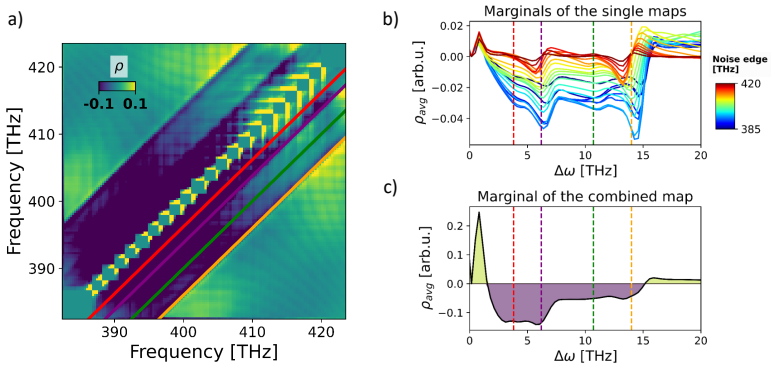

FIGURE 5.7: *moving noise configuration* on α-quartz. We display the 2D map in (a), the integrated curves of the single Pearson maps (b) and the integral of the combined *moving noise* map (c). The integrated curves are obtained by averaging the correlation signal of the correspondent 2D map along the main diagonal. The color scale of (b) indicates the value of the edge frequency between stochastic and coherent spectral regions. Colored lines mark the frequencies of the 3.8 (red), 6.2 (purple), 10.7 (green) and $14\,\mathrm{THz}$ (orange) phonons of α-quartz.

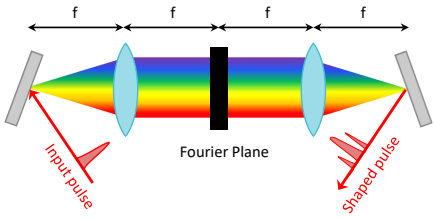

FIGURE 5.8: *4f line* scheme. By employing a diffraction grating in combination with a lens, all the spectral components are spatially separated into a diffraction limited spot at the Fourier plane. By placing a spatial mask in that position, it is possible to independently control the amplitude/phase of the different modes. Then, the shaped components are recombined with a second pair of lens+grating.

5.2 SLM pulse shaping

Stochastic fluctuations are a crucial ingredient for performing FCS experiments. In this Section, we present the methodology that we use to produce randomized light pulses, i.e. *ultrafast pulse shaping*.
In particular, we describe the working principles of a pulse shaper based on a *liquid crystal spatial light modulator* (LC-SLM or briefly SLM) that allows for the complete control of the amplitude and phase of the different spectral components [15, 16]. A pulse shaper based on a different technology is presented in Chapter 6.

4f-line

In general, *pulse shaping* indicates a broad class of techniques that enables to arbitrarily manipulate the electric field of an optical pulse. To achieve this task, most of the schemes operate in the frequency domain. In particular, a widely used pulse shaping scheme is the so-called *4f line* [16].
As depicted in Figure 5.8, a diffraction grating is used in combination with a lens to spatially separate the spectral components of the optical pulse and to focus them into a diffraction-limited spot on the *Fourier plane*. There, by placing a spatial mask, it is possible to manipulate independently each spectral component. Finally, a second pair of lens+diffraction grating is used to recombine the dispersed modes into a collimated pulse. Notably, all the optical elements are separated by the focal length f of the lens, hence the name *4f line*.

The choice of the spatial mask is crucial for determining the pulse shaping specifics. For example, static masks can be fabricated via lithography to obtain a well-defined spectrum profile. However, different shaping parameters require different spatial masks, making them not suitable for tunable pulse shapers.
An alternative is represented by dynamic masks [15], which are programmable and hence are fit for systems that require changes in the shaping parameters.

In particular, we designed a pulse shaper with high tunability that employs a spatial light modulator based on liquid crystals (SLM). An SLM is a matrix of pixels which consists in a layer of nematic crystals intertwined between a couple of electrodes (Figure 5.9). When no voltage is applied, the crystals orientation determines the maximal birefringence, i.e. the difference between the refractive index along the extraordinary (n_e) and ordinary (n_o) axis. By changing the voltage between the electrodes, it is possible to control the orientation of the liquid crystals and hence to modify $\Delta n = n_e - n_o$. This results in a phase delay ϕ

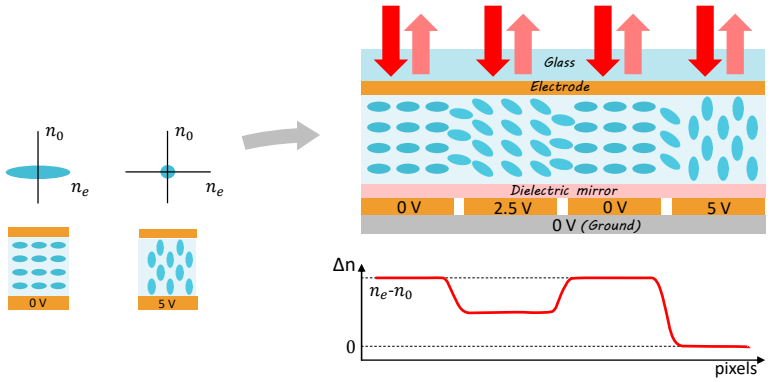

FIGURE 5.9: SLM working principle. By placing a layer of nematic liquid crystals in between two electrodes, it is possible to control their orientation and hence the birefringence of the layer $\Delta n = n_e - n_o$. Hence, the application of different voltages on different pixels determines a tunable Δn profile that causes a variable phase delay along the pixel axis. Adapted from [11].

that can be expressed as:

$$\phi(\omega, V) = \frac{\omega \Delta n(\omega, V) D}{c} \tag{5.3}$$

where ω is the frequency of the impinging light, V is the applied voltage, D is the thickness of the liquid crystals layer and c is the speed of light.

A different voltage can be applied at each pixel (see the side view of the SLM in Figure 5.9), creating a variable Δn profile along the pixel axis. As a consequence, light impinging on different regions of the SLM will experience different phase delays (equation 5.3).
We point out that the layer of liquid crystals isn't partitioned (like the electrodes) and therefore there will be i) no control on the inter-pixel regions (*pixelization*) and ii) a certain amount of correlation between neighbouring pixels.

2D pulse shaping

A single array of pixels, like the one presented in Figure 5.9, provides full tunability of the pulse spectral phase but has no direct control on the spectral amplitude. To recover the latter, a 2D mask has to be used in a diffraction geometry scheme [17].
Figure 5.10 shows the working principles of the diffraction geometry. A single pair of grating+lens is used both to disperse and to collimate the beams (*folded 4f line*). By properly tuning the pixel voltages, an effective blazed grating is generated along the vertical axis of the SLM (pink curve). Hence, each spectral component interacts with a specific grating associated to a pixel column of the SLM matrix and is diffracted. Then, the first order of diffraction of the different components is collected by the lens and recombined on the grating.
Importantly, the total control over the first-order diffracted beam can be achieved by changing the parameters of each blazed grating. To rationalize it, we first write the phase modulation described in Figure 5.10 (right) as:

$$\phi(\omega, y) = \alpha \left\{ \frac{1}{2} + A(\omega) S_d[\psi(\omega), y] \right\} \tag{5.4}$$

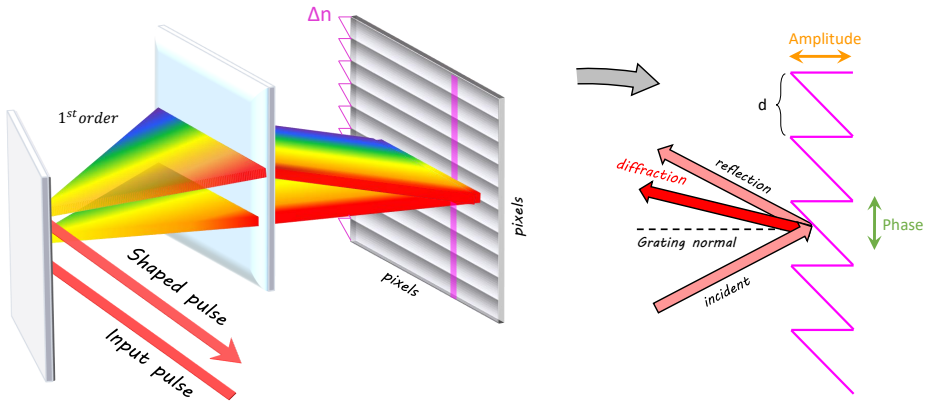

FIGURE 5.10: diffraction geometry scheme. By properly tuning the pixel voltages, an effective diffraction grating is created along the y-axis of the 2D SLM matrix. The full control over the first order of diffraction beam is achieved by changing independently the grating parameters for each spectral component (i.e. for each column of the matrix). Adapted from [11].

where S_d is a normalized sawtooth function with phase $\psi(\omega)$ and period d oriented along the y axis of the SLM matrix. The amplitude of the sawtooth is expressed by $A(\omega)$. Finally, α represents the maximum phase shift achievable with the the specific SLM used. Notably, $A(\omega)$ and $\psi(\omega)$ depend on the frequency because each column of the pixel matrix can be controlled independently (and hence the relative diffraction grating).
According to Fraunhofer diffraction [17], the first-order diffraction beam is:

$$E(\omega) \propto e^{-i\psi(\omega)} sinc[\pi - \frac{\alpha}{2} A(\omega)] \tag{5.5}$$

By looking at equation 5.5, it is clear that the 2D SLM provides full control over the first diffraction order. Indeed, the phase of the outcoming beam is linked to the spatial phase of the grating (i.e. the vertical position) while the amplitude is controlled by the efficiency of the blazed grating and scales as $sinc[A(\omega)]$.
Summarizing, by changing arbitrarily the grating parameters $A(\omega)$ and $\psi(\omega)$ along the frequency axis, it is possible to shape independently the spectral amplitude and phase of the different spectral components of the pulse.

Stochastic fluctuations

We implement the SLM-based pulse shaper by using a commercial 2D LC-SLM (Meadowlark Optics) with a programmable matrix of 1920x1152 pixels with a refresh rate of $\sim 200\,\mathrm{Hz}$.
In order to obtain spectrally uncorrelated pulses to be used in FCS experiments, we generate stochastic fluctuations through randomized SLM patterns. In details, we use an array of 1920 random numbers[5] with uniform distribution to randomly modulate the diffraction efficiency $A(\omega)$ of each spectral component and simulate the presence of stochastic noise[6]. As a result, each spectral component will have a random spectral amplitude.
Because of the intrinsic coupling between neighbouring pixels, we apply Gaussian-smoothing to the array of random values with uniform distribution. Hence, neighbouring pixels are no longer uncorrelated and a finite correlation length that depends on the FWHM of the

[5] Note that 1920 is the number of pixels along the SLM x-axis.
[6] Another approach consists in randomizing the phase of the diffraction grating. Further information can be found in [18].

smoothing function is introduced. This correlation length, that in our system is 5 *pxl* = 1 *nm*, determines the spectral resolution of the FCS experiment (together with the detector resolution).

In conclusion, we underline that the speed of a FCS experiment is determined by the refresh rate of the SLM ($200\,\mathrm{Hz}$) rather than by the pulsed laser source ($\leq 50\,\mathrm{kHz}$). Indeed, supposing to work at $5\,\mathrm{kHz}$, trains of >20 consecutive pulses will have the same stochastic profile and just one of them (or their average) could actually be used in the computation of the Pearson coefficient.
Furthermore, the time consumed for the generation+transmission of the SLM pattern ($\sim 8\,\mathrm{ms}$) must also be taken into account and, by adding it to refreshing time of the crystals ($\sim 5\,\mathrm{ms}$), the speed of the experiment is lowered to $\sim 70\,\mathrm{Hz}$[7].
The slow rate of SLM-based pulse shaping represents the major limitation of FCS experiments. A different pulse shaping scheme that could potentially boost the speed of FCS experiments to repetition rates $\leq 30\,\mathrm{kHz}$ is discussed in Chapter 6.

[7] The detection is synchronized with the SLM rate so that no replicas of the same stochastic pulse are measured.

5.3 FCS for the investigation of magnetic excitations

Femtosecond Covariance Spectroscopy is a technique that allows for the study of Raman signatures encoded in multimode correlations. As we will show in the next Section, the full potential of FCS is expressed in pump-probe experiments, where the technique provides simultaneous high temporal and frequency resolution that are otherwise unreached with time-resolved spontaneous Raman scattering experiments.
Nonetheless, FCS has proved to be a useful tool also for the investigation of equilibrium Raman features, as in the case of vibrational excitations [7, 18].
We underline that, in principle, the technique is sensitive to multimode correlations generated by Raman scattering whatever the specific nature of the elementary excitation is (magnetic, vibrational, electronic) but so far, FCS has been used just for the investigation of phonons.
In this Section we employ FCS for the study of a different type of low-energy excitations, i.e. magnons. In particular, we investigate if the technique is sensitive to magnetic excitations by measuring multimode correlations in the ferrimagnetic compound $RbNiF_3$.

As we discussed in Chapter 3, $RbNiF_3$ is a magnetic compound that is ferrimagnetic below $139\,\mathrm{K}$ and paramagnetic at higher temperatures. Moreover, the ferrimagnetic state is characterized by the presence of an intense 2-magnon excitation that experiences red-shift+broadening as temperature is increased and disappears at high temperatures (see Figure 3.2) [19].

To unveil the 2-magnon signature in photonic correlations, we arrange the setup as sketched in Figure 5.11 to perform a static FCS experiment. We use the laser+NOPA system to generate broadband coherent pulses with E_{pulse}=$1.78\,\mathrm{eV}$ $(430\,\mathrm{THz})$. Then we add stochastic fluctuations to the probe pulses with the pulse shaper described in Section 5.2. Finally, we collect the transmitted beam and we measure the frequency dispersed spectrum of the main and residual polarization with two arrays of photodiodes. In this way, we can evaluate both auto-correlation, i.e. the correlation evaluated between photons with the same polarization, and cross-correlation, i.e. the correlation between cross-polarized photons. The latter is actually the best configuration to isolate the 2-magnon mode [19].

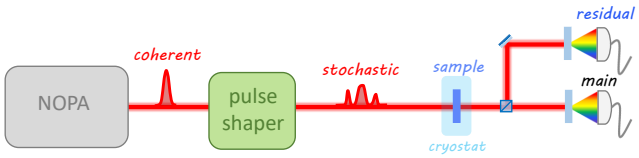

FIGURE 5.11: sketch of the experimental setup used for FCS static experiments.

As previously discussed, there are several noise configurations that we can adopt to perform a FCS experiment (see Figure 5.5). We choose to employ *partial noise modulation*, since it is the one that maximizes the visibility of the correlation signals [7]. However, there is an important evidence that we have to consider: $RbNiF_3$ is not a transparent medium in the visible range [20, 21]. Furthermore, low energy excitations are coupled to the optical absorption spectrum and hence do not have a uniform spectral response (see Chapter 3). For this reason, we use the new protocol of *moving noise configuration* to reconstruct the full spectral response of the material.

5.3.1 $RbNiF_3$

We now present the FCS measurements performed on $RbNiF_3$. We use the setup of Figure 5.11 to measure the cross-correlation signal when the incoming light is polarized orthogonal[8] to the $\hat{c}$ axis of the sample. The results for $E_{probe} \parallel \hat{c}$ are presented in Appendix A.

Figure 5.12 displays the moving noise maps obtained in the ferrimagnetic ($10\,\mathrm{K}$), paramagnetic state ($300\,\mathrm{K}$) and just above the transition temperature ($150\,\mathrm{K}$) of the sample. We first notice that the correlation signal isn't uniform along the diagonal, confirming the importance of performing a study of the whole spectral response. Moreover, the three maps are dominated by non-uniform signals (negative and positive bands) that we attribute to the correlation generated by absorption processes [22]. Since we're interested in temperature dependent correlation features (i.e. magnons), we look at the differential maps derived by subtracting the moving noise maps at different temperatures.

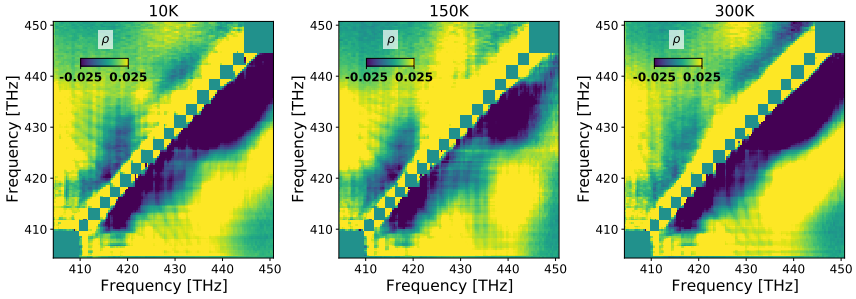

FIGURE 5.12: moving noise maps obtained by measuring a $RbNiF_3$ sample at three different temperatures that correspond to the ferrimagnetic ($10\,\mathrm{K}$), paramagnetic state ($300\,\mathrm{K}$) and to the state just above T_c ($150\,\mathrm{K}$). Measurements are performed with $E_{probe} \perp \hat{c}$.

In Figure 5.13 (a) we display the differential map obtained by subtracting the $10\,\mathrm{K}$ map, where we expect to have a 2-magnon contribution, and the $300\,\mathrm{K}$ one, where there should be no magnetic excitation. We mark with coloured lines the low energy excitations that we measured in Chapter 3. In particular, red line corresponds to the $2.9\,\mathrm{THz}$ phonon, purple line to the $8\,\mathrm{THz}$ one and orange line to the $14\,\mathrm{THz}$ 2-magnon excitation.
We measure two peaked correlation signals in correspondence of the 2.9 and of the $8\,\mathrm{THz}$ phonons[9]. Moreover, we unveil a strong correlation signal that results from a sign change right in correspondence of the two magnon excitation. Interestingly, the signal is localized at high frequencies. This spectral dependence is confirmed by the integrated curves of the single Pearson maps (Figure 5.13, b), where we see a clear sign change at $14\,\mathrm{THz}$ when the noise edge is shifted towards high frequency values (red,orange and yellow traces).
Remarkably, the signal region ($\geq 425\,\mathrm{THz}$) coincides with the energy range of the $3A_2 \rightarrow {}^1E^a$ *dd* transition [20, 21].
We measure a similar signal also in the case of $E_{probe} \parallel \hat{c}$ (see Appendix A).

We underline that, due to the strong spectral dependence of the correlation signal, integrated cuts of the whole moving noise map (Figure 5.13, c) are not representative of

[8] We recall that with this geometry the low energy excitations were more visible in the pump-probe maps (see Chapter 3).

[9] The evidence of a temperature-dependent signal in correspondence of the two phonons is consistent with the PP measurements performed in Chapter 3.

the measurement anymore, as they were in the case of α-quartz (Figure 5.7).

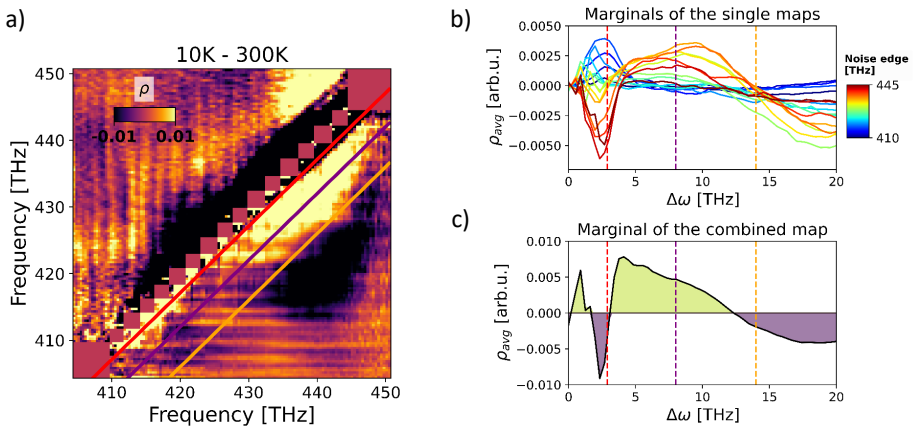

FIGURE 5.13: differential maps (a) with the respective single map (b) and combined (c) integrated curves obtained by subtracting the moving noise maps at $10\,\mathrm{K}$ and $300\,\mathrm{K}$ of Figure 5.12.

In Figure 5.14 we display the differential map obtained by subtracting the moving noise maps at $150\,\mathrm{K}$, where the 2-magnon excitation is expected to be broader and centered at $12\,\mathrm{THz}$, and $300\,\mathrm{K}$.
In this case, the signal isn't easy to interpret. We detect many correlation signals with a strong spectral dependence. Among them, there is a sign change at $12\,\mathrm{THz}$ in the [430-435 THz, 420-425 THz] regions of the map, that could be associated to the 2-magnon excitation.
However, it is not clear why a similar signal is present also in other regions of the differential maps but is centered at very different frequencies (see region [430-450 THz, 425-435 THz]).

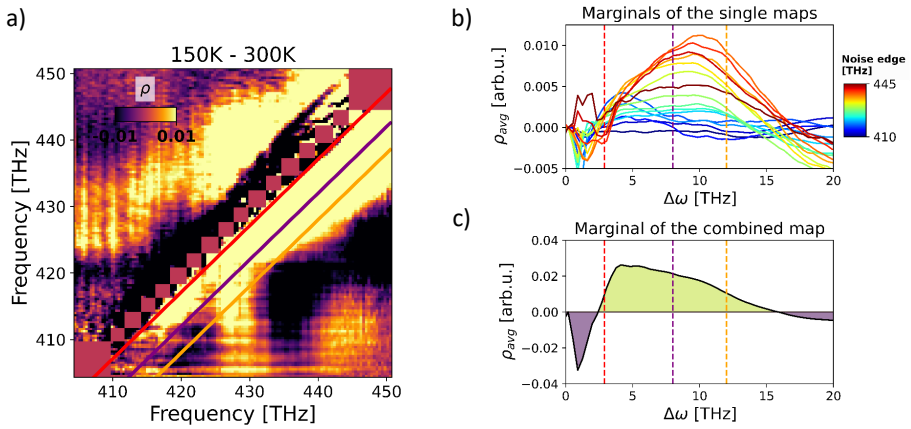

FIGURE 5.14: differential maps (a) with the respective single map (b) and combined (c) integrated curves obtained by subtracting the moving noise maps at $150\,\mathrm{K}$ and $300\,\mathrm{K}$ of Figure 5.12.

5.3.2 Discussion

The static FCS measurements on $RbNiF_3$ evidenced the presence of different correlation signals. First, we observed a dominant non-uniform signal at all temperatures for both the orthogonal ($E_{probe} \perp \hat{c}$) and the parallel ($E_{probe} \parallel \hat{c}$) configuration. Then, by comparing the cross-correlation maps acquired in the ferrimagnetic and paramagnetic state of the sample, we observed correlation features in correspondence of the $2.9/8\,\mathrm{THz}$ phonons and, notably, a big correlation signal centered at the 2-magnon frequency ($14\,\mathrm{THz}$). Also in this case, similar results were achieved by performing the experiment in the parallel and in the orthogonal geometry.

On the other side, the differential maps at intermediate temperatures ($150\,\mathrm{K}$) were more difficult to rationalize and it is not clear if a 2-magnon signal was present or not. In this framework, we just point out that the scattering intensity of the magnetic excitation is expected to be much weaker at the transition temperature with respect to the ferrimagnetic state [19]. Moreover, the magnetic excitation is also broader at higher temperatures and all together these two aspects could infer on the visibility of the correlation signal.

In conclusion, our first FCS experiment on a magnetic system showed promising indications that the technique is sensitive to magnon excitations. Nonetheless, the presented results are non-conclusive for two reasons. First, further studies at selected intermediate temperatures are required to properly unveil the temperature dependence of the correlation signal and see if it follows the magnon one[10] [19]. Secondly, we tried to wash out the absorption contribution to the correlation maps by subtracting the Pearson maps at different temperatures. However, this is just a rough approach that doesn't account for temperature changes of the absorption spectrum [21]. Therefore, a better understanding of correlation signals from non-transparent media is required to properly discriminate Raman and absorption features.

[10] From this perspective, we just mention that each *moving noise* map currently requires $\sim$ 7 hours of acquisition time. Therefore, a continuous temperature scan is not feasible at the moment.

5.4 Dynamic investigation of superconducting fluctuations

As we have previously discussed, Femtosecond Covariance Spectroscopy is a technique that studies Raman excitations through multimode photonic correlations. By employing stochastic pulses, FCS unveils signatures of *stimulated Raman scattering* processes that involve photons lying inside the pulse bandwidth.
Furthermore, FCS can be employed also for time-resolved studies [8]. Indeed, by implementing a pump-probe experiment where the probe is stochastic and is acquired with a single-shot detection, it is possible to measure the dynamic evolution of multimode correlations.

There is a crucial advantage in using pump-probe FCS with respect to time-resolved Raman experiments [23–25]: frequency and temporal resolution are fully decoupled. Indeed, the frequency resolution is dictated by the detection resolution and by the correlation length of the stochastic fluctuations (see Section 5.2) while the time-resolution is determined by the convolution of the pump and probe temporal profile[11].
Consequently, pump-probe FCS enables the possibility of performing a time-resolved Raman experiment following the sub-ps evolution of low-energy excitations with high frequency resolution ($\sigma < 1\,\mathrm{nm}$).

In this Section, we exploit the capabilities of pump-probe FCS to investigate the dynamics of B_{1g} and B_{2g} modes in $Bi_2Sr_2CaCu_2O_{8+\delta}$. After a short introduction, we present the experimental setup and the data analysis performed on the correlation maps. Finally, we discuss the measured correlation signal in the different phases of the sample.

5.4.1 Time-resolved Raman scattering in Cuprates

In Chapter 4 we discussed a specific Raman process, that is *electronic Raman scattering* from Cooper pairs in Cuprate superconductors. Indeed, we showed how it is possible to isolate the electronic excitations pertaining to different regions of the Brillouin zone (B_{1g} and B_{2g} modes) and we performed a full characterization of the related birefringence signal that arises in the superconducting state.
However, B_{1g}/B_{2g} modes can be directly accessed also with Raman spectroscopy [26]. In Figure 5.15 (a) we display the B_{1g} and B_{2g} spectra measured on two $Bi_2Sr_2CaCu_2O_{8+\delta}$ samples with a different level of doping [27]. Notably, the B_{1g} peak (solid line) is shifted at higher energies with respect to the B_{2g} mode. This was one of the first evidences that, together with the different scaling of the two curves at low frequencies (insets), suggested a $d_{x^2-y^2}$ symmetry of the superconducting gap in Cuprates [27, 28].

The investigation of the B_{1g}/B_{2g} dynamic response through Raman spectroscopy is particularly challenging due to the intrinsic limitations of the technique. In Raman experiments, high frequency resolution is achieved by employing quasi-monochromatic pulses that consequently have long temporal duration. Therefore, high frequency and temporal resolution can't be simultaneously accomplished and compromises must be made [23].
This happened also in the first dynamic study of the SC order parameter with time-resolved Raman spectroscopy (Figure 5.15, b) [29]. Saichu et al. measured the dynamic response

[11] The temporal profile of the stochastic probe pulse is the superposition of a ps-long tail [7, 18], resulting from the addition of randomized fluctuations, and of a short coherent component. The latter is responsible of the impulsive excitation and hence determines the temporal resolution of the experiment together with the pump duration.

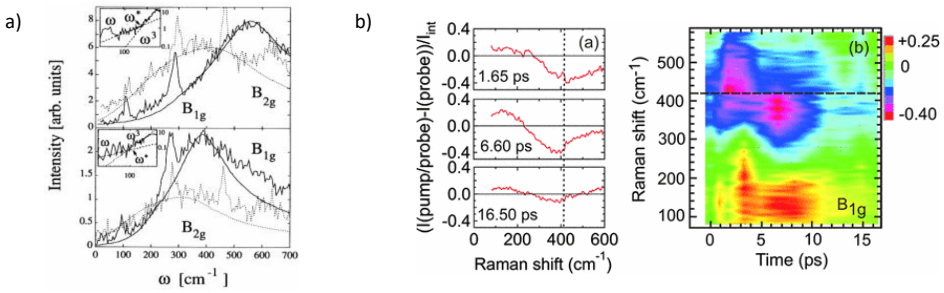

FIGURE 5.15: equilibrium Raman spectra (a) of the B_{1g} and B_{2g} modes of $Bi_2Sr_2CaCu_2O_{8+\delta}$ with different doping levels (top panel: $T_c = 86\,\mathrm{K}$, bottom panel: $T_c = 79\,\mathrm{K}$) [27]. In (b), we report a time-resolved Raman measurement of the B_{1g} mode from [29].

of the B_{1g} mode and unveiled a depletion of the pair-breaking peak (negative signal at $\sim 420\,\mathrm{cm}^{-1}$) accompanied by an increase of the quasi-particle spectral weight inside the gap (positive signal at low frequencies) that they associated to a loss of Cooper pairs caused by the pump action.
Importantly, the temporal resolution of the experiment was $\sim 0.9\,\mathrm{ps}$ and prevented the authors from investigating dynamics shorter than the ones characteristic of hole-phonon coupling.

5.4.2 Pump-probe FCS

To access the sub-ps dynamics of electronic excitations, we implement a pump-probe FCS experiment (Figure 5.16). In details, we investigate an OP $Bi_2Sr_2CaCu_2O_{8+\delta}$ sample ($T_c = 90\,\mathrm{K}$) by employing a low-energy MIR pump pulse ($10\,\mu\mathrm{m}$, $\phi_{pump} = 1.5\,\mathrm{mJ\,cm}^{-2}$) and by measuring both the main ($\parallel$) and the residual polarization ($\perp$) of the scattered probe light. By properly aligning the polarization of the incoming probe beam with the CuO/CuCu axis, we conveniently isolate the B_{1g}/B_{2g} modes [30].
To maximize the visibility of the correlation signal, the experiment is performed with *partial noise modulation*.

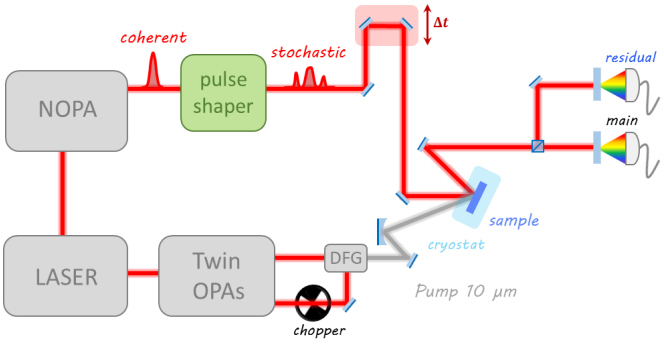

FIGURE 5.16: sketch of the experimental setup used to perform pump-probe FCS.

When we perform a pump-probe FCS experiment, for a fixed pulses delay, we acquire a pair of Pearson maps: one in the presence (*pumped*) and one in the absence (*unpumped*) of the pump. Specifically to isolate the B_{1g}/B_{2g} modes, we measure a pair of cross-correlators between the main and the residual probe polarization (Figure 5.17).

Secondly, we subtract the two Pearson maps (pumped-unpumped) and integrate the differential correlation[12] maps along the diagonal. Notably, if the experiment is performed with *partial noise modulation*, only mixed quadrants have to be considered (Figure 5.17, b).
Finally, we combine all the integrated traces (Figure 5.17, c) obtained at different time delays in a *dynamic FCS map*, where the differential correlation signal is displayed as a function of the frequency shift from the main diagonal and of the pump-probe delay (Figure 5.17, d).

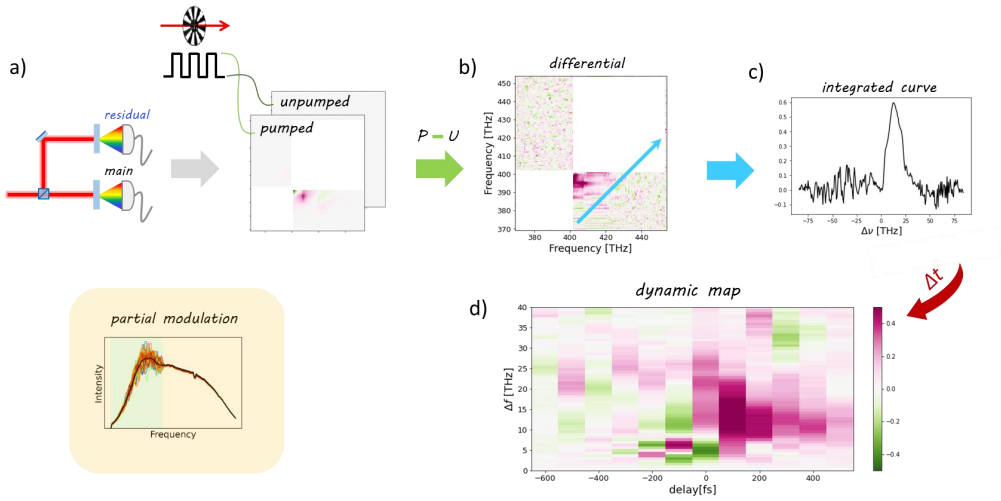

FIGURE 5.17: *dynamic FCS map.* We measure the cross-correlation (*main* vs *residual* polarization) maps for both the *pumped* and the *unpumped* data (a). The differential maps (b) are then integrated along the diagonals. We obtain an integrated trace (c) for each pump-probe delay Δt. We assemble them in a dynamic map (d) where the correlation signal is a function of the frequency shift from the main diagonal Δf and of the pulses delay Δt. When the pump-probe FCS experiment is performed with *partial noise modulation*, only the mixed quadrants have to be considered.

Normal Phase

We start our investigation of the dynamic correlation signal from the normal phase of $Bi_2Sr_2CaCu_2O_{8+\delta}$ (T=300 K). In Figure 5.18 we display the two dynamic maps obtained in the two different geometries.
Both maps are dominated by experimental noise and no clear correlation signal emerges neither at zero nor at positive time delays.

SC state

By cooling down the temperature of the sample (T=38 K), we measure the dynamic response in the superconducting state (Figure 5.19). Remarkably, a dynamic signal appears in correspondence of the temporal overlap and evolves at positive times decaying on a ps time scale.

[12] Each differential map is the result of a 60.000 pulses acquisition.

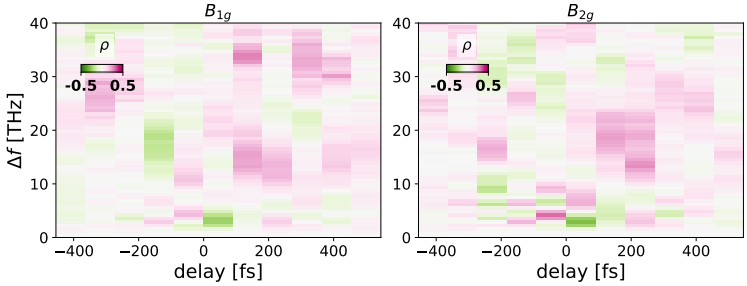

FIGURE 5.18: dynamic FCS maps measured in the *normal phase* of the sample.

We study the spectral dependence of the positive correlation signal of the B_{1g} and B_{2g} modes by integrating the dynamic maps (Figure 5.19, a) in the overlap region (0-$200\,\mathrm{fs}$). The resulting spectra are displayed in Figure 5.19 (b). Notably, the correlation signal associated to the B_{1g} mode is shifted at higher energies with respect to the B_{2g} one, as highlighted by the first-order momenta of the two curves (vertical lines).
We point out that this result is consistent with spontaneous electronic Raman scattering experiments (Figure 5.15) [27].

In Figure 5.19 (c) we present the temporal dependence of the correlation signal by displaying the horizontal cuts of the dynamic maps integrated in the 0-$20\,\mathrm{THz}$ frequency range.
In both configurations, the decaying signal can't be fitted with a single exponential curve. Instead, the fast and the slow dynamics are well described by a double exponential function convoluted with a gaussian that accounts for the pulse temporal duration.
No clear differences emerge among the B_{1g} and B_{2g} geometries.

Finally, we report an interesting asymmetry of the experiment. The dynamic maps that unveil the presence of superconducting correlations (Figure 5.19, a) have been acquired by using *partial noise modulation*, and specifically by adding stochastic fluctuations to the low energy side of the pulse (see Figure 5.17). Remarkably, if the shaping is reversed and stochastic noise is added to the high energy side of the spectrum, correlation signal disappears (Appendix B).
This evidence matches the results reported in Chapter 4, where we unveiled a superconducting birefringence signal localized on the low-energy region of the pulse spectrum.

PG phase

Figure 5.20 shows the dynamic maps measured when the sample is in the pseudogap phase (T=$110\,\mathrm{K}$). Remarkably, a positive correlation signal is measured in the dynamic maps for both the B_{1g} and B_{2g} configurations (Figure 5.20, a).
The spectral dependence of the time-integrated (0-$200\,\mathrm{fs}$) maps (Figure 5.20, b) presents a smaller frequency shift of the first-order momenta with respect to the ones measured in the SC state.
Furthermore, the temporal dynamics of the frequency-integrated (0-$20\,\mathrm{THz}$) maps (Figure 5.20, c) are still described by a double exponential decay. However, there is a difference between the B_{1g} and B_{2g} curves, where the latter is characterized by a slower decay.

We highlight that this result differs fundamentally from spontaneous Raman scattering measurements, where no signal is measured above T_c [26].

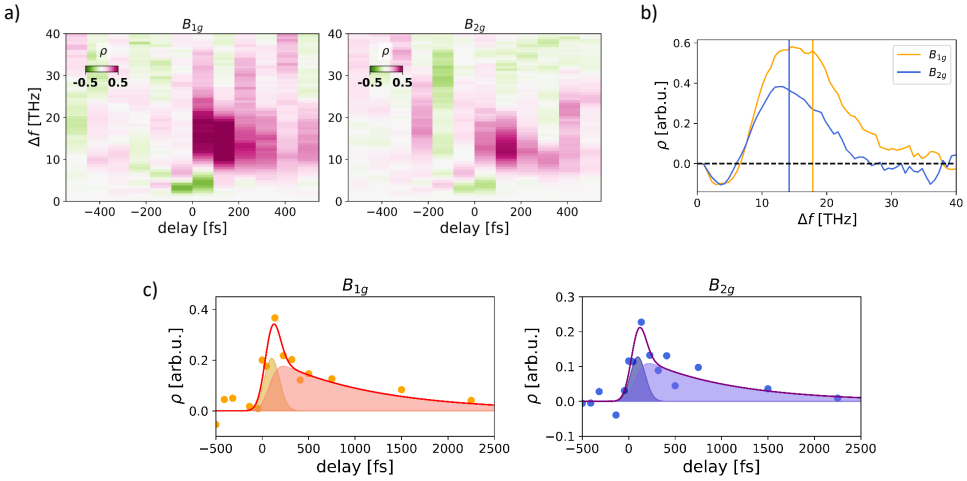

FIGURE 5.19: dynamic maps (a) of the B_{1g} and B_{2g} correlation signals acquired in the SC state (T=38 K). In (b) and (c) we display the time (0-200 fs) and frequency integrated (0-20 THz) cuts of the dynamic maps.

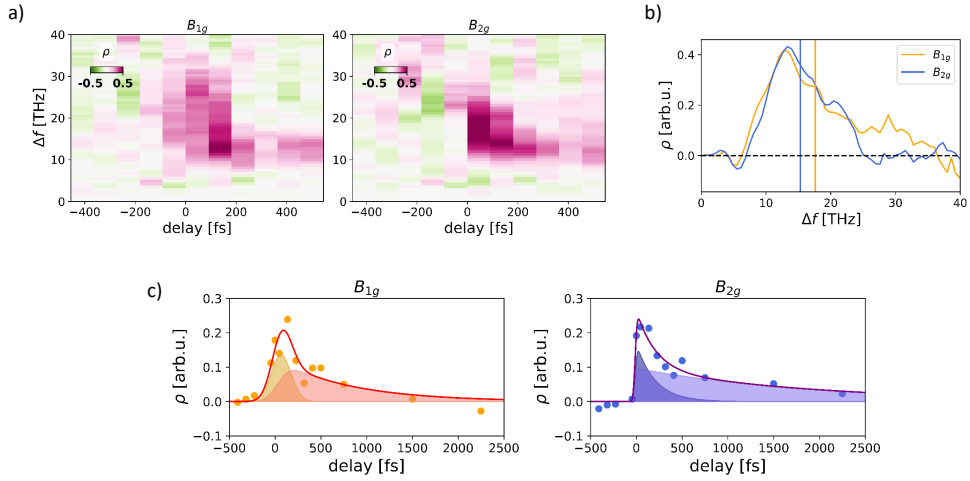

FIGURE 5.20: dynamic maps measured in the PG phase (a) with the relative time-integrated (0-200 fs, b) and frequency-integrated (0-20 THz, c) traces.

5.4.3 Discussion

Summarizing the results of the previous Section, we observed a superconducting correlation signal that resembles some characteristic features of electronic B_{1g} and B_{2g} modes, e.g. the frequency dependence. Moreover, we unveiled a qualitatively similar signal also in the pseudogap phase, where spontaneous Raman scattering doesn't track any signal. Finally, no signal was measured in the normal state of the sample.

In order to discuss these results, we first point out two crucial differences between our experiment and a standard measurement of Raman spectroscopy:

- pump-probe FCS is an *impulsive* technique, where the excitation and the heterodyne detection of the signal field are performed by ultrashort pulses. Oppositely, spontaneous Raman scattering experiments are time-integrated measurements.
- the intrinsic broad bandwidth of ultrashort pulses determines the *stimulated* nature of the Raman process, where 2 fields simultaneously interact to generate a phase-locked excitation. On the contrary, in spontaneous Raman scattering excitation is generated by an off-resonance photon and no phase relation is preserved.

The direct consequence is that pump-probe FCS measures *coherent* signals, while spontaneous electronic Raman scattering probes *incoherent* excitations.

From this perspective, the presence of a superconducting-like signal in the PG phase may be an indication of local pairing above T_c.
The persistence of superconducting fluctuations above the critical temperature has been reported in many works [31–36]. These results highlighted that the opening of a gap and long-range phase coherence are two distinct requirements that must be simultaneously fulfilled to generate a SC state. When coherence among Cooper pairs is broken, the macroscopic superconducting state is melted even if local pairing is still present [37].

At this point, we underline that such pairing is invisible to standard spontaneous Raman scattering, since the incoherent signal is integrated over a multitude of Cooper pairs with random phases. Oppositely, the coherent nature of pump-probe FCS may be a key feature to overcome the macroscopic incoherence and to probe local pairing with its relative dynamics.

However, even if our results are reproducible, they represent just an exploratory study and stronger claims require a richer dataset of dynamic FCS maps collected at different temperatures and on samples with different levels of doping.
This puts the focus on the biggest limitation of pump-probe FCS, that is the slowness of the acquisition times. As we reported in Section 5.2, the speed of the technique is limited by the generation of the stochastic pulses that, with SLM-based pulse shaping, works at $\sim 60\,\mathrm{Hz}$. Consequently, the measurement of a single dynamic map becomes a ~ 6 hours long process, making continuous temperature scans unfeasible.

For this reason, we're currently working on different pulse shaping designs that could provide a fast generation of stochastic pulses and hence boost the speed of the technique. This direction is explored in the next Chapter, where we present a novel pulse shaper based on an acousto-optic crystal that ideally works up to $30\,\mathrm{kHz}$.

Appendices

A FCS on $RbNiF_3$: parallel configuration

In this section, we present a FCS static experiment on $RbNiF_3$ similar to the one presented in Chapter 5 where the impinging probe is set parallel to the $\hat{c}$ axis of the sample and correlation is evaluated between the main and the residual polarization components.
Figure A.1 shows the correlation maps obtained with the *moving noise configuration* in the ferrimagnetic $(10\,\mathrm{K})$ and paramagnetic state $(300\,\mathrm{K})$ of the sample. As in the case of orthogonal geometry (see Figure 5.12), it is difficult to distinguish the differences of the two maps. Therefore, we subtract them in order to highlight the temperature dependent features.
Figure A.2 displays the differential map. As in the case of $E_{probe} \perp \hat{c}$, we identify a clear sign change at $14\,\mathrm{THz}$ in the high frequency region of the map (Figure A.2, a) and in the correspondent averaged cuts (Figure A.2 (b), red and orange curves).
We address this correlation feature two the 2-magnon excitation characteristic of the ferrimagnetic phase of $RbNiF_3$ [19].

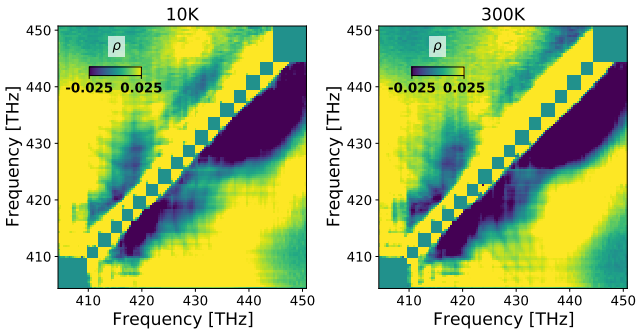

FIGURE A.1: *moving noise* maps obtained by measuring the ferrimagnetic $(10\,\mathrm{K})$ and paramagnetic phase $(300\,\mathrm{K})$ of $RbNiF_3$ with $E_{probe} \parallel \hat{c}$.

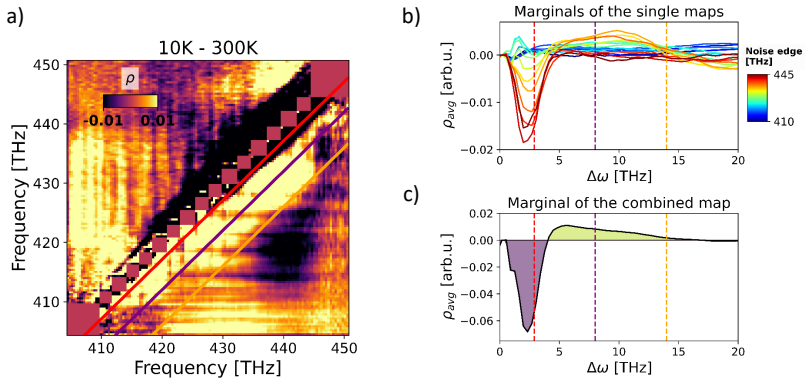

FIGURE A.2: differential map (a) obtained by subtracting the $10\,\mathrm{K}$ and $300\,\mathrm{K}$ maps of Figure A.1. The correspondent marginals obtained by averaging along the diagonal the single differential *partial noise* maps or the final *moving noise* one are displayed in (b) and (c), respectively. In (b), the color scale indicates the edge frequency between the stochastic and the coherent region of the pulse spectrum.

B FCS on $BSCCO$: high-energy stochasticity

In this Appendix we present the same dynamic maps showed in Chapter 5 for the pump-probe FCS experiment on BSCCO (OP, T_c=90 K) measured by inverting the *partial noise modulation*, i.e. by adding stochastic fluctuations on the high energy side of the pulse.
Figure B.1 displays the resulting dynamic maps obtained in the SC state of the sample. Remarkably, no superconducting signal is measured.
We underline that the evidence of a superconducting signal localized on the low-energy side of the probe pulse emerged also in birefringence measurements of Chapter 4, further enforcing the link between FCS signal and B_{1g}/B_{2g} modes.

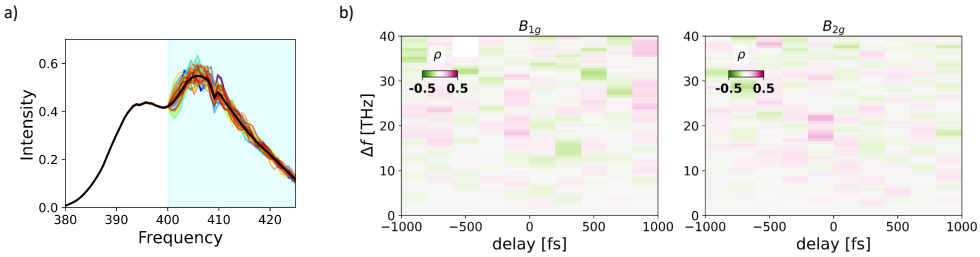

FIGURE B.1: spectrum (a) and dynamic maps (b) obtained by performing a pump-probe FCS experiment on BSCCO in the superconducting phase.

References

[1] Kurt Wiesenfeld and Frank Moss. "Stochastic resonance and the benefits of noise: from ice ages to crayfish and SQUIDs". In: *Nature* 373.6509 (1995), pp. 33–36.

[2] Luca Gammaitoni et al. "Stochastic resonance". In: *Reviews of modern physics* 70.1 (1998), p. 223.

[3] John K Douglass et al. "Noise enhancement of information transfer in crayfish mechanoreceptors by stochastic resonance". In: *Nature* 365.6444 (1993), pp. 337–340.

[4] James J Collins, Thomas T Imhoff, and Peter Grigg. "Noise-enhanced tactile sensation." In: *Nature* (1996).

[5] Martina Esposito et al. "Photon number statistics uncover the fluctuations in non-equilibrium lattice dynamics". In: *Nature communications* 6.1 (2015), p. 10249.

[6] Francesco Randi et al. "Probing the fluctuations of optical properties in time-resolved spectroscopy". In: *Physical Review Letters* 119.18 (2017), p. 187403.

[7] Jonathan Owen Tollerud et al. "Femtosecond covariance spectroscopy". In: *Proceedings of the National Academy of Sciences* 116.12 (2019), pp. 5383–5386.

[8] Giorgia Sparapassi et al. "Transient measurement of phononic states with covariance-based stochastic spectroscopy". In: *Light: Science & Applications* 11.1 (2022), p. 44.

[9] Xiaoji G Xu et al. "Noise autocorrelation spectroscopy with coherent Raman scattering". In: *Nature Physics* 4.2 (2008), pp. 125–129.

[10] LJ Frasinski, K Codling, and PA Hatherly. "Covariance mapping: A correlation method applied to multiphoton multiple ionization". In: *Science* 246.4933 (1989), pp. 1029–1031.

[11] Angela Montanaro. "Non-equilibrium response of quantum materials to resonant low-energy electronic photo-excitations". PhD thesis. University of Trieste, 2022.

[12] Yong-Xin Yan, Edward B Gamble Jr, and Keith A Nelson. "Impulsive stimulated scattering: General importance in femtosecond laser pulse interactions with matter, and spectroscopic applications". In: *The Journal of chemical physics* 83.11 (1985), pp. 5391–5399.

[13] Eric Olaf Potma and Shaul Mukamel. "Theory of coherent Raman scattering". In: *Coherent Raman Scattering Microscopy* (2012), pp. 3–42.

[14] Filippo Glerean et al. "Quantum model for impulsive stimulated Raman scattering". In: *Journal of Physics B: Atomic, Molecular and Optical Physics* 52.14 (2019), p. 145502.

[15] Andrew M Weiner. "Femtosecond pulse shaping using spatial light modulators". In: *Review of scientific instruments* 71.5 (2000), pp. 1929–1960.

[16] Antoine Monmayrant, Sébastien Weber, and Béatrice Chatel. "A newcomer's guide to ultrashort pulse shaping and characterization". In: *Journal of Physics B: Atomic, Molecular and Optical Physics* 43.10 (2010), p. 103001.

[17] Joshua C Vaughan et al. "Diffraction-based femtosecond pulse shaping with a two-dimensional spatial light modulator". In: *Optics letters* 30.3 (2005), pp. 323–325.

[18] Giorgia Sparapassi. "Femtosecond Covariance Spectroscopy". PhD thesis. University of Trieste, 2019.

[19] SR Chinn, HJ Zeiger, and JR O'Connor. "Two-Magnon Raman Scattering and Exchange Interactions in Antiferromagnetic KNi F 3 and K 2 Ni F 4 and Ferrimagnetic RbNi F 3". In: *Physical Review B* 3.5 (1971), p. 1709.

[20] G Zanmarchi and PF Bongers. "Magnon sidebands in the optical spectrum of RbNiF3". In: *Solid State Communications* 6.1 (1968), pp. 27–31.

[21] RV Pisarev et al. "Magneto-optical study of the 3A2 to 1Ea transition in magnetic crystals KNiF3, Rb2NiF4d4, K3Ni2F7, RbNiF3". In: *Journal of Physics C: Solid State Physics* 7.22 (1974), p. 4143.

[22] Dario De Angelis et al. "Free electron laser stochastic spectroscopy revealing silicon bond softening dynamics". In: *Physical Review B* 107.21 (2023), p. 214305.

[23] Daniele Fausti and Paul HM van Loosdrecht. "Time resolved Raman scattering". In: *Optical Techniques for Solid-State Materials Characterization* (2011).

[24] Daniele Fausti, Oleg V Misochko, and Paul HM van Loosdrecht. "Ultrafast photoinduced structure phase transition in antimony single crystals". In: *Physical Review B* 80.16 (2009), p. 161207.

[25] Makoto Nakajima et al. "Time-resolved Raman spectroscopy applied to the photoinduced phenomena in NaV2O5". In: *Journal of Physics: Conference Series*. Vol. 21. 1. IOP Publishing. 2005, p. 201.

[26] Thomas P Devereaux and Rudi Hackl. "Inelastic light scattering from correlated electrons". In: *Reviews of modern physics* 79.1 (2007), p. 175.

[27] TP Devereaux. "Theory of electronic Raman scattering in disordered unconventional superconductors". In: *Physical review letters* 74.21 (1995), p. 4313.

[28] TP Devereaux et al. "Electronic Raman scattering in high-T c superconductors: A probe of d x 2-y 2 pairing". In: *Physical review letters* 72.3 (1994), p. 396.

[29] RP Saichu et al. "Two-component dynamics of the order parameter of high temperature Bi 2 Sr 2 CaCu 2 O 8+ δ superconductors revealed by time-resolved Raman scattering". In: *Physical review letters* 102.17 (2009), p. 177004.

[30] Francesca Giusti et al. "Anisotropic time-domain electronic response in cuprates driven by midinfrared pulses". In: *Physical Review B* 104.12 (2021), p. 125121.

[31] John Corson et al. "Vanishing of phase coherence in underdoped Bi2Sr2CaCu2O8+ δ". In: *Nature* 398.6724 (1999), pp. 221–223.

[32] Jhinhwan Lee et al. "Spectroscopic fingerprint of phase-incoherent superconductivity in the underdoped Bi2Sr2CaCu2O8+ δ". In: *Science* 325.5944 (2009), pp. 1099–1103.

[33] LS Bilbro et al. "Temporal correlations of superconductivity above the transition temperature in La2- x Sr x CuO4 probed by terahertz spectroscopy". In: *Nature Physics* 7.4 (2011), pp. 298–302.

[34] Ivan Madan et al. "Separating pairing from quantum phase coherence dynamics above the superconducting transition by femtosecond spectroscopy". In: *Scientific reports* 4.1 (2014), p. 5656.

[35] Edoardo Baldini et al. "Clocking the onset of bilayer coherence in a high-T C cuprate". In: *Physical Review B* 95.2 (2017), p. 024501.

[36] A. von Hoegen et al. "Amplification of Superconducting Fluctuations in Driven $YBa_2Cu_3O_{6+x}$". In: *Phys. Rev. X* 12 (3 July 2022), p. 031008. DOI: 10.1103/PhysRevX.12.031008. URL: https://link.aps.org/doi/10.1103/PhysRevX.12.031008.

[37] F Boschini et al. "Collapse of superconductivity in cuprates via ultrafast quenching of phase coherence". In: *Nature materials* 17.5 (2018), pp. 416–420.

Chapter 6
Acousto-optic pulse shaping for fast FCS experiments

Abstract

Ultrafast pulse shaping is traditionally performed by inserting liquid-crystal devices (SLM) or acousto-optic modulators (AOM) in the Fourier plane of zero-dispersion *4f lines*, where the spatially-separated spectral components are manipulated independently. However there are several issues that emerge when using these kind of devices. First, the pixelation generates pre- and post- pulses that can contain a relevant fraction of the total pulse energy. Then, a change in the central wavelength of the pulse determines a realignment of the pulse shaper, thus precluding an easy tunability of the system. Finally, the slow refresh rate of the nematic crystals ($\ll 1\,\mathrm{kHz}$) can be a big limitation in some applications, like in the case of *Femtosecond Covariance Spectroscopy* (FCS).

In this Chapter we present an alternative pulse shaping scheme that overcomes all of the aforementioned issues by employing a commercial acousto-optic programmable dispersive filter, the *dazzler* (Fastlite). In particular, we propose a novel design of a customized *dazzler* that can generate stochastic pulses at repetition rates $\leq 30\,\mathrm{kHz}$ and hence paves the way for fast FCS experiments.
After introducing the basic principles of pulse shaping with acousto-optic crystals, we present the design of the customized dazzler that we developed in collaboration with the R&D department of Fastlite to generate stochastic pulses. Subsequently, we perform some preliminary tests on the dazzler-based pulse shaper to understand the feasibility of fast FCS experiments that rely on this pulse shaping scheme.

6.1 Acousto-Optic interaction and Pulse Shaping

Acousto-optic effects arise from the interaction between optical and sound waves that takes place in a medium. In details, when ultrasonic waves propagate through a medium, the strain associated to their propagation induces a periodic change of the refractive index. The perturbed acousto-optic medium is equivalent to a dislocation grating and when an optical wave impinges on it, diffraction occurs.

In 1974 *Chang et al.* proposed a first design of a non-collinear acousto-optic tunable filter [1] that laid the foundations for the development of acousto-optic devices [2]. Nowadays, the applications of acousto-optic devices span a wide range of fields, that go from the development of spectrometers used for lunar exploration [3] to the imaging of food-borne bacteria [4] or environmental monitoring [5].

Moreover, acousto-optic interaction can be used to design pulse-shapers that don't account on conventional spatial-light modulators with liquid crystals technology [6]. Indeed, by exploiting acousto-optic interaction in a birefringent medium, it is possible to generate an optical signal that resembles an original acoustic wave [7]. Therefore, by manipulating the incoming acoustic wave, it is possible to control the spectral profile of the optical pulse [8–10] and obtain a pulse shaper that operates in a broad energy range that goes from the ultraviolet [11] to the mid-IR [12].

This novel pulse shaper is realized in the so-called *acousto-optic programmable dispersive filter* (AOPDF). In AOPDF the pulse shaping mechanism arises from a copropagative interaction between a polychromatic acoustic wave and a broadband optical pulse in a birefringent acousto-optic crystal. When phase-matching conditions are fulfilled, the two beams interact constructively and give rise to a new optical beam, which is referred to as the diffracted beam.

6.1.1 Phase matching conditions

We depict the pulse shaping process as a three-wave mixing process, where the incoming optical beam interacts with the acoustic wave to generate the diffracted beam. This process obeys to the general phase-matching conditions, that are described by the energy and the momentum conservation laws:

$$\begin{aligned} \omega_{in} + \omega_{ac} &= \omega_{diff} \\ \vec{k}_{in}(\omega_{in}) + \vec{k}_{ac}(\omega_{ac}) &= \vec{k}_{diff}(\omega_{diff}) \end{aligned} \tag{6.1}$$

where $(\vec{k}_{in}, \omega_{in})$, $(\vec{k}_{diff}, \omega_{diff})$ and $(\vec{k}_{ac}, \omega_{ac})$ indicate the wave-vectors and the angular frequencies of the incoming optical beam, of the diffracted one and of the acoustic wave.

For standard AOPDFs based on TeO_2, the incoming beam is usually polarized along the ordinary axis of the crystal, the acoustic wave is a shear wave and the diffracted beam is polarized parallel to the extraordinary axis.

Since the velocity of sound in the crystal is much lower than the velocity of light, the acoustic frequency is negligible with respect to the one of the optical beam ($\omega_{ac} \ll \omega_{in}$)

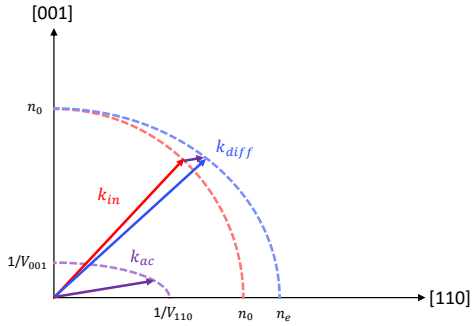

FIGURE 6.1: Phase matching conditions of the acoustic, incoming and diffracted optical beams in a TeO_2 crystal. Adapted from [9].

and equation 6.1 becomes

$$\vec{k}_{in}(\omega_{in}) + \vec{k}_{ac}(\omega_{ac}) = \vec{k}_{diff}(\omega_{in}) \tag{6.2}$$

In Figure 6.1 we display a typical example of fulfillment of the phase-matching conditions in a birefringent crystal. In particular, we point out that the acousto-optic interaction is not collinear in terms of wavevectors.
Moreover, for a fixed propagation direction of the acoustic and the incoming optical wave, we can look at eq. 6.2 as an implicit equation that links acoustic and optical frequencies. In thick crystals, this link is an almost one-to-one relationship between the optical and the acoustic spectral components, i.e. a single acoustic frequency diffracts a single optical frequency.

6.1.2 Poynting vector

In most of the acousto-optic modulators, the Poynting vector of the incoming optical beam is perpendicular to the acoustic one under phase-matching conditions.
On the contrary, input optical and acoustic Poynting vectors are collinear in the case of AOPDF. Indeed, the longitudinal interaction maximizes the interaction length and gives rise to the quasi-bijective relationship between acoustic and optical frequencies:

$$\omega_{ac}/\omega_{opt} = \alpha(\omega) \tag{6.3}$$

where α weakly depends on ω and is determined by the birefringence of the crystal and by the specific phase-matching geometry.
Notably, α values are typically very small (e.g. $\alpha \sim 2.3 \cdot 10^{-7}$ in commercial *dazzler*). This enables the control of optical signals in the hundreds of THz range with electrical signals in the tens of MHz regime.

6.1.3 Acousto-Optic Pulse Shaping

In the following, we describe the acousti-optic pulse shaping working principles. We propose a non-rigorous picture based on *group delay* arguments that gives a direct insight of the mechanism. We report the correct *time convolution* approach, which is practical for computation but less self explanatory, in Appendix A.

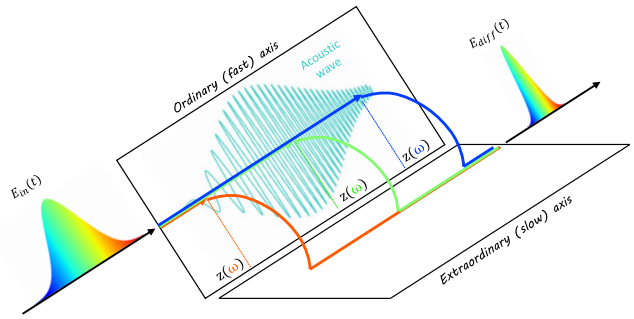

FIGURE 6.2: working principle of acousto-optic pulse shaping in terms of group delay control. Adapted from [13].

A schematic representation of the AOPDF working principle is shown in Figure 6.2. A time-dependent radio-frequency (RF) signal excites a transducer that converts the electric signal in an acoustic wave. The acoustic wave travels along the z direction with velocity V and reproduces the spatial and temporal profile of the original RF signal.

Let's assume that the acoustic wave has a linear chirp and hence that at each position z of the crystal there is a single spatial frequency ω of the acoustic wave ($z \rightarrow z(\omega)$). Each spectral component of the incident optical pulse (polarized along the ordinary axis of the crystal) travels a certain distance before it encounters the correspondent phase-matched spatial frequency of the acoustic grating. At this specific position, three-wave mixing process takes place and generates a component of the diffracted wave polarized along the extraordinary axis.
The same process will occur for different frequencies at different $z(\omega)$ positions and, at the crystal output, the diffracted pulse will consists in all the spectral components that have been diffracted at different z positions.

Importantly, pulse shaping is achieved by controlling the group delay and the amplitude of each spectral component of the diffracted beam. In details:

- since ordinary and extraordinary polarizations travel with different group velocities, each frequency will experience a different group delay. In particular, the group delay of the diffracted pulse is given by [7]

$$\tau(\omega) = \frac{n_{g_o}(\omega)}{c} z(\omega) + \frac{n_{g_e}(\omega)}{c} (L - z(\omega)) \tag{6.4}$$

  where n_{g_o} and n_{g_e} represent the ordinary/extraordinary group indexes[1] and L is the crystal length. Hence, by controlling for each frequency the position $z(\omega)$ where diffraction occurs, it is possible to control the pulse group delay $\tau(\omega)$.

- the spectral amplitude of the diffracted beam is manipulated by controlling the acoustic power at all $z(\omega)$.

[1] We recall that the group index is defined as $n_g = \frac{c}{v_g} = c\frac{\partial k}{\partial \omega}$.

FIGURE 6.3: commercial TeO_2-based AOPDF (*dazzler*, Fastlite).

6.2 Customized Dazzler for stochastic pulses

Acousto-Optic Programmable Dispersive Filters (AOPDF) represent a valid alternative to Spatial Light Modulator (SLM) systems for pulse shaping. Remarkably, they can overcome important issues intrinsic in liquid crystal systems, like *pixelization*, poor wavelength tunability and slow refresh-rate ($< 100\,\mathrm{Hz}$) [10]. In particular, the impossibility of working at high-repetition rates is detrimental for some applications of SLM-based pulse shapers, e.g. *Femtosecond Covariance Spectroscopy*.
In this section, we propose a novel pulse-shaper design that exploits a commercial AOPDF (*dazzler*, Fastlite) to generate stochastic pulses at repetition rates $\leq 30\,\mathrm{kHz}$ and possibly represents the first step for the realization of *fast FCS* experiments.

Dazzler is a commercial Acousto-Optic programmable filter produced by Fastlite (see Figure 6.3). It consists in a TeO_2 prismatic crystal connected to a Radio-Frequency (RF) generator.
By converting the RF signal into an acoustic wave with a transducer, the system exploits acousto-optic interaction to modulate the amplitude and the spectral phase of an incoming optical pulse.
In details, the system is synchronized with the laser source to generate an acoustic wave when the input optical pulse impinges on the acousto-optic crystal. Importantly, the incoming polarization must be parallel to the vertical axis of the crystal (see Figure 6.4).
At the output of the crystal, two beams are generated: the transmitted[2] and the diffracted beam. In particular, the diffracted pulse, which has in-plane polarization (Figure 6.4), will have a modulated spectrum according to the specific profile of the acoustic wave.

Dazzler can manipulate optical pulses in the $650\text{-}1100\,\mathrm{nm}$ range[3] with a resolution of $\sim 0.2\,\mathrm{nm}$. Moreover, there are two operational modes of the device that concern the generation of the acoustic waves:

- In *continuous mode*, a single acoustic wave is repeatedly sent to the acoustic crystal, keeping the profile of the acoustic wave fixed throughout the whole set of pulses. This mode is commonly used for static corrections (e.g. temporal chirp) and works up to $30\,\mathrm{kHz}$[4].

[2] Notably, the transmitted beam isn't parallel to the incoming input beam but propagates along a different direction. This happens because the crystal is prismatic, i.e. the input and output faces aren't cut parallel.

[3] Specifications of the UHR $650\text{-}1100$ *dazzler* model.

[4] In *continuous mode*, the maximum repetition rate is limited by the travelling time of the acoustic wave throughout the crystal ($\sim 30\,\mu\mathrm{s}$).

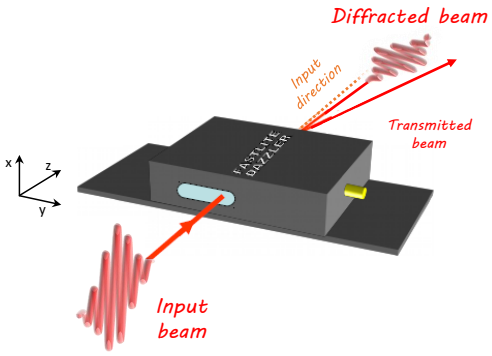

FIGURE 6.4: when light with vertical polarization impinges on a dazzler device, a diffraction beam with in-plane polarization is produced. Remarkably, the transmitted beam doesn't propagate along the input direction since the crystal is prismatic.

- The *streaming mode* allows for the independent shaping of consecutive pulses by refreshing the profile of the acoustic wave at each pulse. Because of hardware and computational limitations, this mode is fit for repetition rates $\leq 500\,\mathrm{MHz}$.

To achieve fast *Femtosecond Covariance Spectroscopy*, we need to implement the generation of stochastic pulses on the dazzler device. There are two ways to do it.

The first approach is *deterministic*. It exploits the *streaming mode* of the device to mimic the generation of stochastic pulses used in SLM-based pulse shapers [14]. By randomizing the spectral amplitude of the acoustic wave, stochastic fluctuations can be added independently to the different spectral components of the optical pulse.
We refer to this approach as deterministic because the shaping reproduces a precise spectral profile in which stochastic fluctuations are introduced via software.

The second approach is fully *stochastic* and relies on the *continuous mode* operation of the dazzler. With this method, the electric signal produced by the RF generator is mixed with the white noise created by a waveform generator. The result is a fully stochastic signal that is subsequently converted in a noisy acoustic wave. Finally, acousto-optic interaction imprints the stochastic fluctuations on the diffracted optical pulse.

Design of the customized Dazzler

In collaboration with the R&D department of Fastlite, we designed a customized version of the dazzler that is compatible with the full stochastic approach previously described.
The design of the customized device is depicted in Figure 6.5. The system can operate both in *standard* mode or in *noisy* configuration, depending on the adopted wiring.
When the output of the RF generator is directly sent to the amplifier (red arrows), the system works as a standard dazzler[5]. If instead stochastic pulses are needed, the RF signal is sent to a mixer (blue arrows) where is combined with the white noise produced by a commercial waveform generator (LeCroy T3AFG120). The resulting pulse is a stochastic electric pulse that, after amplification, is finally converted into a stochastic acoustic wave that imprints stochastic fluctuations in optical pulses through the dazzler.

[5]Notably, it can be used both in *continuous* and *streaming* mode.

In Figure 6.6 we show the changes in the acoustic wave (green trace) when the RF signal is generated by the RF generator (Figure 6.6, a), by the noise source (Figure 6.6, b) or by the mixing of the two signals.
We notice that, when noise is added to the deterministic wave (c), the bandwidth of the acoustic pulse is increased. In particular, it goes from the 60-110 MHz range of the standard configuration to the 15-120 MHz range of the noisy one.

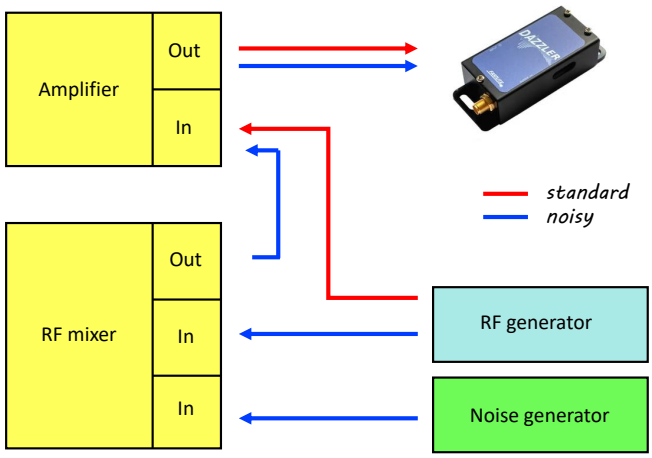

FIGURE 6.5: sketch of the customized dazzler. *Standard* configuration (red) is achieved by wiring directly the RF generator to the amplifier, that transmits the RF signal to the dazzler. In *noisy* configuration (blue), RF signal is mixed with the white noise produced by a waveform generator (LeCroy T3AFG120). The resulting signal is then amplified and sent to the dazzler. In this simple scheme filters are omitted.

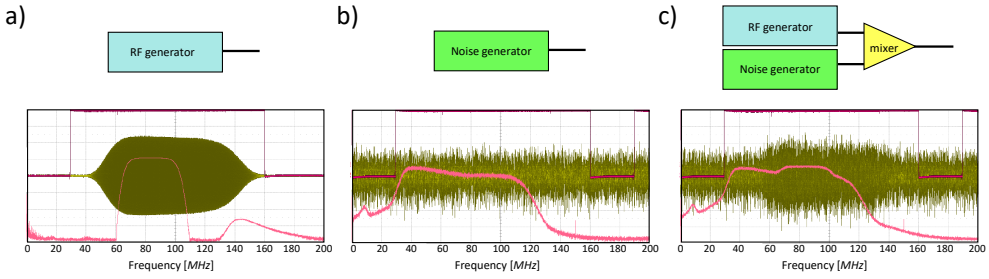

FIGURE 6.6: profile of the acoustic wave (green) with the relative bandwidth (pink) produced by the RF generator (a), the noisy generator (b) or by the mixing of the two signals (c).

6.3 Preliminary tests

In this section we present some preliminary measurements performed on the customized dazzler described in the previous Section. In particular, we test if the system is fit for static fast FCS experiments where stochastic fluctuations are present throughout the whole pulse spectrum (*full noise modulation*) or are limited to a selected spectral region (*partial noise modulation*). Finally, we test the system in dynamic measurements by adding a second pump pulse.
Besides the dynamic measurements, all the other tests are performed without a sample in order to study the features strictly connected to the stochastic light.

6.3.1 Full noise modulation

The first measurements that we present are static FCS experiments with *full noise modulation*, i.e. all the spectral components of the probe pulse are randomized. If the pulses are truly stochastic, we expect to measure a positive signal on the main diagonal and zero correlation elsewhere (see Chapter 5).
In Figure 6.7 we show a Pearson map obtained with the customized dazzler. We clearly notice that there are positive and negative fringes which run parallel to the main diagonal. By remarking that we expect zero correlation for full stochastic pulses, we conclude that the dazzler-based pulse shaper imprints multimode correlations on the probe spectrum and hence the resulting pulses aren't completely stochastic.

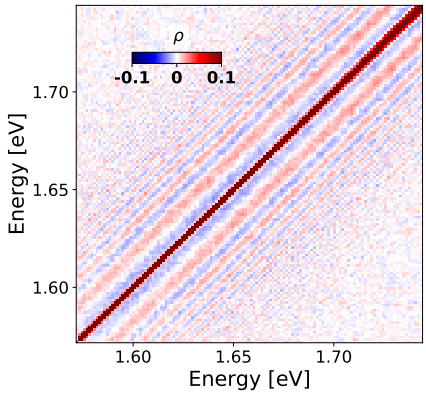

FIGURE 6.7: Pearson map obtained in the *full noise* configuration with the customized dazzler. Correlation fringes emerge parallel to the main diagonal.

Since the generation of full stochastic pulses is imperative for the succeeding of FCS, we investigate the origin of the correlation fringes. Specifically, we want to discriminate if the multimode correlations are linked to the acoustic wave itself or if they're intrinsic in the acousto-optic interaction.
Thus, we perform different measurements to test the dependence of the fringes from the power of the deterministic acoustic wave, from the amplitude of the fluctuations of the white noise and from the power of the optical pulse.

Acoustic power test

In Figure 6.8 we present the data obtained by varying the power of the acoustic wave produced by the RF generator. In details, Figure 6.8 (a) shows the changes in the spectrum of the shaped optical pulse when the power of the acoustic wave ($P_{acoustic}$) is varied. We

clearly see that the spectral amplitude decreases by reducing the power of the acoustic wave (see Appendix A, eq. 6.8).
Since the white-noise signal is kept constant, this results in an opposite trend for the level of noise in the pulse, that we quantify with the σ/μ ratio[6]. Indeed, by plotting the energy-integrated response, we see that a lower acoustic power determines a higher σ/μ ratio (see Figure 6.8, b).
In Figure 6.8 (c) we display the diagonal cuts[7] of the Pearons maps obtained with different $P_{acoustic}$ values.
We observe more pronounced correlation fringes when the value of the acoustic power is high. Reconnecting to Figure 6.8 (b), fringes are more visible when the level of noise (σ/μ) is low. In other words, the presence of stochastic fluctuations destroys multimode correlation.

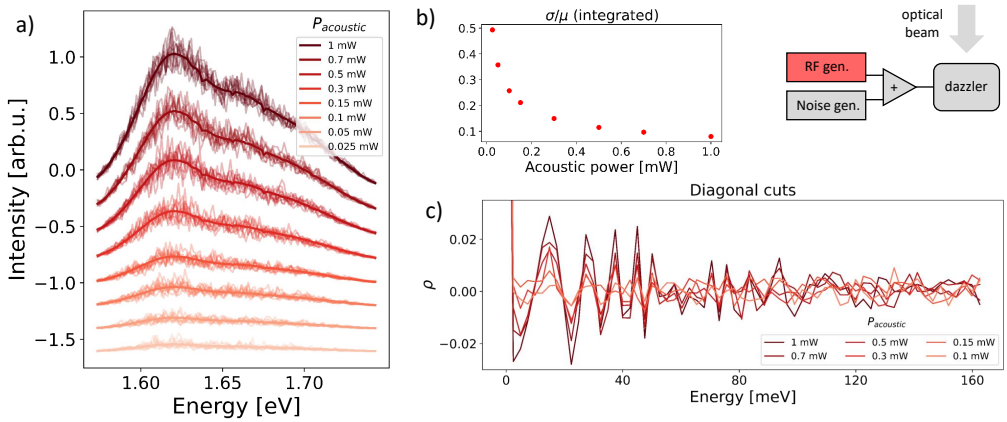

FIGURE 6.8: fringes dependence on the power of the acoustic wave ($P_{acoustic}$). In (a) and (b) we show the spectra and the level of noise (σ/μ) of the shaped optical pulses obtained with different values of $P_{acoustic}$. In (c) we display the dependence on $P_{acoustic}$ of the diagonal cuts of the Pearson maps.

White-noise test

In this paragraph, we present the measurements performed by changing the amplitude of the white-noise[8]. The results are displayed in Figure 6.9.
The spectral amplitude of the shaped pulses doesn't change by varying the amplitude of the white noise (Figure 6.9, a). Hence, the σ/μ ratio increases by increasing the noisy electric signal (Figure 6.9, b).
In Figure 6.9 (c) we display the diagonal cuts of the Pearson maps obtained with different amplitudes of the white-noise. Correlation fringes are more marked when the white-noise is low.
Notably, as in the case of the acoustic-power test (Figure 6.8), fringes are inversely proportional to the level of noise σ/μ.

[6] σ and μ stand for the frequency-integrated std. deviation and the value of the dataset, respectively.
[7] Diagonal cuts are performed perpendicularly to the main diagonal. Indeed, *x-axis* of 6.8 (c) is the distance in energy from the main diagonal.
[8] In details, we change the amplitude of the white noise by varying the *root mean square* value of the noisy electrical signal on the waveform generator. The *rms* value is expressed in *mV*.

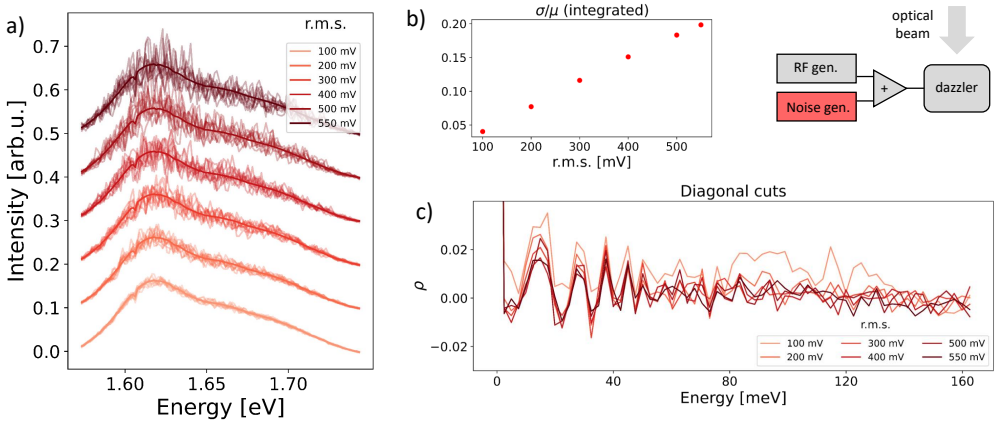

FIGURE 6.9: fringes dependence on the white-noise. We display the spectrum (a), the energy-integrated level of noise (b) and the diagonal cuts of the Pearson maps for different amplitudes of the white noise, expressed as the root-mean-square (r.m.s.) of the electric signal.

Optical power test

The last test that we perform consists in varying the power of the incoming optical pulse ($P_{optical}$). Results are shown in Figure 6.10.
In Figure 6.10 (a) we see that the amplitude of the shaped optical pulses depends on the incoming optical power. However, since no change in the generation of the acoustic wave is made, the level of noise σ/μ remains unaltered (Figure 6.10, b).
Analogously, also the diagonal cuts do not display significant changes with a variation of $P_{optical}$ (Figure 6.10, c).

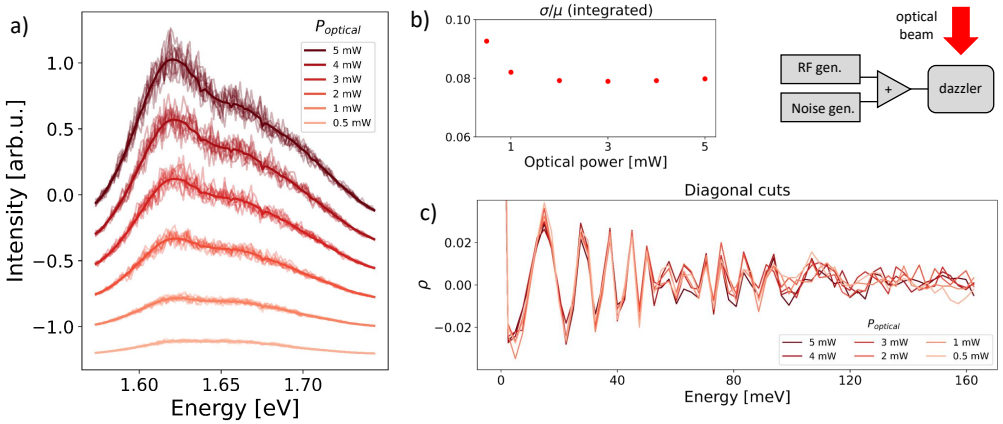

FIGURE 6.10: fringes dependence on the power of the incoming optical beam ($P_{optical}$. We show the spectra (a), the integrated σ/μ ratio (b) and the diagonal cuts of the Pearson maps (c) as a function of $P_{optical}$.

Summarizing, the three tests support a picture in which the correlation fringes are inversely proportional to the level of noise σ/μ of the stochastic pulses. Moreover, we exclude the scenario where multimode correlations are intrinsic in the acousto-optic interaction, since they do not depend on the power of the incoming optical beam (Figure 6.10).

6.3.2 Partial noise modulation

When we do static FCS experiments, there are two possible configurations available: one in which stochastic fluctuations are added to the whole spectrum and one where fluctuations are introduced just into a defined portion of the spectrum. We refer to the latter case as *partial noise modulation* (Figure 6.11).

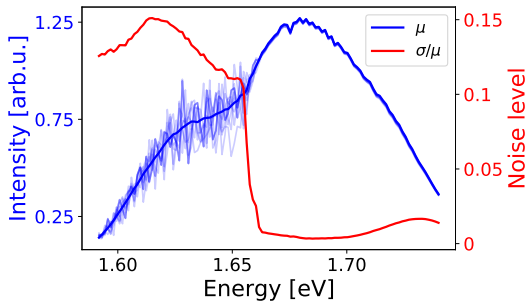

FIGURE 6.11: example of *partial noise modulation* performed with an SLM-based pulse shaper. In this case, stochastic fluctuations are added just in the low energy region of the spectrum.

To reproduce *partial noise modulation* in a dazzler-based pulse shaper, we have two alternatives:

- we can introduce low-pass/high-pass electronic filters in between the noise generator and the RF mixer to selectively add stochastic fluctuations to the low/high energy region of the spectrum.
- we can tune the noise bandwidth directly from the waveform generator.

The first approach is less versatile since we need a new filter with a different cutoff frequency whenever we want to change the range of the stochastic region.
Therefore, we start by investigating the second approach, where *partial noise modulation* is achieved by changing the bandwidth of the generated white noise.

In Figure 6.12 we plot the pulse spectrum and the correspondent Pearson map obtained by reducing the cutoff frequency of the noise generator to $100\,\mathrm{MHz}$[9]. We notice that the noise level σ/μ is higher in the low energy region of the spectrum, as we expect. However, we detect no sharp transition from the noisy region of the spectrum to the coherent one, as we did in FCS experiments with the SLM-based pulse shaper (see Figure 6.11) . Importantly, we never measure a zero-noise region (see Appendix B).
This evidence reflects on the Pearson map (Figure 6.12, right), where we do not see the typical division in quadrants of *partial noise modulation* maps.
We address this behavior to the non-sharp edge of the white noise bandwidth.

Indeed, by measuring directly the noisy electric signal produced by the waveform generator, we see that the bandwidth is not a step-like function, but instead decreases smoothly above the cutoff frequency (Figure 6.13, blue).
Therefore, the approach that accounts on the tuning of the noise bandwidth directly from the generator isn't fit for *partial noise modulation*, since we can't generate well separated

[9]Which corresponds to $\sim 1.617\,\mathrm{eV}$ (see eq. 6.3), that lies almost in the middle of the optical pulse bandwidth.

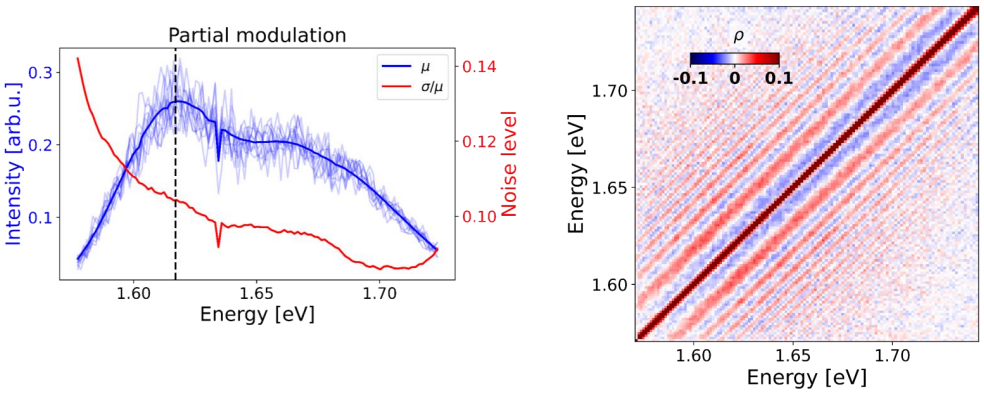

FIGURE 6.12: *partial noise modulation* with dazzler. Both the pulse spectrum and the noise level (left) present no sharp change in correspondence of the cutoff frequency of the noise generator (black dashed line). As a consequence, the Pearson map (right) doesn't show the characteristic division in quadrants typical of *partial noise modulation* measurements.

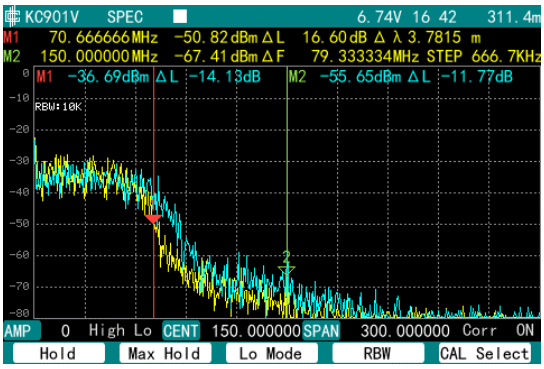

FIGURE 6.13: We show the bandwidth of the white noise with a cutoff frequency, set on the waveform generator, of 70 MHz (red vertical line). Yellow and blue traces represent the noisy signal bandwidth in the presence (yellow) or in the absence (blue) of an additional low-pass filter (70 MHz) inserted in between the waveform generator and the RF mixer.

coherent and noisy regions in the pulse spectrum.

We can still try to accomplish *partial modulation* by using the static filter approach, in which low-pass/high-pass filters are added in between the waveform generator and the RF mixer. Indeed, Figure 6.13 shows that adding a static filter heavily improves the sharpness of the bandwidth edge (yellow trace).
Further studies using static filters with proper cutoff frequencies are required to finally establish if dazzler-based pulse shaper is suited for *partial noise configuration* or not.

6.3.3 Dynamic measurements

Finally, we test the dazzler-based pulse shaper in a pump-probe FCS experiment. In particular, we're interested in understanding if the correlation fringes that dominate the static response (Figure 6.7) are present also in the dynamic maps or if they're washed out in the differential signal.
Notably, since we can't accomplish *partial noise modulation*, we perform the dynamic measurements with *full noise modulation*.

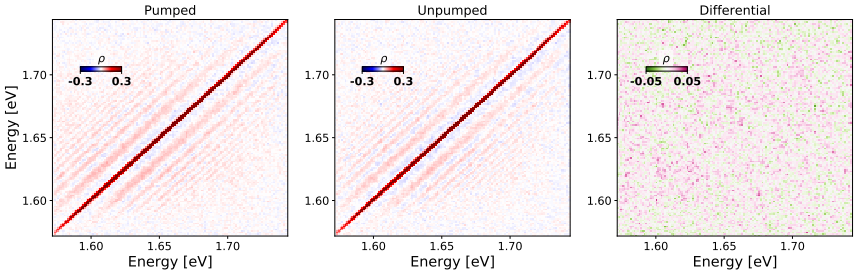

FIGURE 6.14: Pearson maps obtained in the presence (left), absence (center) of the pump pulse ($\Delta t = 0$) and by subtracting the two maps (right). Notably, correlation fringes disappear in the differential map.

We perform the dynamic measurement on the same BSCCO sample studied in Chapter 5 (OP, $T_c = 90\,\mathrm{K}$) . In particular, we try to reproduce the superconducting signal observed in Section 5.4. In Figure 6.14 we show the pumped/unpumped/differential Pearson maps. Remarkably, the differential Pearson maps (Figure 6.15, right) show no trace of the correlation fringes present in both the pumped and unpumped maps (Figure 6.15, left and center). In other words, the spurious multimode correlation linked to the generation of the acoustic wave is washed out by the subtraction of the two maps.
This evidence opens the possibility of employing the dazzler-based pulse shaper to perform fast FCS dynamic experiments.

Figure 6.15 displays the dynamic map that groups all the integrated differential Pearson maps at different pump-probe delays (see Section 5.4)[10]. The dynamic map shows a transient signal in correspondence of the temporal overlap between the two pulses that

[10]We point out that we don't expect to resolve the full ultrafast dynamics of the superconducting signal studied in Section 5.4. Indeed, we are performing a FCS measurement with *full noise* modulation, that is less sensitive than *partial noise* configuration to weak signals [15].

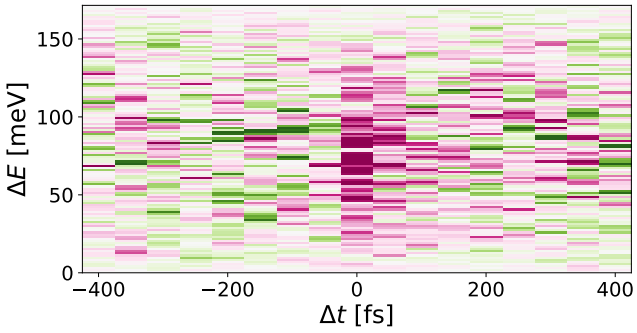

FIGURE 6.15: FCS dynamic map obtained by combining all the integrated differential Pearson maps at different time delays. We detect a signal at the overlap.

isn't affected by the presence of the fringes. Importantly, the dynamic map of Figure 6.15 is obtained in $\sim$ 10 minutes, while dynamic maps obtained with the SLM-based pulse shaper (see Section 5.4) require more than 6 hours of measurement.

6.4 Conclusions and Perspectives

In this Chapter, we presented a novel design of a pulse shaper based on an acousto-optic programmable dispersive filter (dazzler) that potentially opens the path for fast FCS experiments. Indeed, by combining a pulsed electric signal with the white noise produced by a waveform generator, it is ideally possible to generate stochastic optical pulses with repetition rates $\leq 30\,\mathrm{kHz}$.

We tested the device for the generation of fully and partially modulated stochastic pulses.
Our preliminary measurements showed that the shaped optical pulses aren't completely uncorrelated, but instead present multimode correlation fringes. There are indications that link the correlation fringes to the acoustic wave itself more than to the acousto-optic interaction. In this perspective, further investigations are needed to discriminate if fringes originate in the white-noise signal or in other processes (e.g. saturation of the RF signal).

Secondly, we tested the system for the generation of stochastic fluctuations into a limited portion of the optical spectrum. The test provided a negative outcome, since we couldn't generate two distinct regions characterized by coherent and stochastic fluctuations.
However, a possible solution could by provided by the insertion of static filters directly on the output of the waveform generator, in order to transform the smoothed white-noise bandwidth into a step-like function.

We underline that both the presence of correlation fringes and the impossibility in generating partially stochastic pulses may be solved by adopting a *deterministic* approach where the stochastic acoustic wave is already produced by the RF generator.
Indeed, by mimicking the generation process adopted with the SLM-based pulse shaper, we would be able to selectively randomize different spectral regions of the stochastic pulses with a sharp transition to the coherent ones.
Moreover, if correlation fringes are really linked to the white-noise electric signal, they should disappear by eliminating that component from the acoustic wave.
Notably, this solution would determine a lower operational repetition rate ($\leq 500\,\mathrm{Hz}$), that would still be a significant improvement with respect to the current SLM-based technology (max rep.rate $< 100\,\mathrm{Hz}$).

Finally, we performed a preliminary dynamic measurement on BSCCO, to test the capabilities of the dazzler-based pulse shaper for pump-probe FCS experiments.
Remarkably, we discovered that correlation fringes are washed away in the differential signal and hence that it is possible to detect the dynamic response without spurious effects. Moreover, the acquisition times are drastically reduced (6 hours (SLM) vs 10 minutes (dazzler)), proposing the dazzler as the ideal tool to perform fast dynamic FCS experiments.

Appendices

A Time-convolution description of Acousto-Optic Pulse Shaping

In the following, we describe with a rigorous approach the three-wave mixing process at the basis of acousto-optic pulse shaping.

For low diffraction efficiencies ($\ll 100\%$), the outcoming complex electric field $E_{diff}(t)$ is proportional to the convolution of the optical input field $E_{in}(t)$ with the electric signal $S(t/\alpha)$, where α is the almost frequency-independent ratio between the acoustic and the optical frequencies (see equation 6.3):

$$E_{diff}(t) = E_{in}(t) \otimes S(t/\alpha) \tag{6.5}$$

We can rewrite equation 6.5 in the frequency domain as

$$E_{diff}(\omega) = E_{in}(\omega) \cdot S(\alpha\omega) = E_{in}(\omega) \cdot S(\omega_{ac})$$

Notably, the phase of the diffracted beam is:

$$\psi_{diff} = \psi_{in} + \psi_{ac}$$

and hence, the total control of the spectral phase of the diffracted beam is performed via a phase transfer from the acoustic wave to the optical input one.
We model the action of the AOPDF with a transfer function $H(\omega)$ defined by

$$E_{diff}(\omega) = H(\omega) \cdot E_{in}(\omega) \tag{6.6}$$

and

$$H(\omega) = \sqrt{\eta(\omega)}\, e^{i\phi(\omega)} \tag{6.7}$$

where $\eta(\omega)$ represents the frequency-dependent diffraction efficiency and $\phi(\omega)$ is the spectral phase programmed in the AOPDF and applied to the input optical pulse.
From eq. 6.6 and 6.7, we can write ψ_{diff} as:

$$\psi_{diff} = \psi_{in} + \phi(\omega)$$

Therefore, by changing $\phi(\omega)$, we can directly modify the spectral phase of the diffracted beam.

The spectral intensity of the diffracted beam is, in the plane wave and monochromatic approximation [9]:

$$I_{diff}(\omega) = \eta(\omega) I_{in}(\omega)$$

with

$$\eta(\omega) = \frac{\pi^2}{4}\frac{P}{P_0} sinc^2\left[\sqrt{\frac{\pi^2}{4}\frac{P}{P_0} + \left(\frac{\Delta k\, L}{2}\right)^2}\right] \tag{6.8}$$

where:

- $I_{in}(\omega)$ is the input optical intensity
- $\Delta k = (\vec{k}_{diff,e} - \vec{k}_{in,o} - \vec{k}_{ac}) \cdot \hat{e}_{ac}$ is the phase-matching mismatch along the acoustic propagation direction

- P is the actual acoustical power density
- P_0 is a characteristic acoustic power that depends on the specific AOPDF[11]
- L is the crystal length

Notably, the full control on the spectral intensity of the diffracted beam $I_{diff}(\omega)$ is related to the phase-matching conditions and to the acoustic power P.

[11] In particular, when $P = P_0$ and phase-matching conditions are fulfilled ($\Delta k = 0$), the transfer coefficient to the diffracted wave is 100% ($I_{diff}(\omega) = I_{in}(\omega)$).

B Variable cutoff frequency test

In Chapter 6 we couldn't achieve a zero-noise configuration with *partial noise modulation* by using the dazzler. We explained this result with the smooth shape of the bandwidth of the white-noise.
In this Appendix we further investigate the *partial noise* configuration by changing the cutoff frequency of the noise bandwidth and by moving it out of the pulse energy range. In this way, we move across the smoothed edge of the white-noise bandwidth and we expect to reach a zero-noise region where coherent fluctuations are dominant.

In Figure B.1 we show the Pearson maps obtained for different cutoff frequencies of the white-noise generator. We see that coherent fluctuations appear just at low cutoff frequencies ($\leq 60\,\mathrm{MHz}$).
This result is consistent with the level of noise graph (Figure B.2), where zero-noise region is accessed just at small values of the cutoff frequency.

Interestingly, we notice that before the coherent fluctuations become dominant, correlation fringes become more intense (Figure B.1). This evidence suggests that the residual noise present above the cutoff frequency (see Figure 6.13) may be directly involved in the generation of the spurious multimode correlation fringes.

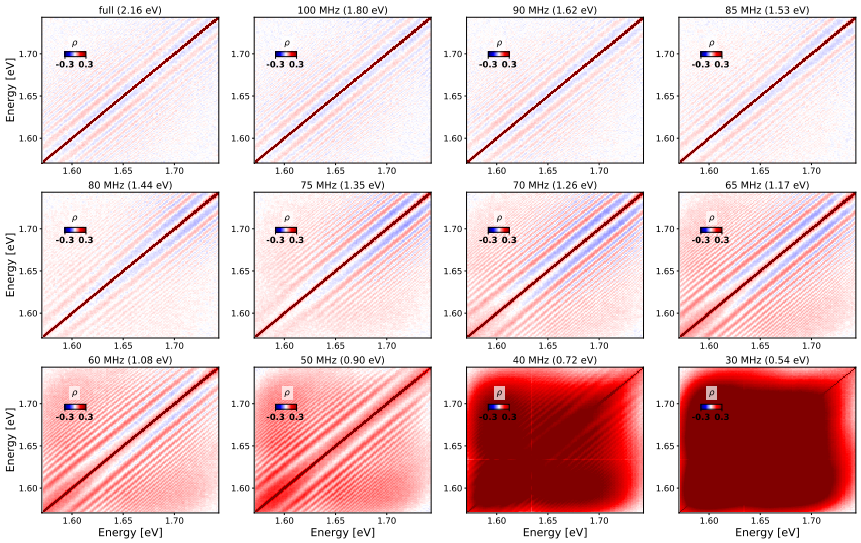

FIGURE B.1: Pearson maps obtained for different cutoff frequencies of the noise generator. In the parenthesis, we specify the correspondent optical frequency.

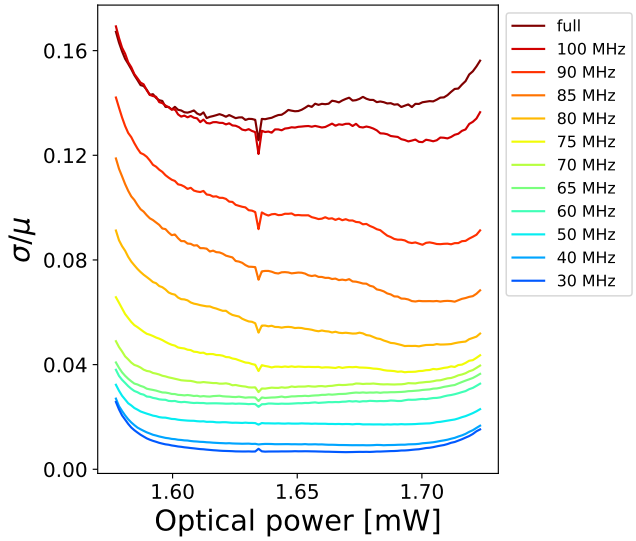

FIGURE B.2: noise level spectra acquired at different cutoff frequencies of the white-noise bandwidth.

References

[1] IC Chang. "Noncollinear acousto-optic filter with large angular aperture". In: *Applied Physics Letters* 25.7 (1974), pp. 370–372.

[2] Jieping Xu and Robert Stroud. *Acousto-optic devices: principles, design, and applications*. Wiley, 1992.

[3] Zhiping He et al. "Spectrometers based on acousto-optic tunable filters for in-situ lunar surface measurement". In: *Journal of Applied Remote Sensing* 13.2 (2019), pp. 027502–027502.

[4] Youngwook Seo et al. "Morphological image analysis for foodborne bacteria classification". In: *Transactions of the ASABE* 61.1 (2018), pp. 5–13.

[5] Liqun Chen et al. "Hyperspectral imaging system based on fiber endoscope". In: *Twelfth International Conference on Information Optics and Photonics*. Vol. 12057. SPIE. 2021, pp. 1078–1083.

[6] Andrew M Weiner. "Femtosecond pulse shaping using spatial light modulators". In: *Review of scientific instruments* 71.5 (2000), pp. 1929–1960.

[7] Pierre Tournois. "Acousto-optic programmable dispersive filter for adaptive compensation of group delay time dispersion in laser systems". In: *Optics communications* 140.4-6 (1997), pp. 245–249.

[8] Frederic Verluise et al. "Amplitude and phase control of ultrashort pulses by use of an acousto-optic programmable dispersive filter: pulse compression and shaping". In: *Optics letters* 25.8 (2000), pp. 575–577.

[9] D Kaplan and P Tournois. "Theory and performance of the acousto optic programmable dispersive filter used for femtosecond laser pulse shaping". In: *Journal de Physique IV (Proceedings)*. Vol. 12. 5. EDP sciences. 2002, pp. 69–75.

[10] Antoine Monmayrant et al. "AOPDF-shaped optical parametric amplifier output in the visible". In: *Applied Physics B* 81 (2005), pp. 177–180.

[11] Sebastien Coudreau, Daniel Kaplan, and Pierre Tournois. "Ultraviolet acousto-optic programmable dispersive filter laser pulse shaping in KDP". In: *Optics letters* 31.12 (2006), pp. 1899–1901.

[12] Raman Maksimenka et al. "Direct mid-infrared femtosecond pulse shaping with a calomel acousto-optic programmable dispersive filter". In: *Optics letters* 35.21 (2010), pp. 3565–3567.

[13] Stéphanie Grabielle. "Manipulation et caractérisation du champ électrique optique: applications aux impulsions femtosecondes". PhD thesis. Ecole Polytechnique X, 2011.

[14] Giorgia Sparapassi. "Femtosecond Covariance Spectroscopy". PhD thesis. University of Trieste, 2019.

[15] Jonathan Owen Tollerud et al. "Femtosecond covariance spectroscopy". In: *Proceedings of the National Academy of Sciences* 116.12 (2019), pp. 5383–5386.

Chapter 7
Conclusions

The physics of complex materials is characterized by the intricate interplay between magnetic, vibrational and electronic degrees of freedom. The understanding of the microscopic mechanisms which rule the physical properties of these systems requires studies that go beyond the linear response. In this framework, non-linear spectroscopy, and in particular pump-probe spectroscopy, established as a unique tool to disentangle competing interactions and to control transient states of matter.

During my PhD, I approached the problem of non-equilibrium physics in complex systems from two different perspectives. Part of my activities was dedicated to 'conventional' pump-probe spectroscopy and to its application to the study of complex materials. On the other hand, I followed the direction of my group that aims at developing new techniques that go beyond standard intensity measurements and focus on different optical observables, like the quantum state of light or the multimode covariance. In this work, I presented both of these aspects, dividing the manuscript in two parts.
The first part of the thesis was dedicated to pump-probe experiments on two different materials: $RbNiF_3$, a magnetic compound characterized by low-temperature ferrimagnetic ordering, and $Bi_2Sr_2CaCu_2O_{8+\delta}$, a high temperature superconductor which belongs to the family of Cuprates. Then, the second part of the thesis focused on the development and commissioning of a novel spectroscopic technique, i.e. Femtosecond Covariance Spectroscopy, and on its application to the study of complex materials.

Firstly, we presented the dynamic study of the ferrimagnetic compound $RbNiF_3$. By performing a non-equilibrium investigation of the material, we revealed novel information hidden to the static response. In details:

- we reported the presence of a long-living dynamic signal ($100\,\mu s < \tau < 20\,ms$) that we associated to a transient magneto-optical Faraday effect. Moreover, the resonant nature of the signal led to a picture in which the relaxation of *dd* excited states induces a metastable phase of the material with a modification of the lattice/magnetic environment.

- in the aforementioned long-living signal, we found signatures of an extra sideband of the $^3A_2 \rightarrow {}^1E^a$ transition, hidden in the static response. By following the evolution of this new feature across the sample phase-transition, we linked it to the ferrimagnetic ordering and in particular to an *exciton-phonon-2magnon* transition.

- we identified different coherent modes that we associated to phonons with different symmetries. Interestingly, we unveiled an unconventional spectral dependence of

the modes that we addressed to different dd-phonon coupling mechanisms. Supported by DFT calculations, we linked the specific couplings to the different atomic displacements of the coherent excitations.

The second non-equilibrium experiment presented in the thesis was dedicated to the high temperature superconductor $Bi_2Sr_2CaCu_2O_{8+\delta}$. Our study aimed at characterizing electronic Raman scattering from Cooper pairs and at testing the selection rules of the B_{1g}/B_{2g} electronic excitations.
The polarimetry measurements that we performed depicted very different scenarios for the two modes. Indeed, we discovered that nodal excitations (B_{2g}) obey to an equilibrium model where the action of the pump is neglected. Oppositely, the selection rules of the B_{1g} mode can't be reproduced in any way by models based on the Cuprates symmetry group D_{4h}.
Interestingly, we noted that a model which includes asymmetric terms in the Raman tensor (and hence predicts time-reversal symmetry breaking) may explain our observations. If validated by forthcoming measurements on samples with different levels of doping, these results would open new perspectives on the transient states achievable via resonant pumping on unconventional superconductors.

The second part of the manuscript was devoted to Femtosecond Covariance Spectroscopy (FCS), a novel spectroscopic technique which relies on multimode photonic correlations to unveil the non-linear response of materials. We introduced the basic principles of the technique and we presented a characterization of the Raman spectrum of α-quartz performed with FCS.
Secondly, we applied FCS to the study of complex materials. With static FCS, we investigated the non-linear response of $RbNiF_3$ in the different phases of the sample, in order to understand whether or not the technique is sensitive to magnetic excitations. Although the results are not conclusive, we found signatures of the 2-magnon excitation in the correlation maps, indicating that FCS can possibly be applied also to the study of magnons.
Finally, we combined FCS with a pump-probe scheme to perform a dynamic study of the electronic excitations in $Bi_2Sr_2CaCu_2O_{8+\delta}$. We isolated a superconducting correlation signal in correspondence of the B_{1g}/B_{2g} excitations, performing a time-resolved Raman-like measurement of the modes with sub-ps temporal resolution. Nonetheless, the main result of our investigation was the discovery of a correlation signal qualitatively similar to the SC one also in the pseudogap phase. Our interpretation of these preliminary results addressed the correlation signal to the scattering of the superconducting gap and its observation in the PG phase to the presence of local pairing above T_c.

Notably, FCS experiments on $RbNiF_3$ and $Bi_2Sr_2CaCu_2O_{8+\delta}$ highlighted an important issue of the technique, which is the speed limitation of the measurements. Indeed, for both systems we couldn't perform a proper temperature study of the correlation signals across the phase transitions because of the long acquisition times ($\sim 60\,\mathrm{Hz}$).
To overcome this limitation, we presented an alternative arrangement for FCS which could potentially work 500 times faster than the standard technique. By employing an acousto-optic crystal (*dazzler*) in combination with a source of white noise, we developed a pulse shaper which can generate stochastic pulses with repetition rates $\leq 30\,\mathrm{kHz}$.
The first tests that we performed on the dazzler-based pulse shaper unveiled two important issues: the presence of multimode correlations and the impossibility of localizing stochastic fluctuations into limited regions of the spectrum. However, there are possible solutions, like the employment of a different white noise source or the use of static filters, that will be explored in the future to understand the feasibility of fast FCS experiments.

List of Publications

- **Rigoni E.M.**, Montanaro A., Enderlein N., ... & Fausti D., Ultrafast signatures of resonant transient Faraday effect and dd-phonon coupling in the ferrimagnetic compound $RbNiF_3$. *To be submitted*

- Montanaro A.*, **Rigoni E.M.***, . . . & Fausti D. Ultrafast measurement of superconducting fluctuations in the Pseudogap phase of optimally-doped $Bi_2Sr_2CaCu_2O_{8+\delta}$ with covariance-based stochastic spectroscopy. *In preparation*

- Montanaro A., **Rigoni E.M.**, Giusti F., Barba L., Chita G., Glerean F., ... & Fausti D. (2023). Dynamics of non-thermal states in optimally-doped $Bi_2Sr_2Ca_{0.92}Y_{0.08}Cu_2O_{8+\delta}$ revealed by mid-infrared three-pulse spectroscopy. arXiv preprint arXiv:2310.10279, *Accepted by Phys.Rev B*.

- Glerean F., **Rigoni E.M.**, Jarc G., Mathengattil S.Y., ... & Fausti D. Ultrafast pump-probe phase-randomized tomography. *To be submitted*

- Jarc G., Mathengattil S. Y., Montanaro A., Giusti F., **Rigoni E. M.**, Sergo R., ... & Fausti D. (2023). Cavity-mediated thermal control of metal-to-insulator transition in $1T - TaS_2$. *Nature*, 622(7983), 487-492.

- Glerean F., Jarc G., Marciniak A., Giusti F., Sparapassi G., Montanaro A., **Rigoni E.M.**, ... & Fausti D. (2020). Time-resolved multimode heterodyne detection for dissecting coherent states of matter. *Optics Letters*, 45(13), 3498-3501.

- Montanaro A., Giusti F., Zanfrognini M., Di Pietro P., Glerean F., Jarc G., **Rigoni E.M.**,... & Fausti, D. (2022). Anomalous non-equilibrium response in black phosphorus to sub-gap mid-infrared excitation. *Nature Communications*, 13(1), 2667.

- Jarc G., Mathengattil S. Y., Giusti F., Barnaba M., Singh A., Montanaro A., **Rigoni E.M.**, ... & Fausti D. (2022). Tunable cryogenic terahertz cavity for strong light–matter coupling in complex materials. *Review of Scientific Instruments*, 93(3).

Ringraziamenti

Dopo aver (finalmente!) finito di scrivere questa tesi, mi trovo ad affrontare la pagina più bella, quella dei ringraziamenti, ed inevitabilmente a fare un bilancio degli ultimi quattro anni.
Che il dottorato non sarebbe stato una passeggiata si era capito dal prinicpio, ovvero da quel lontano Novembre 2020 passato non in ufficio/laboratorio, ma rinchiuso in camera col Covid a consumare i martelletti del fidato Yamaha. Eppure, poco più di un mese dopo, non riuscivo a smettere di ridere euforico mentre lasciavo Cesena con mio papà, un diploma e la voglia di cominciare la nuova vita da dottorando.
Forse, le montagne russe di quei primi mesi rappresentano bene ciò che è stato il mio dottorato: un'alternanza di momenti difficili e soddisfazioni che mi hanno formato a livello scientifico, ma soprattutto sul piano umano.

Il primo Grazie è quindi per Daniele, che da supervisor mi ha sempre dato fiducia e massima libertà di movimento, perché "alla fine in laboratorio ci siete voi". Grazie però soprattutto per tutto ciò che va aldilà della fisica, per l'inesauribile positività e per avermi insegnato a lavare sempre la macchina prima di un matrimonio.
Il secondo Grazie è obbligatoriamente per tutti i fantastici compagni del gruppo *Q4Q*. Ad Angela, per aver condiviso le più esasperanti esperienze in laboratorio (noise correlation?) e per l'infinita disponibilità a dare una mano, quale che sia il problema. A Giacomo, per essere stato compagno di esperienze surreali (Metro parigina, Hotel International, ...) e per aver accresciuto la mia cultura con la barzelletta del "tubicino blu" o del "panino alla mortadella". Grazie ad entrambi per avermi reso la Germania un paese ospitale, per gli aggiornamenti quotidiani sulla discografia del maestro e per l'esperienze in stile concerto Biei Watch + carroattrezzi.
Grazie a Shahla, per essere stata la compagna di banco di questo dottorato: aver vissuto assieme gioie e dolori ha reso il percorso meno impervio. Grazie anche per aver condiviso un po' di India in forma di racconti, cene o *banana chips*. Grazie a Francesca e Filippo, per rispondere ancora presenti alle reunion, treni e aerei permettendo.
Un Grazie particolare anche agli studenti con cui ho avuto il piacere (spero ricambiato) di lavorare. In particolare, un Grazie a Costanza e Giovanni, che con il loro modo di essere hanno reso speciali i mesi passati assieme a raccogliere dati. Grazie anche per la delicata introduzione all'arrampicata (Costanza) e per l'indimenticabile massima sui magnoni (Giovanni).
Devo quindi assolutamente ringraziare i nostri cugini di *T-Rex* Manuel, Denny, Wibke e Federico per la disponibilità e la fratellanza, come il gruppo degli elettronici con Gabriele, Matija, Rudi, Marco e Bepo per l'inesauribile pazienza. Infine, un sentito grazie al prof. Parmigiani per avermi regalato ormai 7 anni fa un libro che è stato assieme iniezione di fiducia e piccola spinta.

Seguono quindi i Grazie per tutti coloro che non hanno direttamente a che fare con la spettroscopia pump-probe, ma la cui presenza è stata per me fondamentale. Grazie

ai compagni "perfettamente normali" sparpagliati in giro per l'Europa, che è così bello ritrovare nonostante le grandi distanze (vero Willy?). Soprattutto Grazie a Seba e Virtus, per tutto ciò che non so esprimere ma che possiamo trovare davanti a tre tagli da Scussa. Grazie poi agli amici di sempre e a quelli che ho avuto la fortuna di conoscere durante questi quattro anni, per tutti i momenti di spensieratezza, gioia e affetto che mi regalate. Un Grazie a parte per Federico e Jacopo, la cui presenza nei momenti belli e in quelli di mare in tempesta è insostituibile.

Grazie infine alla mamma, al papà, alla nonna e ai miei guardiani silenziosi. L'amore che mi date ogni giorno è assieme la benzina per i miei sforzi e il dono più grande che potessi chiedere.
L'ultimo Grazie è per Bianca. Gli Afterhours, in una canzone che sembra scritta apposta, cantavano: "Sei il colore che non ho". Grazie per avermelo portato.